FLIGHT CONTROL AND HARDWARE DESIGN OF MULTI-ROTOR SYSTEMS

by

Nathan M. Zimmerman, B.S.

A Thesis Submitted to the Faculty of the Graduate School
Marquette University,
in Partial Fulfillment of the Requirements for
the Degree of Master of Science

Milwaukee, Wisconsin

June 2016

ABSTRACT

FLIGHT CONTROL AND HARDWARE DESIGN OF
MULTI-ROTOR SYSTEMS

Nathan M. Zimmerman, B.S.
Marquette University

This thesis overviews crucial concepts involved in achieving quadcopter flight such as orientation estimation and control system implementation. This thesis also presents researchers with comprehensive hardware and software specifications for a quadcopter system. The primary application for this system would be for research with regards to the implementation of advance control techniques as well as data acquisition. Key constructs of this system include hardware software specifications for a flight controller, the radio system, and the sensorless brushless motor controllers.

Firstly, the thesis starts by developing a reference frame and a mathematical model for the quadcotper system. Next, flight orientation estimation is determined through an assortment of MEMS sensors such as an accelerometer, gyroscope, and magnetometer. Each sensor will be individually addressed as to its strengths and weaknesses with regards to orientation estimation. An algorithm will then be proposed for the combination of these various sensors. Finally, an algorithm will be purposed for translating the orientation feedback into a control system that will efficiently stabilize the quadcopter.

Finally, this thesis will overview methods of integrating lidar data directly into the quadcopter's control system. Real-world lidar data is used and a computational geometry algorithm, ICL, is employed to translate the point cloud data into relevant control parameters.

ACKNOWLEDGEMENTS

Firstly, I would like to thank my parents who cultivated my passion for engineering and provided endless encouragement. Secondly, I would like to thank my advisor, Dr. Cris Ababei, who provided a TA-scholarship and academic support which made this thesis possible. I also would like to thank my other committee members, Dr. Susan Schneider and Dr. Ronald Brown, for taking the time to review this thesis and provide feedback.

I would also like to thank all of the engineers who significantly invested in me during my development as an engineer. Specifically, I would like to thank Brian Booth from John Deere who invested in teaching me fundamentals of hardware engineering. Likewise, I would like to thank Bradly Schleusner and Nicholas Butts from Appareo Systems who taught me vital fundamentals of writing embedded software. In addition, I would like to thank Dr. James Richie for an incredibly useful antenna theory class which made the RF portions of this thesis possible. I would also like to thank Kellen Carrey for his feedback as well as assistance in developing the RF controller. Finally, I would like to thank my fellow lab mates, Milad Ghorbani and Wenkai Guan, who managed to put up with the noise this thesis generated as well provide useful feedback and support.

TABLE OF CONTENTS

TABLE OF CONTENTS — *Continued*

TABLE OF CONTENTS — *Continued*

TABLE OF CONTENTS — *Continued*

LIST OF TABLES

LIST OF FIGURES

LIST OF FIGURES — *Continued*

LIST OF NOMENCLATURE AND ACRONYMS

IMU: Inertial Measurement Unit.

ESC: Electronic Speed Controller.

PPM: Pulse Position Modulation.

EMF: Electro-motive Force.

BEMF: Back Electro-motive Force.

MCU: Micro-Controller Unit.

FSK: Frequency Shift Keying.

USB: Universal Serial Bus.

UART: Universal Asynchronous Receive Transmit.

MEMS: MicroElectroMechanical System.

PID: Proportional Integral Derivative.

SPI: Serial Peripheral Interface.

LiDAR: Light Detection And Range.

RF: Radio Frequency.

UHF: Ultra High Frequency.

ISM: Industrial Scientific Medical

CPWG: CoPlanar WaveGuide.

FPU: Floating Point Unit.

LiPo: Lithium-ion Polymer.

FET: Field Effect Transistor

QFN: Quad Flat No-leads

ICP: Iterative Closest Point

ICL: Iterative Closest Line

Table 0.1: Key Nomenclature

math/symbol	definition
θ	Pitch
ϕ	Roll
ψ	Yaw
$\hat{x}$	Estimate of x
$\bar{x}$	Unit vector of x direction
$\cdot$	Scalar product
$\times$	Cross product
$UPPERCASE$	Matrix
A^{-1}	Inverse of matrix A
$\|x\|$	Absolute value of x
$atan2()$	Four quadrant arc tangent function
$atan()$	Traditional two quadrant arc tangent function

CHAPTER 1

Problem Statement, Objective and Contributions

1.1 Problem statement

This thesis focuses on developing multi-rotor control theory, inertial measurement orientation fusion, and finally a comprehensive software/hardware platform specification for multi-rotor research. To establish a reference frame, this thesis will specify a mathematical coordinate system and then use this system to construct control goals. The following sections will then focus on how to meet the purposed control goals. An overview of existing IMU sensors will be presented as well as their trade offs with respect to aerial vehicle flight. An algorithm will then be purposed on how to fuse this data to overcome the existing sensor limitations and weaknesses. Once known orientation has been establish, this thesis will then focus on specifying multi-rotor kinematics, software and hardware involved in control. Finally, this thesis will explore means of autonomous control with lidar and sonar sensors.

The primary problem this thesis attempts to solve is in reducing barriers to entry for advance control techniques. When building a multi-rotor vehicle(drone), designers are faced with the choice of paying for a custom designed aerial vehicle, building their own vehicle from scratch, or sacrificing controllability for a cheap off-the-shelf system. While numerous cheap off-the-shelf multi-rotor platforms are available, they often consist of proprietary modules even when advertised as open-source. Common examples of these

black-box modules are sensor-less brushless motor controllers, flight controllers, and radios. These modules are often proprietary and have limited **hardware** specifications [3],[4]. Consequently for a researcher, the control and the modifiability of these modules is limited.

1.2 Objectives

A main objective of this work is provide researchers with a functional, fully specified, and stabilized quadcopter. This system will be specified from scratch hardware and software with the intent of eliminating as many black boxes components as possible. In addiction, this flight system will have an emphasis on theoretical control as well as data collection making it a prime candidate for research and reference.

1.3 Previous Work

Admittedly, much work has been done in the area of advance control of multirotor systems and these works are too numerous for a comprehensive listing. Consequently, key examples will be provided that were used as a reference for the development of this thesis. For example, Robert Mahony presents a comprehensive method for modeling, orientation, and control of a quadcopter with state space methods [5]. Another example of advance control is where researchers at University of Zurich implemented a quadcopter with a model predictive control were able to perform extreme acrobatic maneuvers [6],[7]. Numerous other control techniques have been applied to quadcopters as well such as PID, LQR, LQR-PID, and H_∞ [8], [9].

With regards to open source multi-rotor systems, Open Pilot and Clean Flight are perhaps two of the most popular open software flight controller systems. These systems support a

broad range of multi rotor vehicles from tri-copters to octo-copters [3],[4]. With regards to open source software and hardware systems, the Pixhawk and Sparky systems feature an open source flight controllers [10],[11]. While these systems feature some open hardware and software, they integrate with systems that are proprietary.

In regards to indoor autonomous control, this is an active area of research for all types of remote vehicles. Mapping of unknown environments has been conducted with mutli-rotor vehicles utilizing lidar and employing the iterative closest point (ICP) algorithm[12],[2],[13]. However, in these cases the multi-rotor vehicle was operated by a human. A team at MIT achieved autonomous indoor control of an aerial vehicle by combining lidar data and IMU data with an extended Kalman filter as well as a Gaussian particle filter [14]. However, in this case the environment had been pre-mapped and pre-determined trajectories were used. Comprehensive simultaneous mapping and control complex and still an ongoing area of research.

1.4 Contributions

This thesis develops a functional multi-rotor flight system with a higher level of integration than most other open source options. In addition, this thesis develops a computationally efficient lidar parsing algorithm. The key contributions of this flight system are as follows:

- Provides open source software / hardware files for a functional stabilized auto-leveling flight controller
- Provides open source software / hardware files for a remote remote control system

- Offers practical design insights for other researchers attempting to construct their own aerial vehicles
- Demonstrates a computationally efficient implementation of ICL for lidar data translation

1.5 Thesis Organization

Chapter 2 presents fundamental background information and terminology associated with multi-rotor systems that will be used throughout this thesis. Chapter 3 overviews the the mathematical reference frame for the multi-rotor system and specifies control objectives. Chapter 4 describes sensors used for quadcopter orientation estimation as well as a fusion algorithm to combine the various sensors. Chapter 5 proposes a control system to achieve auto-leveling flight. This chapter will also overview the software architecture used in order to execute the desired control system. Chapter 6 overviews the quadcopter's radio system and introduces applicable theory required for its design and construction. Chapter 7 describes other hardware components of the quadcopter such as the flight controller and electronic speed controllers. Chapter 8 overviews lidar integration with a quadcopters control system. This chapter also specifies an algorithm for parsing lidar data under significant processing and memory constraints. Finally, chapter 9 will overview the findings of this thesis, present flight data, and discuss future work.

CHAPTER 2

Quadcopter Background Information

In order to provide context for future chapters, this chapter introduces the basic inputs and outputs common to a quadcopter system. As the name quadcopter implies, a quadcopter is a multi-rotor aircraft with four propellers. Beyond having four propellers, there is significant design diversity. This design diversity includes but is not limited to motor type and frame design. Examples of various quad-copter implementations is shown in Fig. **2.1**.

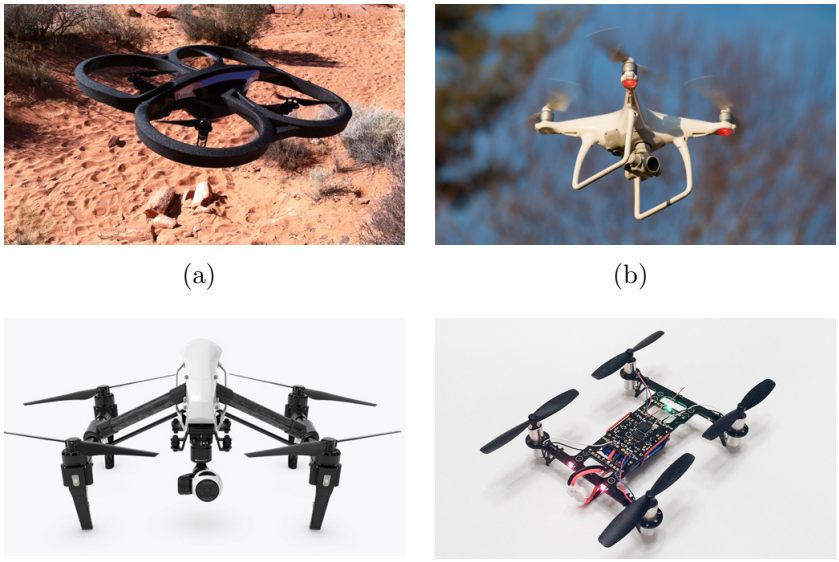

(a) (b)

(c) (d)

Figure 2.1: Examples of quadcopter implementations. Sources: (a), (b), (c), (d).

The quadcopters in Fig. **2.1** are referenced throughout this chapter as demonstrations of different types of construction. A defining aspect of these quad-copters is the motor type that they utilize. Consequently, the next section will overview the common types of quadcopter motors.

2.1 Common Quadcopter Motor Types

Low cost commercial quadcopters generally use electric DC motors such as brushed and brush-less permanent magnet motors. In contrast to gas motors, there exists small electric motors that are light weight, low cost, and of simple construction. These features make small electric motors ideal for low cost commercial quadcopters. Among these electric motors, two common types of DC electric motors exist which are brushed and brushless motors. As the name implies, brushed DC motors are mechanically commutated with a brush, are powered by DC, and are explained in detail in [15]. The control simplicity and cost of brushed DC motors makes them a popular choice for micro-size quads such as the Turnigy Micro-X shown in Fig. **2.1**(d). However, the brush which mechanically commutates the motor results in friction losses as well as limited motor life span. Consequently, larger quadcopters often use brush-less permanent magnet DC motors which are electronically commutated. Brush-less motors are also split into two common types which are sensored and sensor-less motors. Examples of these two motor types are illustrated in Fig. **2.2**.

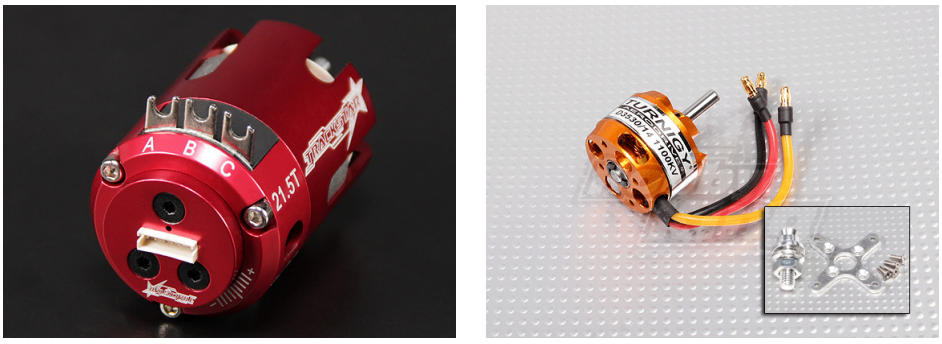

(a) (b)

Figure 2.2: Examples of sensored(a) and sensor-less(b) brush-less permanent magnet motors. Sources: (a), (b).

While brushless motors have higher performance in some areas, the cost of electronic commutation versus mechanical commutation is in greater motor driving complexity. In

order to electronically commutate a permanent magnet motor, the rotors position must be known. This can be achieved by using hall effect sensors or by using sensor-less driving techniques. Common sensor-less techniques include back EMF zero-cross detection as well as field oriented control [16],[17]. Sensor-less operation is desired since sensor-less motors have reduced weight as well as cost. As a result of this, sensor-less brush-less motors are common in quadcopters. However, in order to drive these motors, a DC to AC 3 phase sensor-less motor driver is needed. In terms of popular multi-rotor vernacular, these are commonly referred to as electronic speed controllers (ESC).

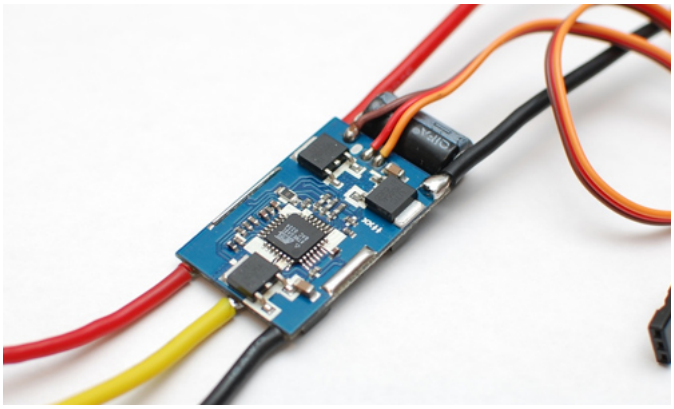

Figure 2.3: Example of ESC. Source:(1).

These ESCs represent an integral part of the quadcopter system architecture since their output indirectly controls the orientation of the quadcopter by varying the speed of the propellers. These devices will be discussed in greater detail in chapter 7.

2.2 Quadcopter Configurations and Frame Design

Quadcopters have various configurations though the most common types are the **X** configuration, the **H** configuration, and the + configuration. These various configurations are illustrated in Fig. **2.4**.

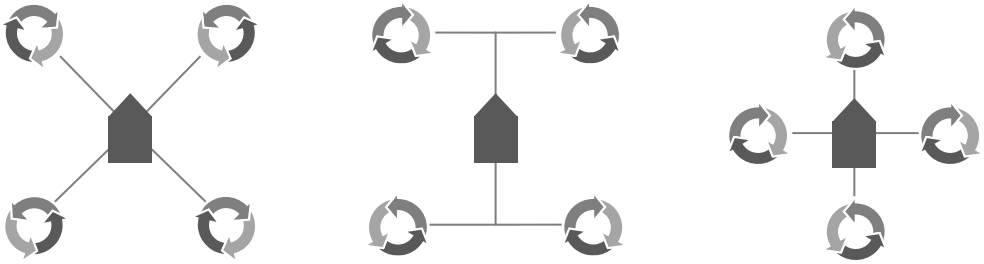

(a) (b) (c)

Figure 2.4: (a): **X**, (b): **H**, (c): + configuration quadcopters

Each type of configuration offers advantages and dis-advantages. The **X** configuration is the most commonly utilized motor configuration since it is simple to construct, ideal for a forward facing camera, and is symmetrical about both the x and y axis. Quadcopters in Fig. **2.1**(a,b,c) are using this type of configuration. A disadvantage of this configuration is an increase in control complexity. In contrast to the **X** configuration, the + configuration is the simplest to mathematically model and control. However, this configuration is least ideal for a forward facing camera. Consequently, very few commercial drones are sold in this configuration and they generally only appear in research or DIY projects. Finally, the **H** configuration is sometimes built for mechanical convince as seen in Fig. **2.1**(d). In contrast, the DJI Inspire in Fig. **2.1**(c) was designed as a **H** configuration quadcopter to achieve improved camera perspective [18]. While this configuration can be ideal for forward facing cameras, it is also not symmetrical about the quadcopters x and y axis. This lack of symmetry should be taken into account and will be discussed later in this thesis. These three configurations including minor deviations represents the majority of quadcopter configurations in common use today.

2.3 Quadcopter System Architecture

A final step in presenting necessary background information for this quadcopter thesis is to briefly overview of the electrical architecture. This architecture is presented in a block diagram form in Fig. **2.5**.

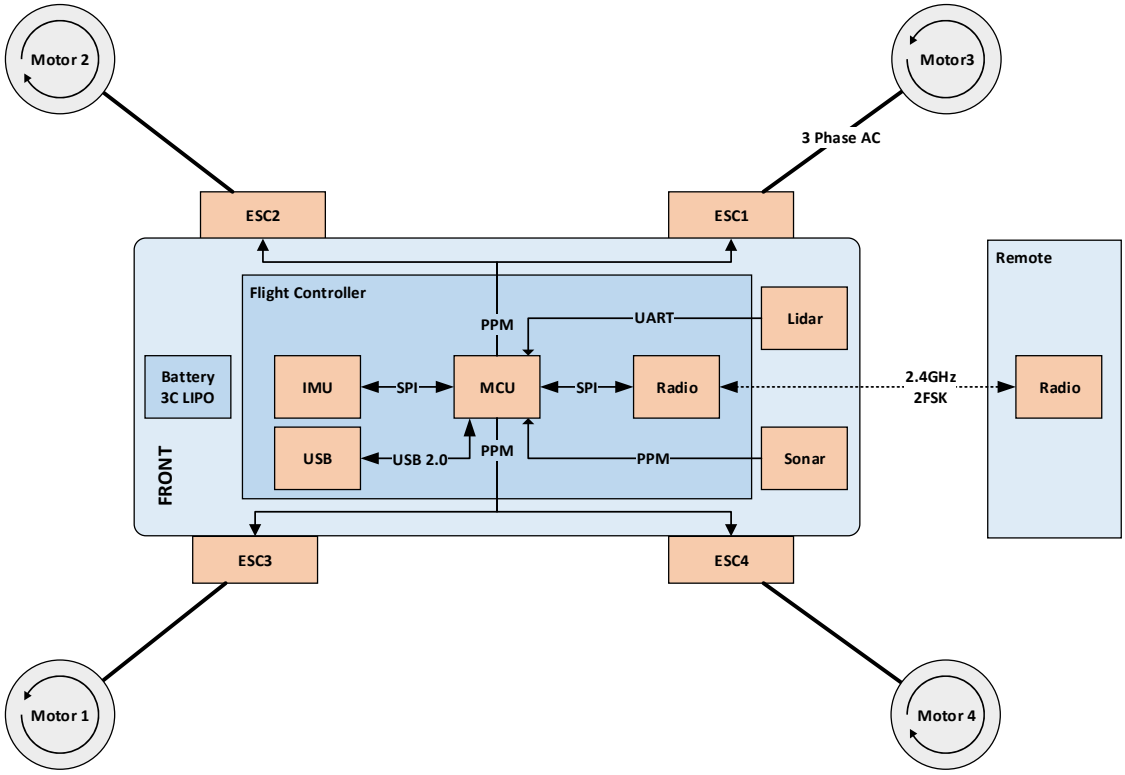

Figure 2.5: Marq Drone electrical architecture.

The underlying system for the quadcopter in this thesis was nammed the "Marq Drone" system. This system consists of a flight controller, a radio, and ESCs. Core components of the flight controller include a micro-controller unit(MCU), a radio, and an inertial measurement unit(IMU). Externally, the flight controller communicates with the ESCs and sonar through pulse position modulation(PPM). In addition, the flight controller communicates with a lidar sensor through a universal asynchronous receive and transmit

(UART) interface. To communicate with devices external to the quadcopter, a USB interface can be used for data acquisition or programming. Another method communication is through a wireless 2.4GHz frequency shift keyed(FSK) interface.

Now that all the components involved have been introduced, the I/O of the system can be identified. For the flight controller itself, feedback inputs are from the IMU, sonar, and lidar sensors. The outputs of the system are the four individual PPM signals that are sent to the ESCs. Now that the I/O of the system has been briefly introduced, a control scheme will be derived that uses these I/O to achieve stable flight.

CHAPTER 3

Control Goal and Orientation Establishment

In this chapter, a control goals will be presented for the quadcopter in addition to a reference coordinate system. Like other multi-rotor vehicles, the primary control objective is to keep the quadcopter's orientation controlled and its altitude above ground non zero. With this in mind, a common reference coordinate system will be presented to explicitly define this control objective.

3.1 Quadcopter's Reference Frame

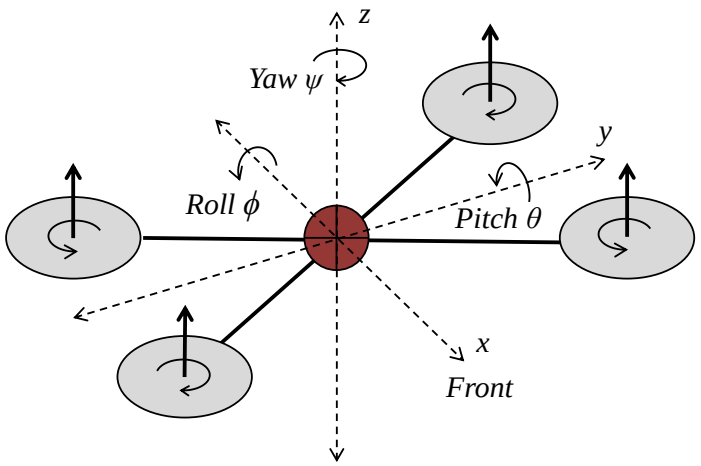

Figure 3.1: Quadcopter reference frame

Fig. 3.1 demonstrates a common reference frame for multi-rotor vehicles. The quadcopter exsits in a Cartesian x,y,z plane and uses Euler angles pitch(θ), roll(ϕ), and yaw(ψ) to denote its orientation.

3.2 Control Objective

A primary control objective for the quadcopter is to be able command a stable orientation of the quadcopter. With this in mind, the first set of control goals can then be summarized in equation **3.1** where θ_c, ϕ_c, ϕ_c represent a user commanded rotation, where $\dot{\theta}, \dot{\phi}, \dot{\psi}$ represent the rotational velocities of the quadcopter, and where T_c represents the user commanded throttle.

$$\begin{aligned} &\dot{\theta} = 0 \qquad \dot{\phi} = 0 \qquad \dot{\psi} = 0 \\ &\theta \to \theta_c \qquad \phi \to \phi_c \qquad \psi \to \psi_c, \qquad T \to T_c \end{aligned} \tag{3.1}$$

These control parameters, $\theta_c, \phi_c, \psi_c, T_c$, allow a user to drive the quadcopter to anywhere in three dimensional space. Consequently, many commercial systems give users these four degrees of freedom to operate a quad-copter. However, the user must also act as a control system in order to regulate the quadcopters height to keep it above the ground. To achieve this, the user must observe the quadcopters height and constantly re-adjust the throttle, T_c, such that the height with respect to ground, z, is roughly constant. Also, if a user desires a quadcopter to stay at a fixed position in space, they must also observe the x, y position of the drone and adjust θ, ϕ accordingly such that the quadcopter remains at a fixed position.

While these parameters allow a user to control a drone, these four degrees of freedom are not enough for stable autonomous flight. Without a user to observe and control the quadcopters x, y, z position with respect to the room, stable flight is not possible. Therefore as a secondary control objective, equation **3.2** demonstrates the control needed for autonomous

flight.

$$\begin{aligned} \dot{x} = 0, \qquad \dot{y} = 0, \qquad \dot{z} = 0 \\ x \to x_c \qquad y \to y_c \qquad z \to z_c \end{aligned} \tag{3.2}$$

To meet the autonomous control objectives in equation **3.2** , additional sensors are needed such as lidar, GPS, and sonar. These methods will be introduced at a later point in this thesis.

3.3 Purpose of Mathematical Derivation

Other than being a stimulating mental exercise, a mathematical derivation of a multi-rotor frame provides a basis for update laws and helps a designer gain intuition regarding their system. While in simple cases, these update laws can be derived from simple inspection of the airframe, this method becomes less effective as motor count is increased, as asymmetries are introduced to the air frame, and as motor angles are changed. Consequently, the incentive of the following sections is to translate motor thrust($[T_0, T_1, T_2, T_3]$) to angular velocities($\dot{\theta}, \dot{\phi}, \dot{\psi}$) such that our control system can drive pitch(θ), roll(ϕ), and yaw(ψ) to their desired values.

3.4 Mathematical Model

Now that control goals have been defined for user assisted quadcopter flight, a model of the quadcopter must be derived to meet the purposed goals. For this thesis, a modified **X** configuration quadcopter design was selected. This was chosen for mechanical convenience and mounting simplicity. A diagram shown in fig. **3.2** dimensions this modified **X**

configuration quadcopter.

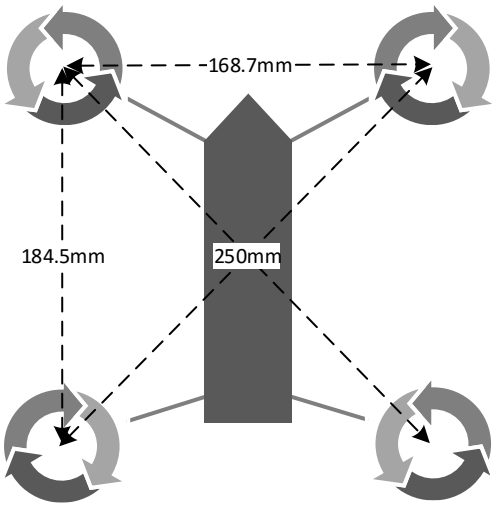

Figure 3.2: Mechanical demensions of quadcopter

These dimensions are relevant to the physics based model derivation. Note that this quadcopter is not symmetrical about its X and Y axis. Now that the dimensions have been presented, Fig. **3.3** demonstrates a more detailed free body diagram of forces and torques acting upon the quadcopter.

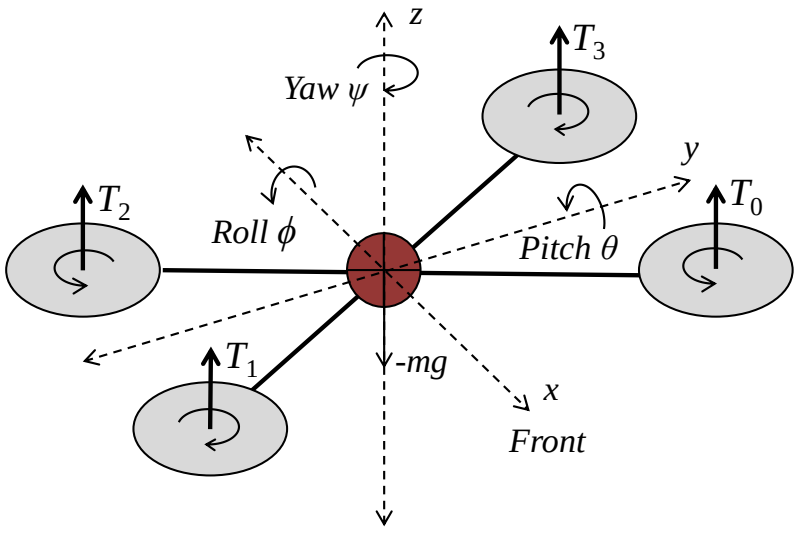

Figure 3.3: Quadcopter free body diagram

The dominate force acting on the quadcopter is naturally mass·gravity. To counteract this, force vectors are produced from the propellers.

3.4.1 Forces

Propellers produce a force orthogonal to their rotation. It follows that this force is proportionally related to the propeller's speed. It can be shown that an approximation of propeller the thrust force is as follows in equation **3.3** where T_i is a force vector for motor index i, where k is a scaling constant, and where ω is the angular velocity of the propeller[19].

$$T_i = k \cdot \omega^2 \tag{3.3}$$

The sum of thrust force vectors, T, is shown in equation **3.4** where $\bar{x}, \bar{y}, \bar{z}$ are Cartesian unit vectors.

$$T = \sum_{i=1}^{4} T_i = k \cdot \begin{bmatrix} 0 & 0 & \omega^2 \end{bmatrix} \cdot \begin{bmatrix} \bar{x} \\ \bar{y} \\ \bar{z} \end{bmatrix} \tag{3.4}$$

Note that all these forces are in the $\bar{z}$ direction. The implication of this is that the quadcopter cannot transverse a room's x, y plane without some rotation. This has aerial footage implications which is why some multi-rotor platforms use angled motors as seen here[20]. Another important note is that while a ESC is aware of motor speed, ESCs do not commonly send this information back to a controller. ESCs are simply a black box in which

a PPM signal is sent to. Without taking external measurements, it is not possible to accurately correlate a PPM signal to propeller's velocity or thrust. To approximate the PPM signal to thrust relationship, the quadcopter was put upside down on a weight scale, tared, and then varying PPM signals were sent to the motors. The results of this testing are shown in Fig. **3.4**.

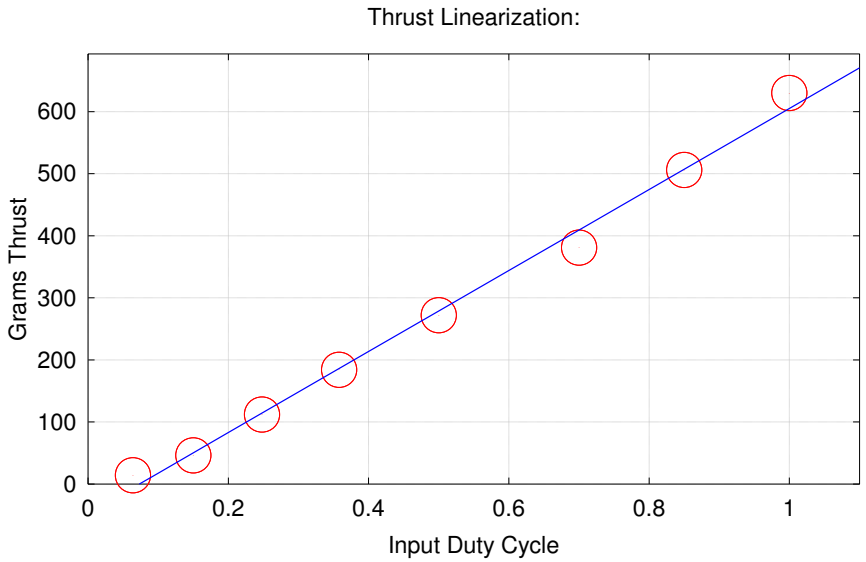

Figure 3.4: Thrust per Duty Cycle Input

As observed in Fig. **3.4**, there was a roughly linear relationship between input duty cycle and thrust. Consequently, a simple linear regression was used to approximate the thrust for a given motor in terms of the PPM duty cycle as shown in equation **3.5**.

$$\hat{T}_i = 652.82 \cdot PPM_i - 47.68. \tag{3.5}$$

Naturally this equation only applicable to this specific combination of propellers and motors. This experiment would need to be performed again should the motors or propellers change. Now that an estimate T_i has been formulated, it is now possible to calculate the required thrust to keep the quadcopter in the air.

$$\sum_{i=1}^{4} \hat{T}_i \cdot \bar{z} = m \cdot g$$
$$\bar{z} = cos(\theta) \cdot cos(\phi) \tag{3.6}$$
$$\hat{T}_i = \frac{m \cdot g}{4 \cdot cos(\theta) \cdot cos(\phi)}$$

Assuming $\hat{T}_i$ is set equal to the result calculated in equation **3.6**, the quadcopter should roughly maintain its height regardless of minor rotations in θ, ϕ. However, it is important to note that thrust vectors T_i occur at some r_i distance away from the center of mass which results in torques acting on the frame.

3.4.2 Torques

From physics, we know that torque, τ, is equal to the cross product of distance and force. For control purposes, it is useful to calculate the torque for each of the quad-copters rotation axes as seen in equation **3.7**. In equation **3.7**, height (h) and length (l) are defined from Fig. **3.2**.

$$\tau = r \times F$$
$$\tau_\theta = r_{\bar{x}} \times T = (h/2) \cdot (T_0 + T_1 - T_2 - T3) \tag{3.7}$$
$$\tau_\phi = r_{\bar{y}} \times T = (l/2) \cdot (T_0 + T_3 - T_1 - T_2)$$
$$\tau_\psi = a \cdot (T_0 + T_2 - T_1 - T_3).$$

As observed in equation **3.7**, the pitch and roll torques (τ_θ, τ_ϕ) are defined with respect to the quadcopter's frame geometry. Had the quadcopter frame been symmetrical, l, h would have been equal which would have resulted in a simpler equation. Without taking this asymmetry into account at the control system level, the quadcopter's pitch and roll would

react differently. In contrast to τ_θ, τ_ϕ, it is harder to define the torque about the yaw axis(τ_ψ) geometrically. This torque is slightly less intuitive because it arises from having spinning masses attached to the frame. Without taking this into account, the quadcopter would continuously spin about the yaw axis. However, this problem is not unique to just quadcopters. A helicopter, for example, uses a tail rotor in order to counteract the yaw torque introduced by the primary blade. Similarly, in order to counteract this torque on the quadcopter frame, two propellers are selected to spin clock wise and two propellers are selected to spin counter clockwise. These alternating motor directions are illustrated in Fig. **3.3**. While geometry and force vectors have allowed for derivations of torque, these cannot be converted to angular rates without observing inertia.

3.5 Inertia and Angular Acceleration

Classical physics defines a relationship between torque and angular acceleration as shown in equation **3.8** where ω is angular velocity, where $\alpha, \dot{\omega}$ represent angular acceleration, and where I_{xyz} represents the inertia matrix.

$$\tau = I_{xyz} \cdot \alpha = I_{xyz} \cdot \dot{\omega} = \begin{bmatrix} I_{XX} & I_{XY} & I_{XZ} \\ I_{YX} & I_{YY} & I_{YZ} \\ I_{ZX} & I_{ZY} & I_{ZZ} \end{bmatrix} \cdot \begin{bmatrix} \dot{\omega}_x \\ \dot{\omega}_y \\ \dot{\omega}_z \end{bmatrix} \tag{3.8}$$

The angular accelerations can be solved for by equating equation **3.8** to equation **3.7**. Furthermore, taking the time derivative yields angular velocity. Also note at an instant in time, $\omega_x, \omega_y, \omega_z$ is equal to $\dot{\phi}, \dot{\theta}, \dot{\psi}$ respectively.

$$\begin{bmatrix} \dot{\phi} \\ \dot{\theta} \\ \dot{\psi} \end{bmatrix} = I_{xyz}^{-1} \cdot \begin{bmatrix} (h/2) \cdot (T_0 + T_1 - T_2 - T3) \\ (l/2) \cdot (T_0 + T_3 - T_1 - T_2) \\ a \cdot (T_0 + T_2 - T_1 - T_3) \end{bmatrix} \cdot \Delta T \tag{3.9}$$

Consequently, to calculate angular velocity, the inertia tensor matrix must be known. Note, if rotations are defined about an objects center of mass and the mass is symmetrically distributed, the inertia matrix is diagonal[21]. Note this is an approximate since in reality, the mass will not be distributed perfectly symmetrically. Using this approximation and factoring in our already calculated thrust equations results we can calculate the four degrees of freedom in terms of motor thrusts as shown in equation **3.10**.

$$\begin{bmatrix} \dot{\phi} \\ \dot{\theta} \\ \dot{\psi} \\ T \end{bmatrix} = \begin{bmatrix} \frac{h \cdot \Delta T}{2 \cdot I_{XX}} & \frac{h \cdot \Delta T}{2 \cdot I_{XX}} & -\frac{h \cdot \Delta T}{2 \cdot I_{XX}} & -\frac{h \cdot \Delta T}{2 \cdot I_{XX}} \\ \frac{l \cdot \Delta T}{2 \cdot I_{YY}} & \frac{-l \cdot \Delta T}{2 \cdot I_{YY}} & \frac{-l \cdot \Delta T}{2 \cdot I_{YY}} & \frac{l \cdot \Delta T}{2 \cdot I_{YY}} \\ \frac{a \cdot \Delta T}{I_{ZZ}} & \frac{-a \cdot \Delta T}{I_{ZZ}} & \frac{a \cdot \Delta T}{I_{ZZ}} & \frac{-a \cdot \Delta T}{I_{ZZ}} \\ \frac{m \cdot g}{4 \cdot cos(\theta) \cdot cos(\phi)} & \frac{m \cdot g}{4 \cdot cos(\theta) \cdot cos(\phi)} & \frac{m \cdot g}{4 \cdot cos(\theta) \cdot cos(\phi)} & \frac{m \cdot g}{4 \cdot cos(\theta) \cdot cos(\phi)} \end{bmatrix} \cdot \begin{bmatrix} T_0 \\ T_1 \\ T_2 \\ T_3 \end{bmatrix} \tag{3.10}$$

These equations will form the basis of the control system update laws. However, in order to apply them, the orientation of the quadcopter must be known.

CHAPTER 4

Flight Orientation Estimation

4.1 Introduction

In order to meet the control goals purposed in **3.1** , estimation of the quad-copter's orientation is required. With modern advancements in electronics, determining attitude can be done cheaply, efficiently, and quickly with MicroelEctricalMechancial Systems (MEMS) based sensors. Unfortunately, currently, there is no single affordable MEMS sensor that directly measures θ, ϕ, ψ. Consequently, the combination of multiple MEMS sensors is required in order to accurately estimate orientate. This chapter will individually overview MEMS sensors individually and overview their strengths and weaknesses with respect to multi-rotor aircraft. We will then establish the minimum amount of sensors to achieve the desired goal.

4.2 3 Axis Accelerometer

4.2.1 Introduction

3 axis accelerometers are devices that are designed to measure Cartesian $\bar{x}, \bar{y}, \bar{z}$ acceleration. It follows that the output of the device is a Cartesian acceleration vector denoted as $A = [A_x, A_y, A_z]$. Fig. **4.1** is a macro scale illustration of how accelerometers measure

acceleration.

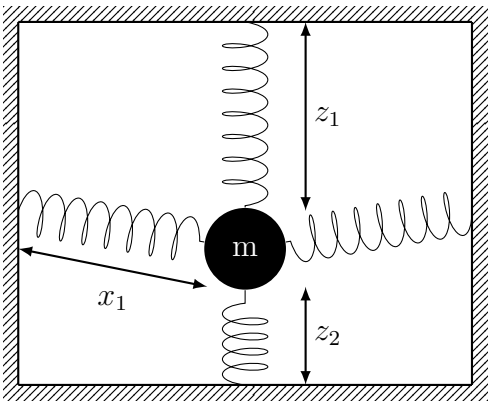

Figure 4.1: 2D macro scale spring accelerometer.

$$F = m \cdot A, \quad F = k \cdot z$$
$$A_z = \frac{k \cdot (z_1 - z_2)}{2 \cdot m} \tag{4.1}$$

In Fig. **4.1** a mass is suspended by springs. Acceleration acting on the mass is determined by spring deflection. Due to gravity, an accelerometer will state that an object at rest is experiencing an acceleration approximately $9.8m/s^2$. This acceleration is represented in Fig. **4.1** with the deflection of the z springs. This gravity reference is crucial for steady state orientation estimation. Also, note that in the illustration, the x dimension springs are also experiencing deflection due to gravity but their magnitudes of deflection are equal. Consequently when using equation **4.1**, the net acceleration in the $\bar{x}$ direction would be 0 when at rest. Given one is using a 3D Accelerometer, similar equations to equation **4.1** can be derived for A_x and A_y.

4.2.2 3D MEM Accelerometer

In order to achieve low form factor, low power consumption, and low cost, most modern accelerometers are designed using MEMS based technology. While they operate under the

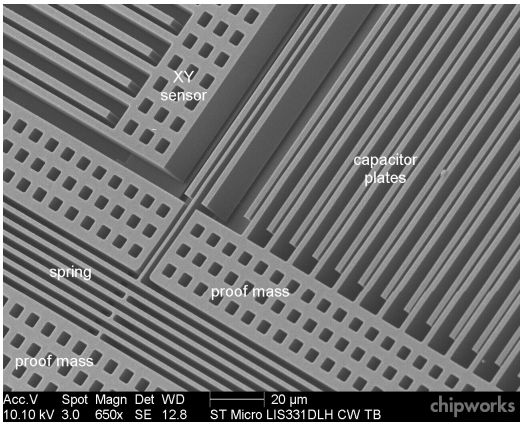

Figure 4.2: Accelerometer MEMs image. Image Source: (1)

same principles illustrated in Fig. **4.1**, there is little visual similarity since the springs are often of micron size etched in a silicon based process. Fig. **4.2** is a picture of the internals of a modern MEMs accelerometer. These structures take a variety of shapes although they generally consist of spring loaded masses in combination with parallel plates. As acceleration is applied to the MEMS structure, the distance between the plates changes. Consequently, the device then measures the capacitance of the plates and converts the result to an acceleration [22]. The accelerometer can then transmit this acceleration value through a serial bus or an analog signal.

4.2.3 Accelerometer Orientation Equations

To make use of accelerometer readings with respect to orientation, a conversion from Cartesian acceleration Euler angles is required. It can be shown that with equation **4.2** and equation **4.3** that we can convert from Cartesian acceleration to Euler angles θ and ϕ [23].

$$\theta = atan\left(\frac{A_x}{\sqrt{A_y^2 + A_z^2}}\right) \cdot \frac{180}{\pi} \tag{4.2}$$

$$\phi = atan2\left(\frac{A_y}{A_z}\right) \cdot \frac{180}{\pi} \tag{4.3}$$

Note that in the case of ϕ in equation **4.3**, the $atan2$ function is used which is a four quadrant version of the traditional arc tangent function. Also note that there is no yaw(ψ) equation listed. This is a fundamental physical limitation of the 3 Axis Accelerometer.

4.2.4 Accelerometer Drawbacks

1. Incomplete Orientation Assessment

While vectors contain magnitude and directional information, they do not intrinsically have a rotational component. It follows that the yaw(ψ) of a given object cannot be determined with a 3 axis accelerometer. Consequently, sole use of an accelerometer does not allow for the control goals **3.1** to be achieved. Without yaw feedback, any unbalanced ψ torques about the quad-copter would result in the aircraft spinning undetected in air. Naturally, this would make navigation difficult and it follows that the accelerometer is not generally used as a stand alone orientation sensor for multi-rotor aircraft.

2. Sensitive to High Frequency Vibrations

Another noteworthy issue with accelerometers is that they are sensitivity to high frequency vibrations. While this is not an issue for some applications, quadcopters often experience a high level of vibration due to their motors spinning at high RPMs. The affect that this can have is illustrated in Fig. **4.3**.

As seen in Fig. **4.3**, when at rest there is negligible noise on the accelerometer readings. However, when the quadcopter's motors are turned on, a significant amount of high

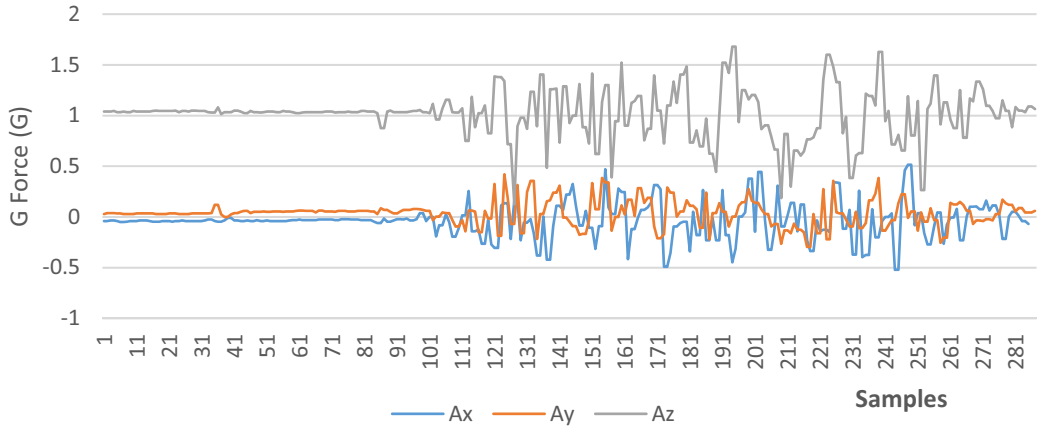

Figure 4.3: Accelerometer noise before and during motor operation

frequency noise is registered on the sensor. While low pass filtering would remove this noise, the delay of such a filter can lead to flight instability.

3. External acceleration produces unknown orientation

Accelerometers measure a gravity reference when an object at rest. However, the accuracy of this reference can be lost if the quadcopter is accelerating. For example, if the quadcopter in Fig. **3.3** is moving upwards at a rate twice that of gravity, the accelerometer would yield $A_z = -1g, A_x = 0g, A_y = 0g$. Using this data, equation **4.3** would state that the quadcopter is upside-down. Consequently, equation **4.3** is only valid and useful for orientation when the quadcopter is not accelerating.

4.3 3 Axis Gryoscope

4.3.1 Introduction

In contrast to the accelerometers, gyroscope measures rotation. For decades, gyroscopes have been used as an integral part in naval and areospace navigation. The first gyroscopes were generally spinning masses held in a gimbal frame. These frames allowed the mass to

spin freely and maintain its axis of rotation regardless of the mounting of the external frame. Due to angular momentum, the spinning mass would resist any changes to its rotation. This structure is visualized in Fig. 4.4 .

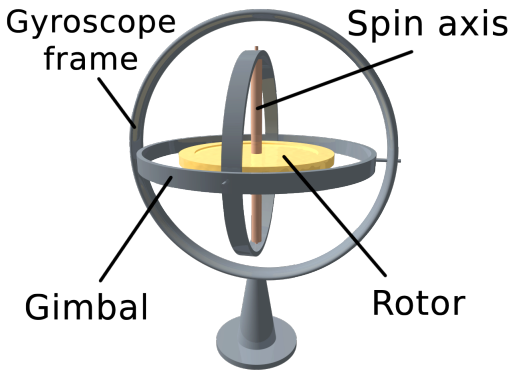

Figure 4.4: Classical Gyroscope

To electronically measure changes in rotation using a classical gyroscope, electrical potentiometers are connected to the gimbal frames. While these devices are capable of a large degree of accuracy, they are large, heavy, and expensive.

4.3.2 MEMs Gyro

A MEMS version of the gyroscope is illustrated in Fig. 4.5. Due to the silicon design process, they are small, low power, and cost effective.

Unlike the macro version shown in Fig. 4.4, MEMS gyroscopes do not contain a spinning disk. Owing to the fact that it is difficult to achieve a large angular momentum in a microscopic space, MEMS gyroscopes operate on a different physical principle. This physics principle is called the "coriolis effect" [24]. Consequently, these types of gyros are called "Coriolis vibratory gyroscopes". As the name suggests, these contain vibrating structures. By measuring forces exerted on these vibrating structures, velocity of rotation can be determined [25]. It important to note that MEMS gyroscopes measure velocity in contrast

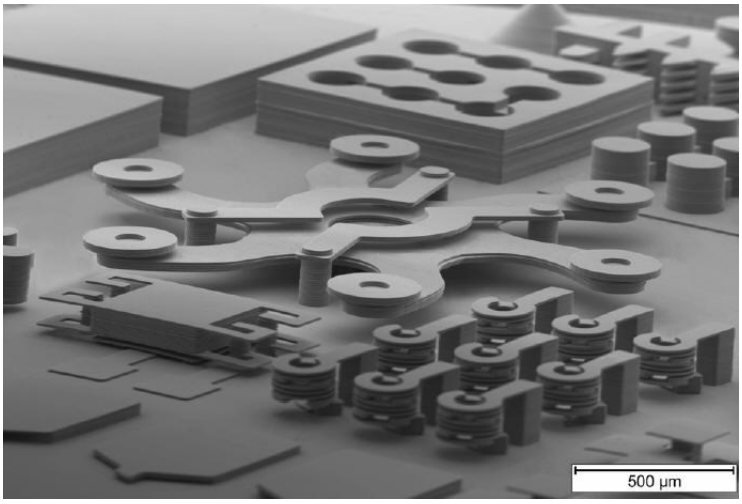

Figure 4.5: MEMS 3 Axis Gyroscope. Image Source: (1)

to macro-scale gyroscopes that measure orientation angles directly. To estimate orientation angles, it follows that the MEMS gyroscope readings must be integrated as shown in equation **4.4**.

$$\theta = \int_0^t \dot{\theta} \cdot d\theta \qquad \phi = \int_0^t \dot{\phi} \cdot d\phi \qquad \psi = \int_0^t \dot{\psi} \cdot d\psi \tag{4.4}$$

4.3.3 MEMs Gyro Drift

As a result of integrating the readings MEMS gyroscope over time, steady state orientation error accumulates. This accumulated error is commonly called gyro drift. As a result, a MEMS gyroscope must continuously be re-calibrated or must be high pass filtered. Consequently, MEMS gyroscopes are often used in combination with other sensors.

4.4 3 Axis MEMS Magnetometer

4.4.1 Introduction

Magnetometers are devices that measure magnetic field. The most common and oldest form of a magnetometer is a compass. Compasses, which point in the direction of earth's magnetic north, have been used in navigation for hundreds of years. For modern low power electronics, a MEMS solution also exists. An example of a MEMS magnetometer is shown in Fig. **4.6**.

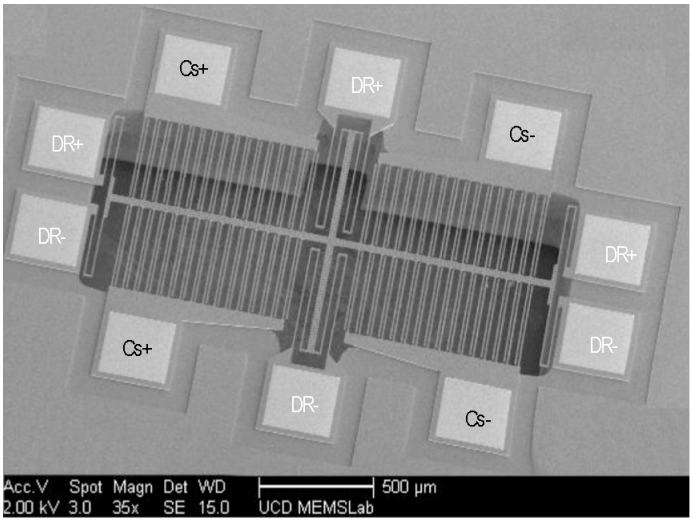

Figure 4.6: MEMS 3 Axis Magnetometer. Image Source: [1]

Common MEMS magnetometers function by making use of the Lorentz force in order to measure magnetic field [1]. This force is then converted to a electronic signal similarily to how an accelerometer measures acceleration. This force creates deflection on a spring system which is sensed by parallel capacitive plates. Primarily, these sensors are used to measure the earths magnetic field which gives orientation insight. When these devices are used in conjuntion with an accelerometer, steady state estimation accuracy of θ, ϕ, ψ can be achieved. While these devices can provide useful insight into orientation, they also have their own drawbacks.

4.4.2 Hard-Iron and Soft-Iron Interference

A magnetometer's proximity to both ferrous and non ferrous metal is a large source of error. These errors are called hard-iron and soft-iron interference for ferrous and non ferrous materials respectively [26]. Electronic assemblies intrinsically contain both types of material and consequently are susceptible to both as soon as a magnetometer is bonded to a PCB. Unfortunately, since the earths magnetic field is weak, these errors can dominate the output readings of a magnetometer.

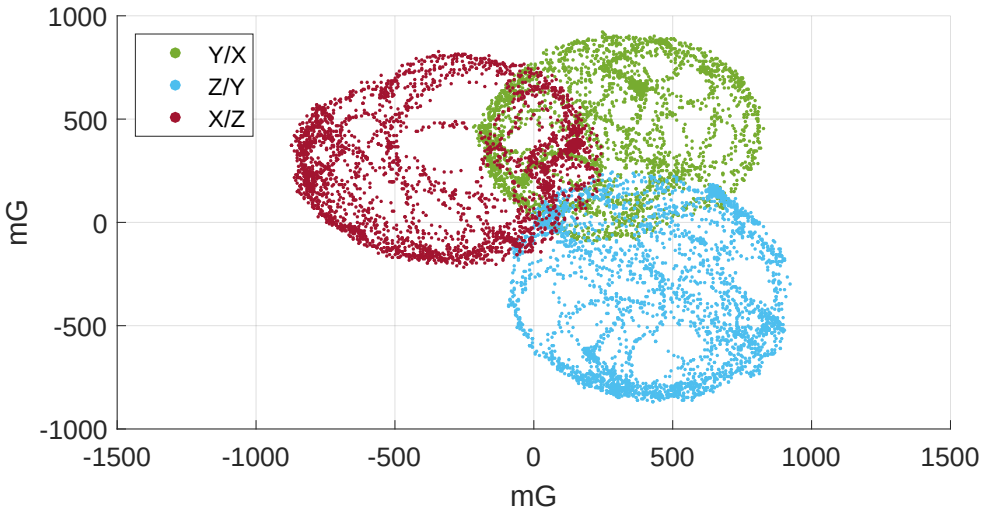

Figure 4.7: Milli-Gauss(mG) output of an uncalibrated magnetometer when rotated in 3 Dimensions

Consequently, for magnetometer readings to be valid, a calibration must be done after a magnetometer has been bonded to the PCB. The uncalibrated magnetometer readings observed on the quadcopter is illustrated in Fig. **4.7**. For practical purposes, a simple offset and scaling calibration can be performed. A method of performing this scaling is shown in equation **4.8** where M_x, M_y, M_z represents the milli-Gauss values on their respective axises.

$$\hat{M}_x = 2 \cdot \frac{M_x - min(M_x)}{max(M_x) - min(M_x)} - 1$$
$$\hat{M}_y = 2 \cdot \frac{M_y - min(M_y)}{max(M_y) - min(M_y)} - 1 \tag{4.5}$$
$$\hat{M}_z = 2 \cdot \frac{M_z - min(M_z)}{max(M_z) - min(M_z)} - 1$$

Note that this calibration procedure should only be performed during a window of time in which the quadcopter is being rotated about all its axies. If a windowed calibration is not performed, eventually the min and max values will be corrupted by external fields and will permanently skew the values of M_x, M_y, M_z. This calibration procedure was performed on the quadcopter's IMU and the results can be seen in Fig. **4.8**.

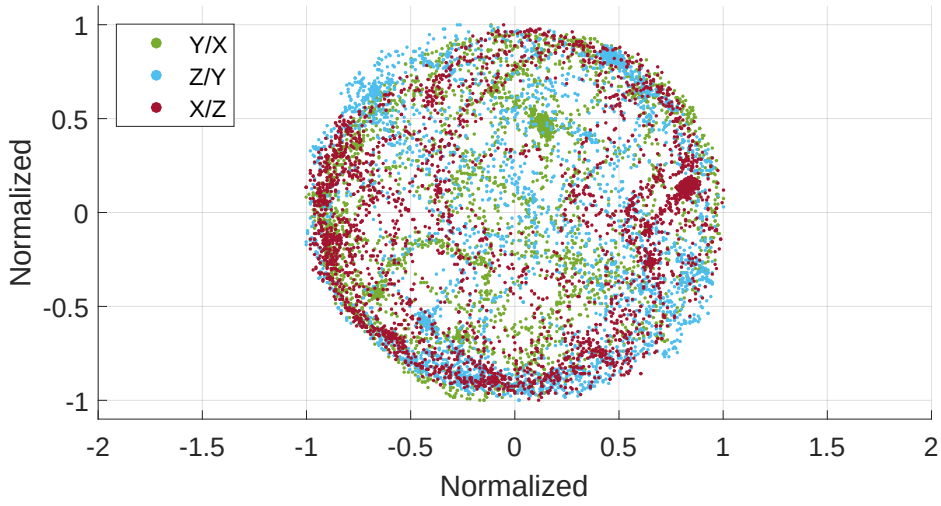

Figure 4.8: Milli-Gauss(mG) output of an calibrated and normalized magnetometer when rotated in 3 Dimensions

As seein in Fig. **4.8**, the magnetomer data is normalized and no longer has significant scaling or offset varation between the axises. However, this calibration procedure does convert the output from milli-Gauss to a unitless value. This loss of information is of little value since subsequent calculations will all be based upon trigonometry. For example, assuming the quadcopter is level ($\theta = 0, \phi = 0$), yaw (ψ) can be calculated with the basic

equation shown in equation **4.6**.

$$\psi = atan2(\frac{\hat{M}_y}{\hat{M}_x}) \tag{4.6}$$

Note this equation is no longer valid if the quadcopter is not level

4.4.3 Magnetomer Tilt Compensation

Magnetomer yaw accuracy can be improved by performing tilt compensation based upon θ, ϕ [27]. The end goal of tilt compensation is to make equation **4.6** valid by de-rotating the axises by θ, ϕ. Using rotation matrices along with equation **4.6**, equation **4.7** is derived.

$$\hat{\psi}_C = tan^-1\left(\frac{\hat{M}_z \cdot sin(\phi) - \hat{M}_y \cdot cos(\phi)}{\hat{M}_x \cdot cos(\theta) + \hat{M}_y \cdot sin(\theta)sin(\phi) + \hat{M}_z \cdot sin(\theta)cos(\phi)}\right) \tag{4.7}$$

For this equation to work properly, it is imperative that all IMU outputs match the axis as shown in Fig. **3.1**. This equation was validated with IMU data and a comparison between compensated and uncompensated yaw is shown in Fig. **4.9**.

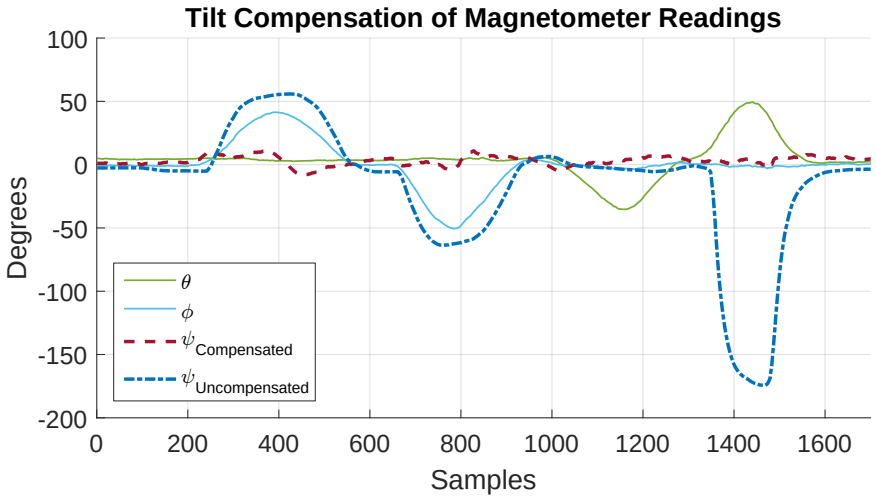

Figure 4.9: Plot demonstrating successful tilt compensation of magnetometer readings. Here θ and ϕ are actuated without significant change in ψ_C.

4.4.4 Magnetometer Drawbacks

Susceptible to external fields

As mentioned previously, the earths magnetic field is extremely weak. Consequently, external ferrous material can significantly skew orientation readings if in close proximity to the sensor. A method that was implemented to combat this is to ignore the magnetometer data if the data observed is significantly beyond the normalization in Fig. **4.8**.

Global Location Dependent

Earth's magnetic field direction and strength vary across the surface of the earth. The earths magnetic field vector points towards magnetic north as opposed to the true geographical north. The angular difference between these two locations is defined as magnetic declination. In addition, the earths magnetic field has a varying vertical component. The angular difference between the surface of the earth and the earths magnetic field is defined as magnetic inclination. This is illustrated in Fig. **4.10** where σ is magnetic declination and where δ is magnetic inclination.

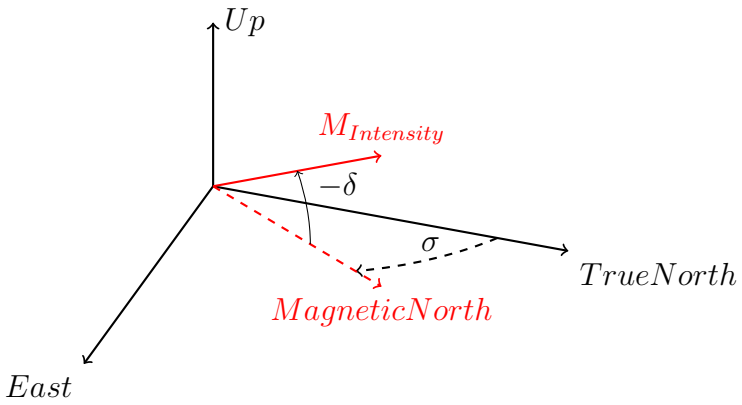

Figure 4.10: Demonstration of magnetic intensity (M), magnetic inclination (δ), and magnetic declination (σ)

Geographical variations in magnetic intensity, inclination, and declination are shown in Fig. **4.11**.

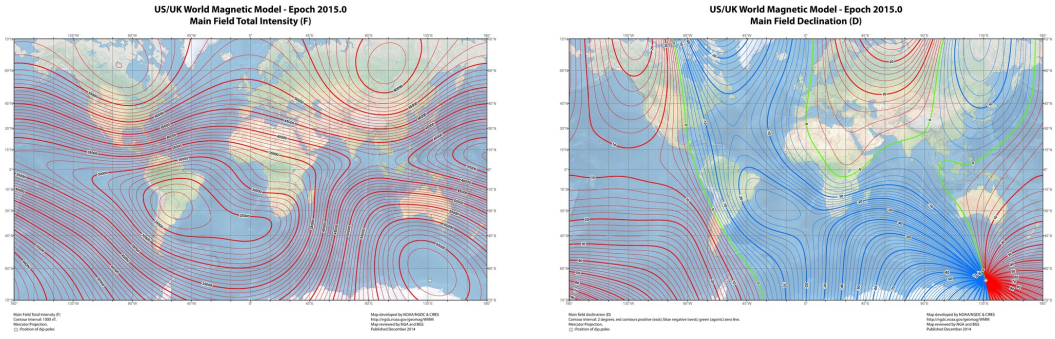

(a) (b)

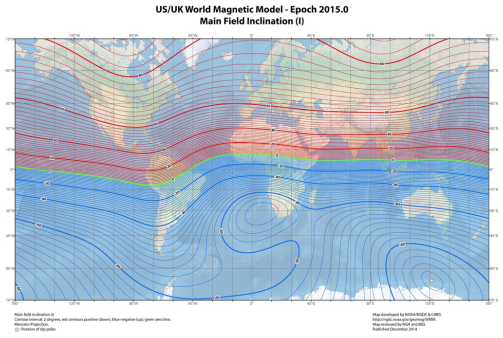

(c)

Figure 4.11: Global variation in: (a) magnetic intensity, (b) magnetic declination, (c) magnetic inclination. Image Source: (a),(b),(c).

These variations have implications for quadcopter flight. Variations in field strength would affect the results of the calibration procedure in equation **4.8**. Consequently, the quad copter should be re-calibrated per continent of operation. Variations in magnetic declination do not actively affect user operated flight. However, absolute heading error can have implications in autonomous flight. However, if the quadcopter's location is known, the map in Fig. **4.11**(b) can be used for correction. Finally, magnetic inclination can be accounted for likewise using the map in Fig. **4.11**(c). Another method of compensating for magnetic inclination is to use the equation in equation **4.7** which effectively ignores the z component of the magnetic field.

4.5 Sensor Fusion

4.5.1 Introduction

The process of combining data from multiple sensors and coming up with a collective estimate is commonly called sensor fusion. For orientation, there are multiple different sensor fusion algorithm techniques such as gradient descent and Kalman filtering[28]. However, due to the high frequency vibrations, large system accelerations, low computational power available, and fast control loop update requirements, not all algorithms are ideal for quadcopter flight use. With this in mind, a simple complementary filter was selected. This work was inspired by [29]

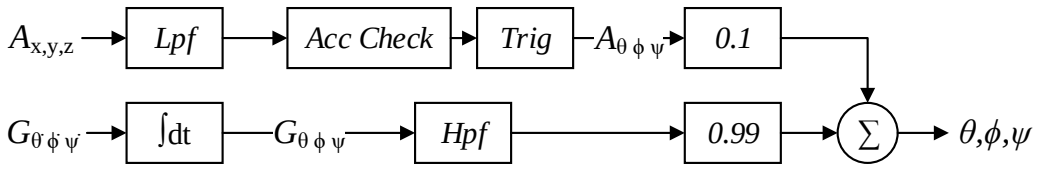

Figure 4.12: Complimentary filter acting on raw accelerometer and gyro inputs

A block diagram representation of a basic complimentary filter is shown in Fig. **4.12** where $A_{x,y,z}$ is the raw accelerometer data and $G_{\dot\theta,\dot\phi,\dot\psi}$ is the raw gyroscope data. This filter addresses weaknesses such as what was addressed in 4.2.4 and 4.3.3. While gyroscopes have good dynamic response and noise immunity, they have long term drift. In contrast, accelerometers have poor dynamic response but are not susceptible to drift in the same manner. Consequently, a high pass filter is used on the gyroscope data and a low pass filter is used on the accelerometer data. However, before the data is combined, it is important to verify validity of the accelerometer data as mentioned in 4.2.4. Also, before combing the gyroscope and accelerometer data, the accelerometer Cartesian vectors must be converted to

angles using equation **4.2**.

However, a weakness of this filter is that it does not incorporate a magnetometer and would consequently have steady state ψ error. To counteract this, a magnetomer can be added using equation **4.8**. This data can be fused with the gyroscope reading of ψ in the same complimentary fashion as to how the accelerometer and gyro data were fused. This filter is illustrated in block diagram form in Fig. **4.13** where $M_{x,y,z}$ represents the magnetometer readings scaled by equation **4.8**.

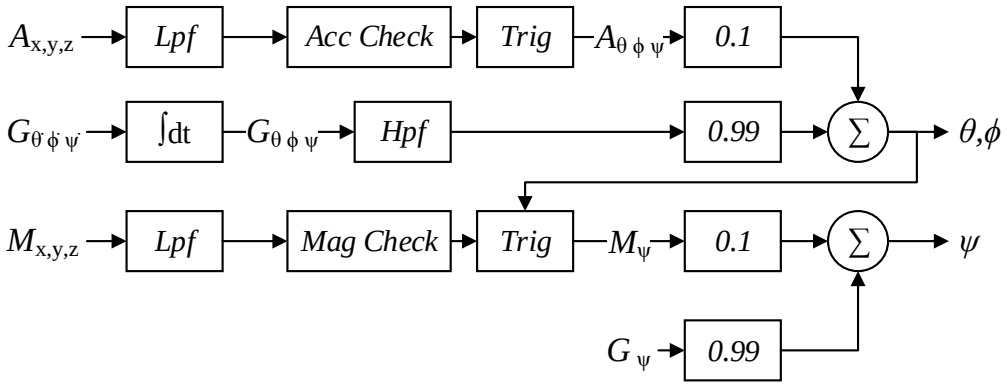

Figure 4.13: Complimentary filter with magnetometer integration

This diagram can be easily implemented in C code. Due to the filtering and trigonometry operations, it is highly recommended that this filter be used on a micro-controller with a hardware floating point unit. Pseudo C code is shown in Fig. **4.14** of this purposed filter.

4.6 Orientation Estimation Conclusion

The proposed IMU fusion filter is a computationally efficient and simple filter that provides complete orientation assessment of a quadcopter. The filter was validated using real world test data on measured rotary bed. The results of the testing are shown in Fig. **4.15** where

```
#include <math.h>
#define DeltaT 0.002 // Filter is run every 2ms.
void IMU_Comp_Filter(){
  float Accel_Mag, Pitch_Accel, Roll_Accel,Num,Den,Yaw_Mag; //temp vars

  Ax = Ax + 0.1*(Ax_Raw - Ax); // Acceleration Low Pass Filter
  Ay = Ay + 0.1*(Ay_Raw - Ay);
  Az = Az + 0.1*(Az_Raw - Az);

  Pitch+= Gx * DeltaT; // Apply Gyro Integral
  Roll+= Gy * DeltaT;
  Yaw+= Gz * DeltaT;

  Accel_Mag = fabsf(Ax) + fabsf(Ay) + fabsf(Az); //Should be near 1g
  if (fabsf(Accel_Mag-1)<0.2) //If not experiencing external acceleration
  {
    Pitch_Accel = (180/PI) * atan(-Ay,Az); // Apply Trig
    Roll_Accel = (180/PI) * atan2(Ax,sqrt(Ay*Ay + Az*Az));

    Pitch = 0.99*Pitch + 0.01*Pitch_Accel; //Combine Gyro & Accel Data
    Roll = 0.99*Pitch + 0.01*Roll_Accel; // Fuse gyro and accelerometer
  } // End of typical complimentary filter

  Mx = Mx + 0.1*(Mx_Raw - Mx); // Magnetometer Low Pass Filter
  My = My + 0.1*(My_Raw - My);
  Mz = Mz + 0.1*(Mz_Raw - Mz);

  Mag_Mag = fabsf(Mx) + fabsf(My) + fabsf(Mz); //Should be near 1
  if(fabsf((Mag_Mag-1)<0.2) //If not experiencing external fields
  {
    Num = Mz*sin(Roll) - My*cos(Roll);
    Den = Mx*cos(Theta)+My*sin(Pitch)*sin(Roll)+Bz*sin(Pitch)*cos(Roll);
    Yaw_Mag = (180/PI) * atan2(num,den); // Apply Trig
    Yaw = 0.99*Yaw + 0.1*Yaw_Mag; // Fuse gyro and magnetometer
  }
}
```

Figure 4.14: Block diagram of complementary filter

$\phi_{Measured}$ is the measured roll, where ϕ_{Filter} is the output of the IMU fusion filter, and *Error* is the observed difference between the measured roll and the filter output.

As observed in Fig. **4.15**, the steady state error is negligible and the transient error is minimal. A weakness of this filter is that it relies on filter coefficients that must be tunned on a case by case basis. Another weakness of this filter is that it is using Euler angles (θ, ϕ, ψ). Euler rotation angles become undefined in edge cases such as $\theta = 90$. Consequently, this filter implementation is not designed for acrobatic maneuvers. A strength

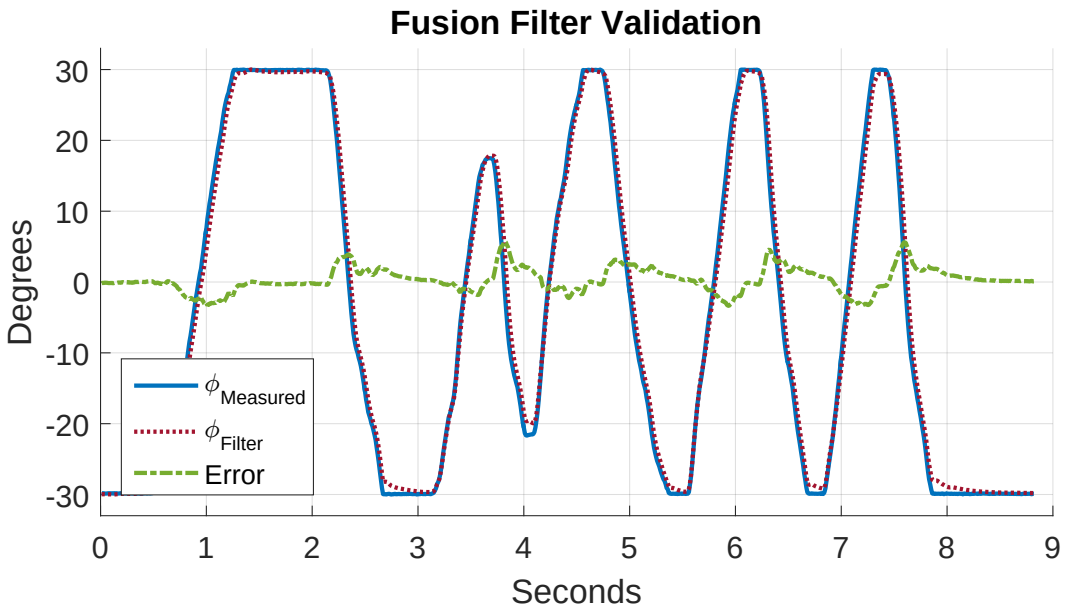

Figure 4.15: Complimentary filter validation test measuring and computing roll

of this filter is that is it is easy to understand and implement. In addition, with added data checks for valid accelerometer and magnetometer information, this filter is ideal for use on multi-rotor aerial vehicles.

CHAPTER 5

Control System Implementation

5.1 Introduction

This chapter will overview the control system used to achieve stable flight and meet the control objectives listed in **3.1**. This control system was needed in order to handle real world disturbances and to account for unknown offsets. In order to drive the quadcopter's orientation(θ, ϕ, ψ) to desired values, a series of proportional integral derivative (PID) controllers were implemented.

5.2 PID Basics

A PID controller is a control loop that updates based upon the error observed between a desired output and the measured output. This control loop's response is characterized by coefficients K_p, K_i, K_d and is shown in equation **5.1** where e represents error and $u(t)$ represents the PID output[30].

$$u(t) = K_p \cdot e(t) + K_i \cdot \int_0^t e(\tau)d\tau + K_d \frac{de(t)}{dt} \tag{5.1}$$

The magnitude of coefficients K_p, K_i, K_d determines how responsive the controller is to proportional, integral, and derivative errors respectively. Control loops such as PID act on

systems to stabilize them if needed. In addition, a PID loop can improve transient response of a system. Systems themselves in controls context are often referred to as a "plant". In the case of this thesis, the plant is the quadcopter system. This plant along with control is visualized in Fig. **5.1** where $u(t)$ is the input to the plant, where $r(t)$ is the desired set point of the plant, and where $e(t)$ is the error between the output of the plant and the desired set point.

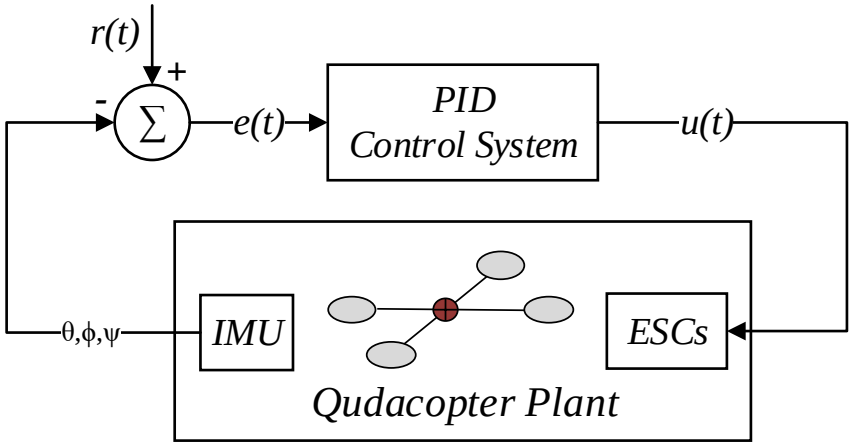

Figure 5.1: Diagram of quadcopter plant and control system

The input to the plant, $u(t)$, represents the speed commanded to each of the quadcopter's motors. For simplicity, $u(t)$ will be redefined to vector T where $T = [T_0, T_1, T_2, T_3]$. T_0, T_1, T_2, T_3 represent the four individual motor thrust vectors. $r(t)$, the desired quadcopter outputs, is the user commanded orientation angles θ_c, ϕ_c, ψ_c as well as throttle T_c. Recall that these outputs were previously defined in equation **3.1**. Note that this system is linearized at a current point in time and consequently assumes that superposition is upheld. Consequently, the input to our system u(t) is calculated as a summation of the individual control components. This control concept is shown in Fig. **5.2** and the calculations for each block are demonstrated in section 5.3.

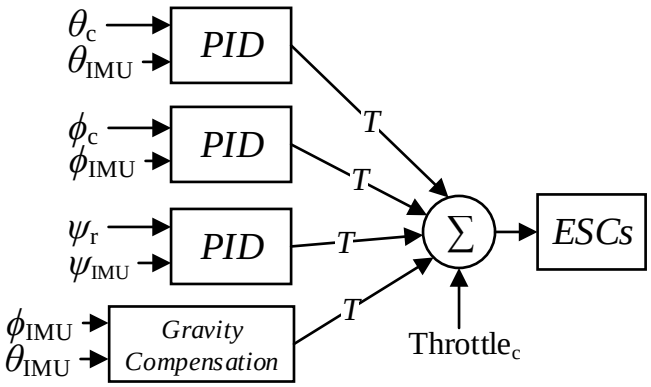

Figure 5.2: Expanded view of quadcopter's control system

With the input and output relationship established, the following section overviews the PID code developed for the system as well as how T was updated such that the control goals are achieved.

5.3 PID Software Implementation

The first step in implementing the control shown Fig. **5.2** was to write a simple PID controller in software as shown in Fig. **5.4**.

```
1  #define I_THR 200 // Max threshold value for integral
2  #define DeltaT 0.01 // Filter is run every 10ms.
3  float PID_Output(float Input, float Target, PID_STRUCT * PID){
4    float Error = Target-Input; // Calcualte Setpoint Error
5    float P = (PID->KP) * Error; // Proportional
6    float I = (PID->KI) * Error * DeltaT + PID->Integral_Error; // Integral
7    float D = (PID->KD) * (Error- PID->Prev_Error) * DeltaT;//Derivative
8    PID->Prev_Error = Error; //For next derivative term
9    PID->Integral_Error += (PID->KI) * Error * DeltaT; //For next I term
10   if(fabsf( I ) > I_THR){ // Integral windup prevention
11     PID->Integral_Error = (PID->Integral_Error>0) ? I_THR : -I_THR;
12     I = (PID->Prev_Error>0) ? I_THR : -I_THR; // Limit I to +- I_THR
13   }
14   return (P+I+D); // Return PID result
15 }
```

Figure 5.3: Code snippet of PID Controller

This code provides a PID output per a given input, target, and PID parameter structure.

This PID block can then be used to act on pitch, roll, and yaw.

```
void  Get_Control_Errors(){
  cntrlRoll = PID_Output(IMU_Roll, Remote_Roll, &Roll_PID);
  cntrlPitch = PID_Output(IMU_Pitch, Remote_Pitch, &Pitch_PID);
  cntrlYaw = PID_Output(IMU_Yaw, Remote_Yaw, &Yaw_PID);
}
```

Figure 5.4: Code snippet for calculating PID results

With these control outputs, we can now finally use the model developed in equation **3.10** which relates how θ, ψ, ϕ relate to motor speeds T. This model determines how we update the motor speeds T respectively. To illustrate this, Fig. **5.5** shows how equation **3.10** was applied in code to update T based on a given control error. Note, apart from simulation, a motivation for this derivation is such pitch and roll perform similarly. Consequently, constants A, B are formed for pitch and roll respectively. For normalization, pitch and roll were divided by A such that their response would be roughly equal. Yaw rate is due to different inertia physics and thus was not scaled by A.

```
#define A (H * DeltaT / (2*IXX)) // Constant acting on pitch
#define B (L * DeltaT / (2*IYY)) // Constant acting on roll
void Apply_Pitch(){
  T[0] += cntrlPitch;
  T[1] += cntrlPitch;
  T[2] -= cntrlPitch;
  T[3] -= cntrlPitch;
}

void Apply_Roll(){
  T[0] += (B/A) * cntrlRoll;
  T[1] -= (B/A) * cntrlRoll;
  T[2] -= (B/A) * cntrlRoll;
  T[3] += (B/A) * cntrlRoll;
}

void Apply_Yaw(){
  T[0] +=cntrlYaw;
  T[1] -=cntrlYaw;
  T[2] +=cntrlYaw;
  T[3] -=cntrlYaw;
}
```

Figure 5.5: Code snippet of pitch, roll, and yaw thrust calculations

The final control variable is height(z) which is controlled by the user. Consequently, as far as the controller is concerned, this is open loop control. However, to simplify user control, aspects of equation **3.10** can still be taken into account. Specifically when the quadcopter has a none zero roll or pitch, more collective thrust is needed in order to ensure the quadcopter maintains its height. The code designed to achieve this throttle control is demonstrated in Fig. **5.6**.

```
#include <math.h>

void Apply_Gravity_Compensation(){// additional thrust if titling
  float MG_Factor = (MASS * GRAVITY / 4) * cos(IMU_Pitch) * cos(IMU_Roll);
  T[0] +=MG_Factor;
  T[1] +=MG_Factor;
  T[2] +=MG_Factor;
  T[3] +=MG_Factor;
}

void Apply_Throttle(){ // Take joystick value of throttle and apply it to
    all motors
  T[0] +=Remote_Throttle;
  T[1] +=Remote_Throttle;
  T[2] +=Remote_Throttle;
  T[3] +=Remote_Throttle;
}

#define MOTOR_SPEED_MAX 1000.0 // Max speed normalized to 1000.
#define MOTOR_SPEED_MIN 100.0

void Apply_Throttle_Limits(){ // Ensure motor values are not beyond their
    min/max values
  uint16_t i = 0;
  for(i=0; i<4; i++)
  {
    if(T[i]>(MOTOR_SPEED_MAX))
      T[i] = MOTOR_SPEED_MAX;

    if(T[i]<(MOTOR_SPEED_MIN))
      T[i] = MOTOR_SPEED_MIN;
  }
}
```

Figure 5.6: Code snippet of open loop throttle control

With the implementation of the PID system and update laws, these segments of code can be combined to formulate the overall control system. Note to achieve a stable quadcopter, it is recommended to update motor speeds atleast at a rate of 100 Hz. This control loop code is

illustrated in Fig. 5.7.

```
1
2  void Run_Control_Loop()
3  {
4    Get_Control_Errors();
5    Apply_Throttle();
6    Apply_Gravity_Compensation();
7    Apply_Pitch();
8    Apply_Roll();
9    Apply_Yaw();
10   Apply_Throttle_Limits();
11 }
```

Figure 5.7: Code snippet of control loop

5.4 GUI and PID Tuning

Optimal selection of PID coefficients is a common problem when designing a PID control system. Given one has an accurate physical model, the optimal PID coefficients can be selected based upon desired overshoot and speed for example. However, without a physical model, values can be tunned on the fly. Initially, quadcopter parameters to achieve flight were tunned on the fly. A javascript GUI was written to help for debug purposes. This GUI had the capacity to tune the PID parameters of the quadcopter on the fly. A snapshot of this GUI is shown in Fig. 5.8.

This GUI was useful for collecting and saving live flight data, testing motor orientation, and adjusting PID values. Being able to update and visualize data on the fly greatly simplified PID tuning and general development.

Figure 5.8: Quadcopter javascript GUI

5.5 Software Architecture

The control loop in Fig. **5.7** along with the IMU code purposed in Fig. **4.14** account for the majority of flight critical code running on the quadcopter. An overall software architecture is shown in Fig. **5.9**.

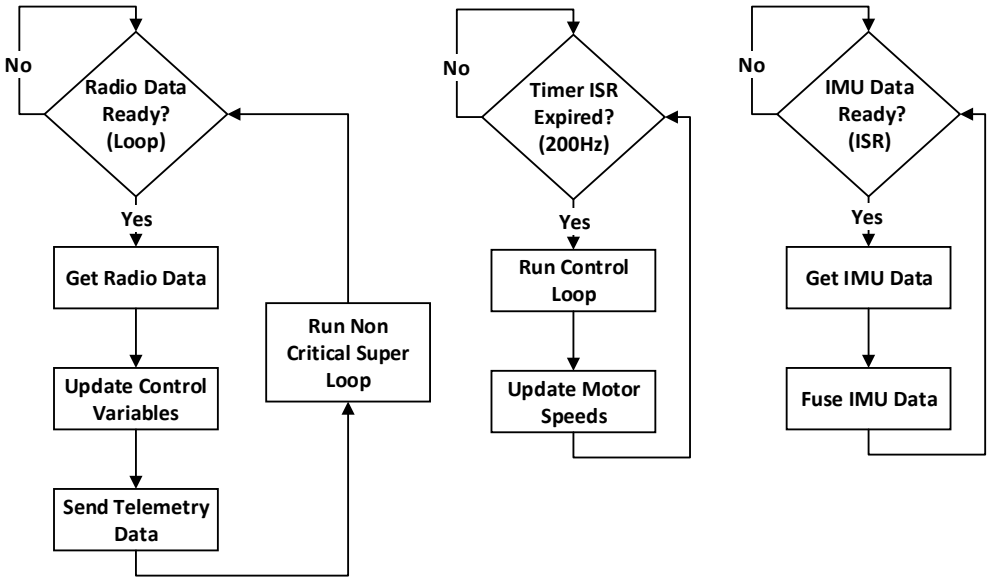

Figure 5.9: High level quadcopter software flow chart

To keep control timing and IMU collection constant, the software was implemented in three separate threads. These threads primarily managed IMU filter updates, control system updates, and radio link updates. For this quadcopter software implementation, IMU data is received on a consistent interrupt basis. Gyro and accelerometer readings are updated and filtered every 500 Hz. The magnetometer is updated every 100 Hz which is the maximum for the given device. These updates are performed based on an interrupt to give the IMU filter consisting timing characteristics. Likewise, the control system is also triggered through interrupts. The control system executes every 200 Hz and uses the most up to date data from both the controller and the IMU filter to perform its calculations. Less timing critical tasks are then executed in a super loop such as checking for new radio data, transmitting telemetry data, handling USB commands, and other non flight related features. Full source code is provided at www.somegithubrepo.com.

CHAPTER 6

Radio Frequency System Implementation

6.1 Introduction

This chapter will overview the radio frequency (RF) system used with the Marquette Drone and explain concepts regarding its design. Radio frequency design at ultra high frequency (UHF) is tedious which is why a chapter is devoted to it. This chapter will overview a minimal amount of information required to design a legal and efficient RF link. The RF hardware designed for the Marquette drone is shown in Fig. **6.1**.

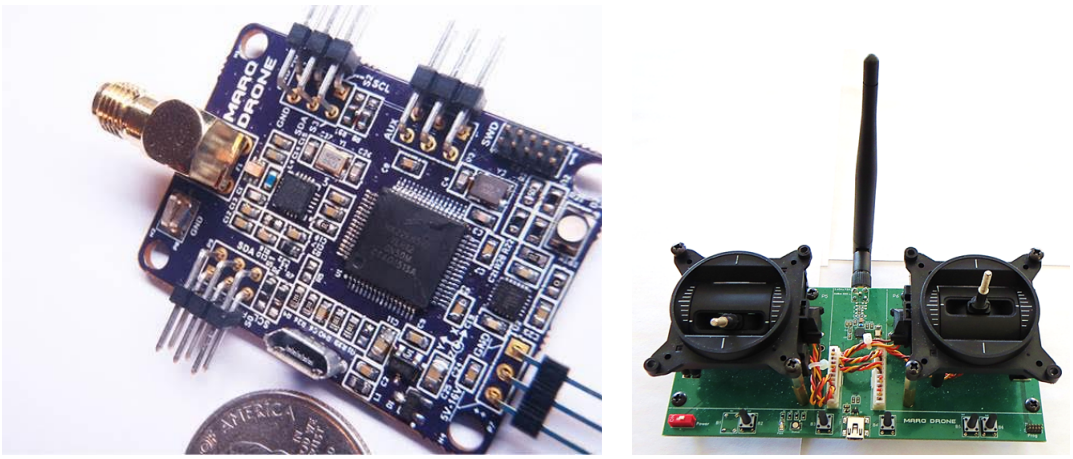

(a) (b)

Figure 6.1: RF Marquette Drone hardware: (a) Flight Controller, (b) Radio Controller

The Marquette Drone utilizes a flight controller with an integrated radio as well as a remote controller with an integrated radio. The primary motivation behind this was eliminate use of the PPM protocol as well as have the capacity to collect data in real time. This hardware

was designed to help understand the nature of the underlying system as well to be able to implement a more flexible architecture as shown previous in Fig. **2.5**. The schematics of these pieces are included in Appendix A. The CC2500 transceiver was selected for this RF system and its selection is explained in latter sections. A RF block diagram of this system is presented in Fig. **6.2**.

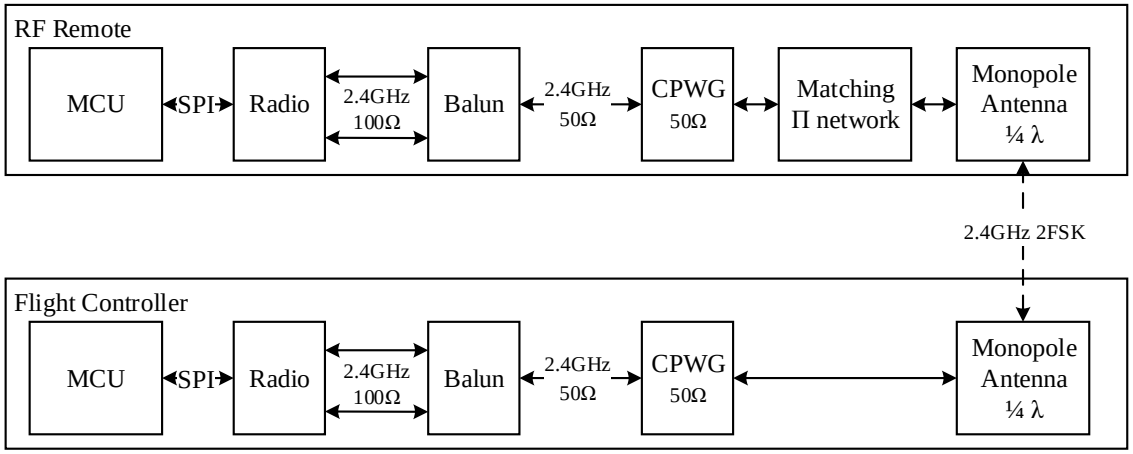

Figure 6.2: Block diagram of Marquette Drone RF system

These RF blocks will be over-viewed in the following sections. Before over-viewing these blocks, basic design considerations are addressed such as frequency of operation and range calculations.

6.2 Selecting a Frequency Band

Frequency of operation is the principle attribute of any RF system. The frequency determines the size of the radio system, the required power of the RF system, and the legality of a system. Firstly, one must select a radio frequency that is legal to operate in their region. For many countries, there exists Industrial, Scientific, and Medical (ISM) bands of operation where RF transmission does not require a license. For the United States, ISM

operation is covered in FCC Title 47 Part 15[31] and is shown in Table 6.1.

Fundamental frequency (MHz):	**Field strength of fundamental (mV/m)**	**Field strength of harmonics (mV/m)**
902-928	500	1.6
2435-2465	500	1.6
5785-5815	500	1.6
10500-10550	2500	25.0
24075-24175	2500	25.0

Table 6.1: Title 47 part 15.245 ISM Bands

The 2.4 GHz band is widely accepted in most countries and has become popular for consumer electronics. Consequently, many affordable RF devices now exist for this band of operation. An advantage of this band is the size of its quarter wavelength. The calculations for the 2.4GHz quater wavelength are shown in equation **B.2** where λ is wavelength, where c is the speed of light, and where f_o is the frequency of operation.

$$\begin{aligned} &\frac{\lambda}{4} = \frac{c}{4 \cdot f_o} \\ &\frac{2.99 \cdot 10^8 m/s}{4 \cdot 2.4GHz} \approx 3.12cm \approx 1.23inches \end{aligned} \tag{6.1}$$

Having a quarter wavelength of roughly 1.23 inches allows for the antenna to be easily mounted to both the drone and the remote controller. While smaller antennas could be used for lower frequency bands, these antennas would be fundamentally limited in their efficiency.

6.3 Creating a link budget with Friis transmission

Another crucial aspect of an RF system is designing for a desired transmission range. Traditionally this is done by creating a link budget. To create a link budget, the power output of the transmitter must be known, the antenna gain of both the transmitter and

receiver must be known, and the receiver sensitivity must be known. With these inputs and assuming Friis transmission, the Friis transmission equation can be used to calculate range[32]. For the Marquette drone system, quarter wavelength monopoles were used for the transmitter and receiver that have an ideal antenna gain of 5.19 dBi. In regards to the transiever, the CC2500 was selected which has a max transmission power of 1dBm and a receiver sensitivity of -83 dBm at 500kBaud. The standard representation of the Friis transmission equation as shown in equation **6.2** where P_{rx} is the receiver sensitivity in watts, where P_{tx} is the transmitter power in watts, where r is the distance in meters, and where G_{tx}, G_{rx} are the isotropic gains of the transmitter and receiver antennas.

$$P_{rx} = P_{tx} \cdot G_{tx} \cdot G_{rx} \left(\frac{c}{4\pi \cdot r \cdot f_o} \right)^2 \tag{6.2}$$

Next, this equation is solved for range in terms of units that are commonly specified such as decibel milli-watts (dbm) and decibel isotropic (dbi).

$$r = 10E\left(\frac{P_{tx,dbm} - P_{rx,dbm} + G_{tx,dbi} + G_{rx,dbi} + 20log_{10}(\frac{c}{4 \cdot \pi \cdot f_o}) - 10}{20} \right) \approx 82m \tag{6.3}$$

Note this is a highly optimistic estimate of the expected range since it assumes perfect antenna gains and no additional losses. However, this number is a ball park range and at best, one cannot expect more than this value. Often it is assumed that the observed value will be 10 times less than an ideal measurement which would leave the range to be slightly under 100 feet which is acceptable for indoor flight.

6.4 2.4GHz Microstrip and Coplanar Wave Guide Transmission Line

Transmission lines are required for high frequency signals where parasitic inductance and capacitance begin to effect the characteristics of the signal transmitted. 2.4 GHz is a high enough frequency where these parasitic effects will have adverse influence over signals transmitted. For optimum power transmission, the source impedance must match the load impedance and the transmission line impedance. In general, both sources and antennas are matched to 50Ω impedance. This leaves the transmission line impedance which must be designed to 50Ω. Consequently, a transmission line is needed on the PCB between the source and the antenna. There are two common transmission lines that can be easily be created on a PCB and are shown in Fig. **6.3**

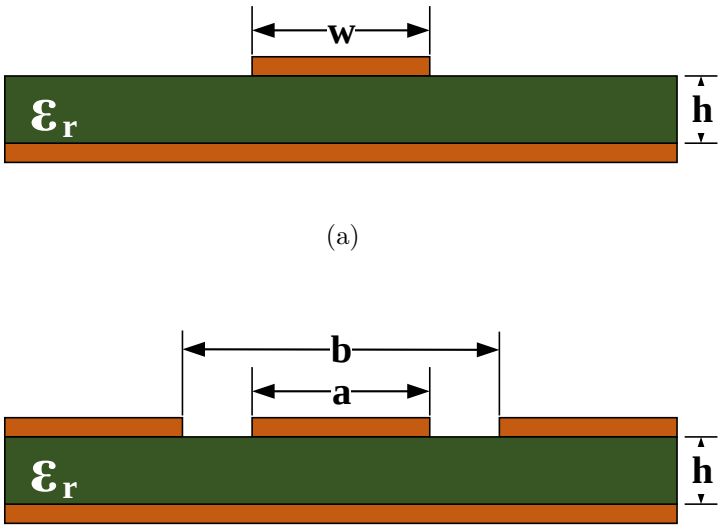

Figure 6.3: PCB transmission lines: (a) Microstrip Line, (b) Coplanar Wave Guide

Calculations for these transmission lines are lengthy and are included in Appendix B. Note it is imperative that the correct ϵ_r be used for both equations and that this parameter changes with frequency. Fig. **6.4** is a demonstration of how frequency effects the dielectric

constant of a PCB substrate. For most materials, the dielectric constant trends downwards as the frequency increases.

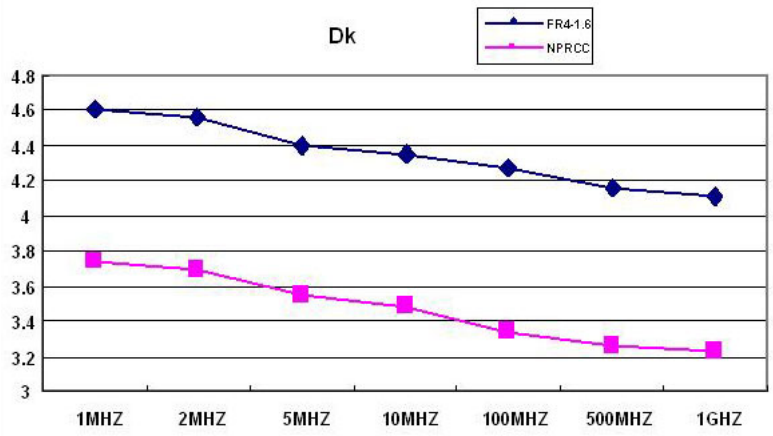

Figure 6.4: Plot of how ϵ_r changes with respect to frequency. Image source:(1)

Failing to take the material's frequency characteristics into account can result in lossy transmission lines. While the transmission line equations in Appendix B are frequency independent, the material characteristics cause a real-world frequency dependency.

With regards to transmission line selection, coplanar wage guides are often preferred since they result in smaller transmission lines. In addition, coplanar waveguides are more ideal for adding shunt tunning elements. Parallel and series element tuning networks can be used to match a load impedance(antenna) to the transmission and the source impedance. Tunning strategies are beyond the scope of this thesis but are over-viewed at the following reference[33]. An example matching network is shown in Fig. **6.5**.

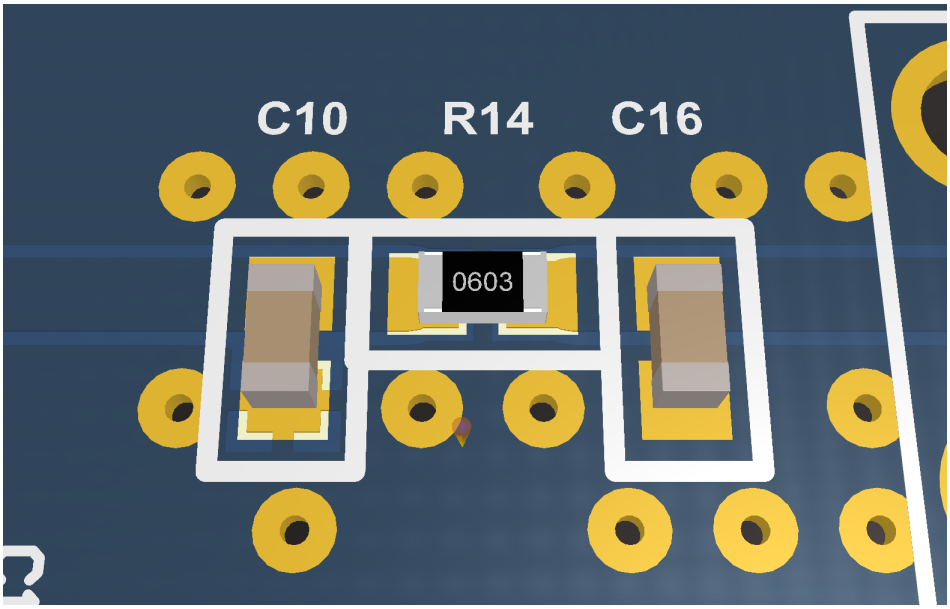

Figure 6.5: PI tuning network example

In this network, shunt and series elements can be changed to capacitors or inductors as needed. This network should be located close to the load that is intended to be matched. Vias were added around the network to reduce ground loop impedance. Without vias, small value capacitors can act as inductors. These vias are left un-tented to allow for connection RF pigtails. RF pigtails are used to validate the impedance of the network with a vector network analyzer. Note, if RF performance is satisfactory, the network can be left unpopulated except for a zero ohm resistor on the series element.

6.5 RF Baluns

RF sources and loads often exist in differential and single ended forms. The CC2500 transceiver has a differential RF output which was intended for differential loads such as loop antennas or dipole antennas. However, differential antennas are a mechanical inconvenience so it is often desired to use single ended loads such as a monopole antenna or a helical antenna. Consequently, baluns are used to convert from differential signals to a single ended

signal and vice versa. PCB mounted baluns can be made of passive discrete electrical components such as inductors and capacitors[34]. However, the validation and the tunning of these baluns is difficult without access to a high frequency oscilloscope. An alternative is to use an integrated balun that requires minimal additional discrete components. Examples of both an integrated balun and discrete balun are illustrated in Fig. **6.6**.

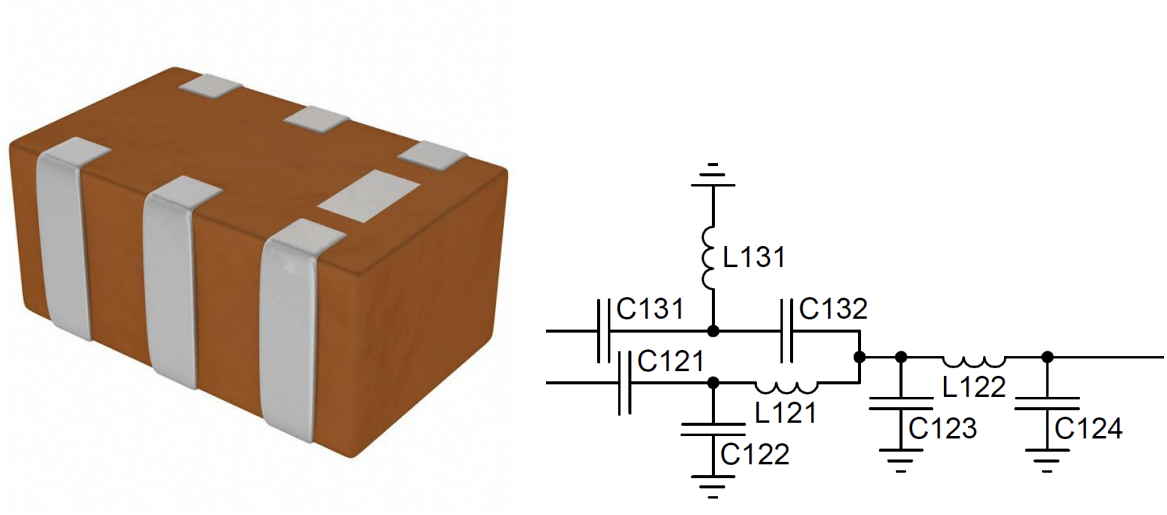

(a) (b)

Figure 6.6: RF Baluns: (a) Integrated Balun, (b) Discrete Balun. Image Sources: (a)(b)

For this thesis, an integrated balun was used to save space and reduce design complexity[35].

6.6 RF Packet Structure and Collision Avoidance

Once the hardware design of the system was completed, a system of sending RF packets was contrived. This is method is only an example and is by no means optimal. RF packet structures vary for application as to whether throughput or range is prioritized. The RF packet structure used in this thesis is shown in Fig. **6.7**.

This packet contains four major components which are a preamble, sync, data, and checksum. The preamble size can vary and is used to give the receiver an opportunity to

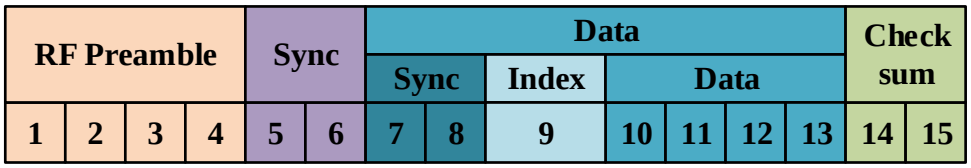

Figure 6.7: RF Packet Implementation

lock onto the signal being transmitted. Longer preambles increase the probability of the packet being received. Sync bytes inform the receiver when the preamble has ended. The data segment of the packet in this case consists of two sync bytes, an index byte, and four bytes of data. Finally a checksum is appended to the packet to help verify the validity of the data received. Note the preambles are not checksummed since it takes time for the receiver to lock onto the signal and initial corruptions is expected. RF packets are discarded should the data checksum fail. Packeting of data as opposed to a continuous stream helps save power as well as gives the opportunity for bidirectional communication between transceivers. However, a disadvantage of packeting data is overhead. In this case, 15 bytes of data are used to convey 5 bytes of information. This limits the effective baud rate at which information is transfered. Another bandwidth limitation is at what speed bytes are encoded on top of the 2.4GHz carrier frequency. For this implementation, two frequency shift keying (2-FSK) modulation was used. Bytes were encoded at 250K baud which meant that at best, information would be conveyed at 250K speed in addition to packet overhead. A Lower baud would increase probability of reception meanwhile a higher baud would allow for faster transmission. 250K was a selected as a compromise between these two goals. Then, to achieve bi-directional communication, a ping system was used in which the remote would periodically send out control packets and the flight controller would send back telemetry information when it received a packet. Naturally, the period of this exchange must be longer

than the time required to transmit 2 packets. A packet exchange is shown in Fig. **6.8** by probing the voltage of the voltage at the balun.

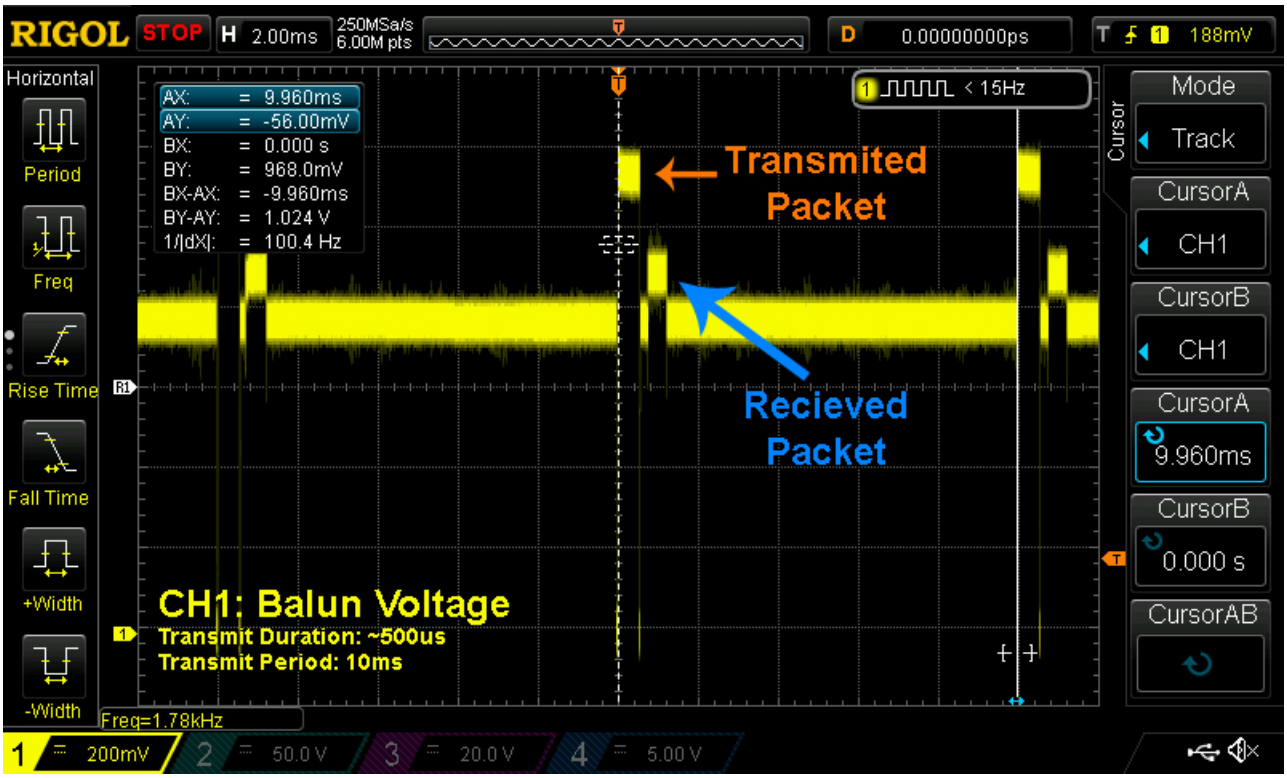

Figure 6.8: RF Packet Implementation

The balun has an integrated bandpass filter which simplifies observation of transmitted and received packets. While the presents of packets can be observed by a RMS magnitude, the individual byte information is not possible to obtain without a GHz class oscilloscope. Having the remote transmit periodically and the flight controller echoing back helps prevent any chance of packet collision. An initial design where both the controller and flight controller periodically transmitted independently resulted in phases of signal lost. During the phases of signal loss, both the remote and controller were periodically transmitting at the same time and periodic collisions would occur.

6.7 Conclusion

Designing a custom RF system allows for great flexibility and efficent data acquisition but comes at the cost of design complexity. For a custom RF system, first a frequency band must first be selected based upon the antenna size desired and legal bands of operation. After a frequency has been selected, antennas types and a transceiver are selected given the mechanical and power constraints of the system. RF transmission lines and baluns are required in order to get a signal from point A to B without significant loss. Finally, a scheme must be formulated for the transmission of bidirectional packets. In the end, a efficient, customizable, and bidirectional link was established between the quadcopter and the remote. This is advantageous over the majority of off the shelf systems since data is not encoded into PPM signals, the data is bidirectional, and the source files are available for future expansion.

CHAPTER 7

Hardware Implementations

7.1 Introduction

This chapter will briefly overview the electronic hardware design of the quadcopter. Electronic hardware components of this system include the radio system, flight controller, and motor controllers. An early picture of the quad-copter is shown in Fig. 7.1.

These pieces of hardware were designed to help understand the nature of the underlying

system as well to be able to implement a more flexible architecture as shown previous in Fig. **2.5**. Hardware involved in this project was designed in atrium and schematics/PCBs can be viewed fully in Appendix A. The following sections overview the hardware design for the quadcopter.

7.2 Flight Controller Hardware

The flight controller consists of a MCU, a IMU, a radiocore, and external IO. The flight controller is responsible for stabilizing the quad-copter and executing user control. To simplify the software, a microprocessor was needed with sufficient computational power for numerous floating point instructions. The Cortex M4 MK22FN512 by Freescale was chosen for its FPU, large flash space, large ram space, USB interface, low per unit cost, and hardware simplicity. With regards to the IMU, the MPU-9250 by Invensense was selected due to it being a compact integrated solution with a 3 axis accelerometer, gyro, and magnetometer. Another advantage of the MPU-9250 is that it had already been flight tested in another multi-rotor platform[11]. For the radiocore, the CC2500 by Texas instruments was selected due to its low cost and high reconfigurability. For motor control, four hardware PWM pins were exposed on external headers for PPM communication with ESCs. Finally, serial IO and analog IO were exposed on an additional external header for additional expansion. This architecture is illustrated in block diagram form in Fig. **7.1**.

The board itself was assembled using solder paste and a toaster reflow oven. The primary hardware challenges involved in flight controller operation was the development of the radio core. The micro-controller as well as the IMU are much lower frequency devices with more implementation robustness. Clean power sourcing, decoupling, ESD protection, transient

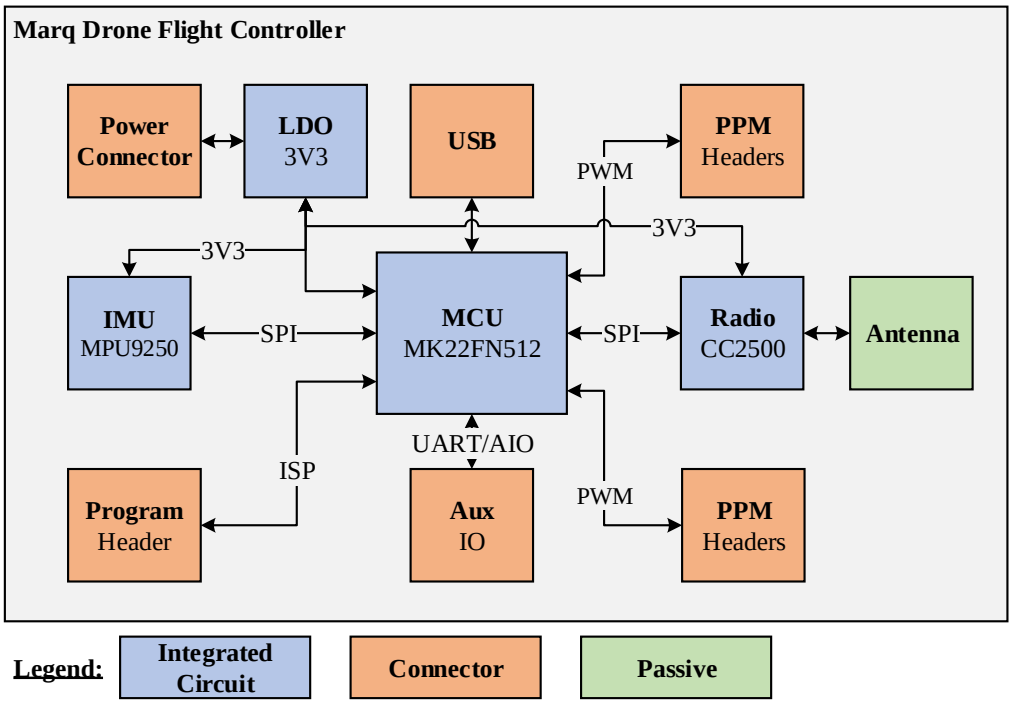

Figure 7.1: Block diagram of flight controller

protection and other basic hardware principles were implemented in its design. The assembled design is shown in Fig. **7.2**

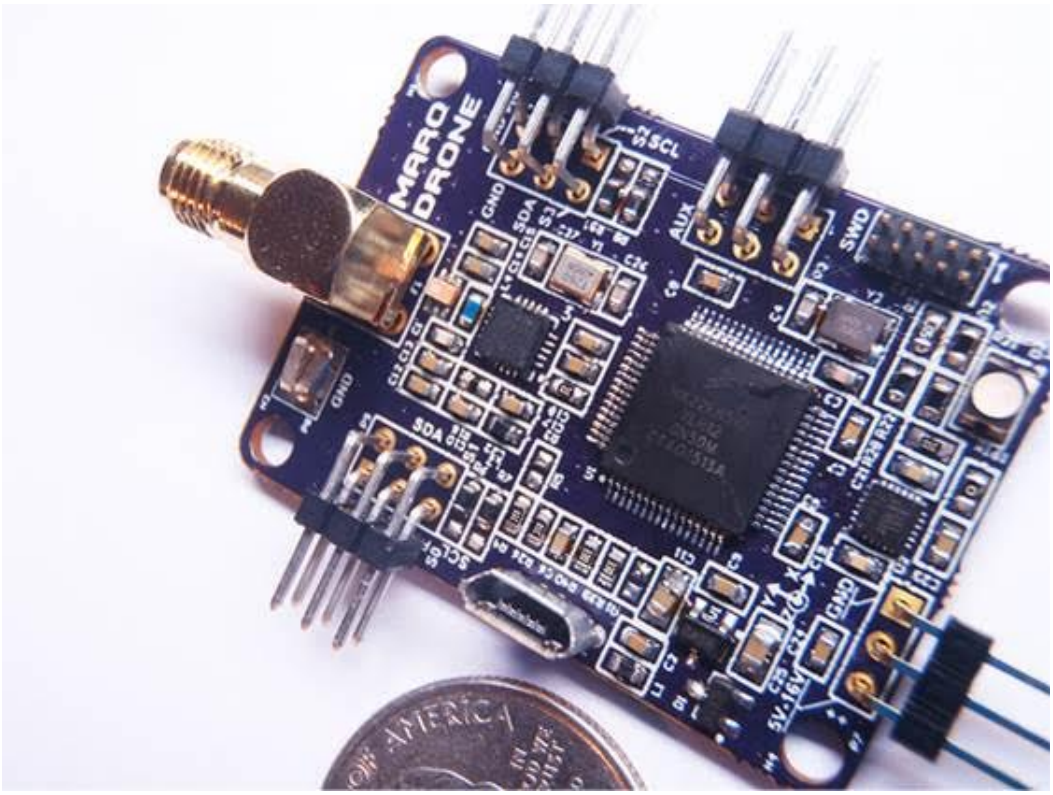

Figure 7.2: Image of Marq Drone flight controller

7.3 Remote Controller

The remote controller hardware consists of two joysticks, a micro-controller with a USB interface, a radiocore, push buttons, and a rechargeable battery. A system level block diagram for the remote is shown in Fig. **7.3**. This diagram illustrates all the major hardware blocks utilized by the controller. Further information can derived from the source code as well as the schematic.

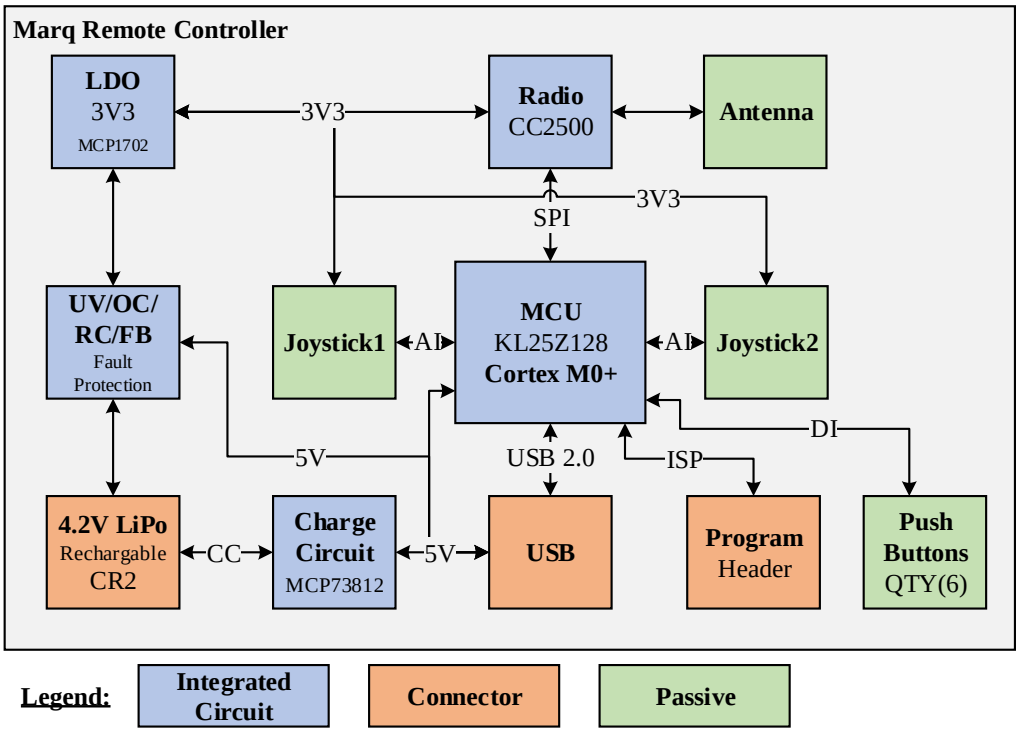

Figure 7.3: Block Diagram of flight controller

For the joysticks, two Frsky Taranis Gimbals were selected. These joysticks were selected since they were primarily designed to for remote flight control. To simplify the mechanical design, these joysticks mount directly to the PCB which avoids requiring an injection molded or 3D printed enclosure. With regards to the microcontroller, the Freescale Kinetis Cortex M0+ KL25Z128 microcontroller was selected due to its low cost, availability, and

USB interface. The radiocore is the same as the flight controller which is the CC2500 and discussed in Chapter **??**. Push buttons were added for flight commands such as emergency cutoff. Finally, for remote portability, a 1 cell 4.2V LiPo cell battery was used such that the remote could be operated independently of a computer. This cell would be recharing any time the USB interface was plugged in. In addition, the battery system had hardware protection against reverse battery, current back-feeding, over current, and under-voltage. A picture of the assembled controller is illustrated in Fig. **7.4**.

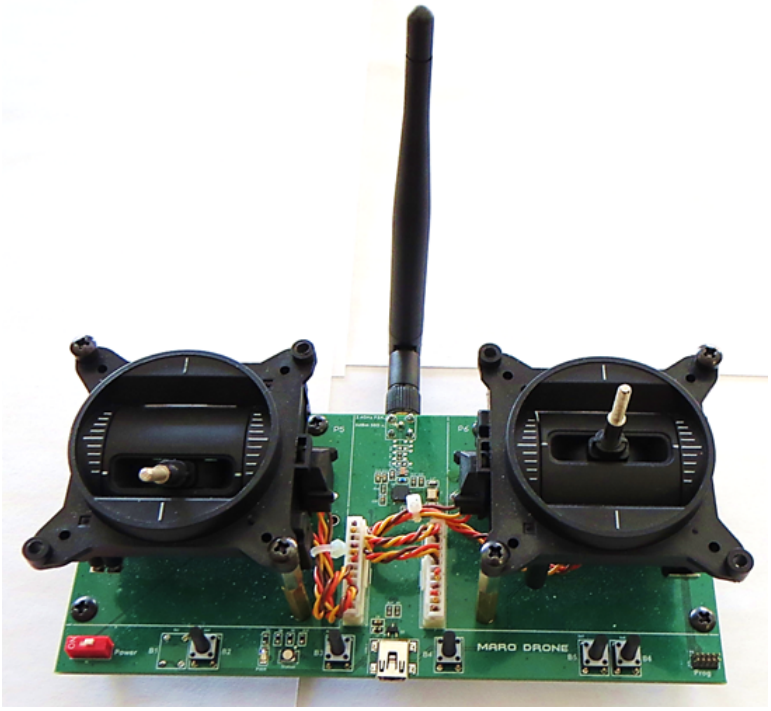

Figure 7.4: Image of Marq Drone remote

Apart from the RF design, the only other challenging aspect of the remote controller design was the LiPo battery protection system. Care must be taken such that Lipo batteries are not overcharged. Overcharging LiPos will break down their internal chemistry and potentially cause fires. Consequently, the MCP73812 charge IC was used to regulate the current being used to charge the LiPo and to cutoff charging at the batteries nominal voltage. Another danger with LiPo batteries is draining them past their minimum rated voltage. Overdraining can result in a break down of chemistry which leads to inability to

recharge and sustain charge. Finally, drawing more than the battery's rated current can cause the battery to overheat and potentially catch fire and or break down in chemistry. Note, the energy capacity contained in a small single cell LiPo battery is very minimal which significantly reduces the potential hazards the battery can generate. The circuit derived to meet this requirements is shown in Fig. **7.5**.

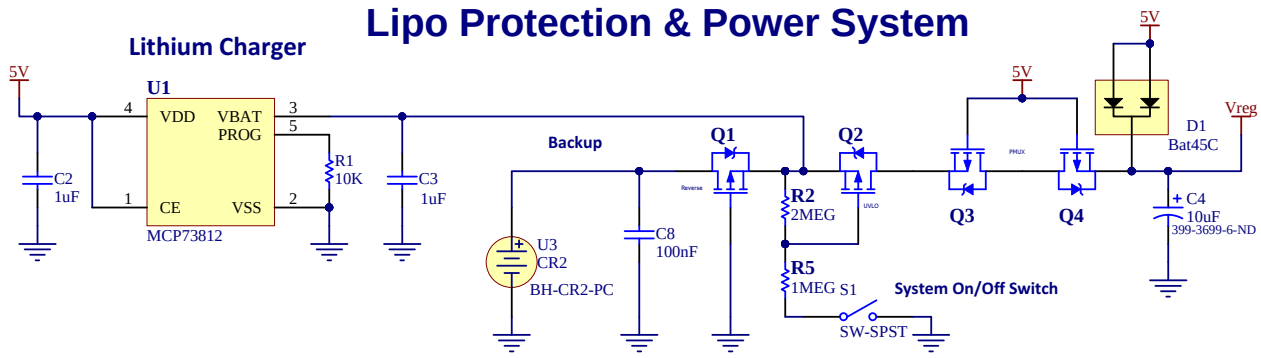

Figure 7.5: LiPo under voltage, over current, over charge, reverse bias, and backfeed protection circuit

U1 prevents overcharging of the LiPo. PFET Q1 prevents damage to U1 and other ICs in the event of reverse bias. Q2 in combination with R2 and R5 acts as an under voltage lockout as well as an over current lockout. When the LiPos battery voltage is low, the bridge divider on the gate of Q2 forces Q2 into the cutoff region of operation. Similarity, when significant current is drawn, the internal resistance of the battery combined with the R2 and R5 bridge forces Q2 into cutoff. Back to back PFETs Q3 and Q4 prevent USB power from back-feeding the battery when plugged in. FETs were used as opposed to diodes on the batteries current path to eliminate voltage drop out on the 3.3V rail.

7.4 Electronic Speed Controller Hardware

The brushless sensorless motor controllers, or ESCs, are made up primarily of a microcontroller, gate drivers, and high power FETs. The MCU selected was the Cortex

M0+ KL25Z128 Kinetis by Freescale. This was the same processor used on the remote and is pin by pin compatible with the micro-controller on the flight controller. The gate drivers selected was ADP3110 by ON Semiconductor since it supported dual high side low side NFET drivers, is 3.3V logic compliant, can be powered by 2C or 3C LiPo battery, is low cost, and has a easy to solder package. The primary switching mosfet selected was the PSMN011 by NXP since it supports a max drain current of 61A, has an RDSON of $10m\Omega$, and since it utilizes a small QFN package. A block diagram of this system is Fig. **7.6**

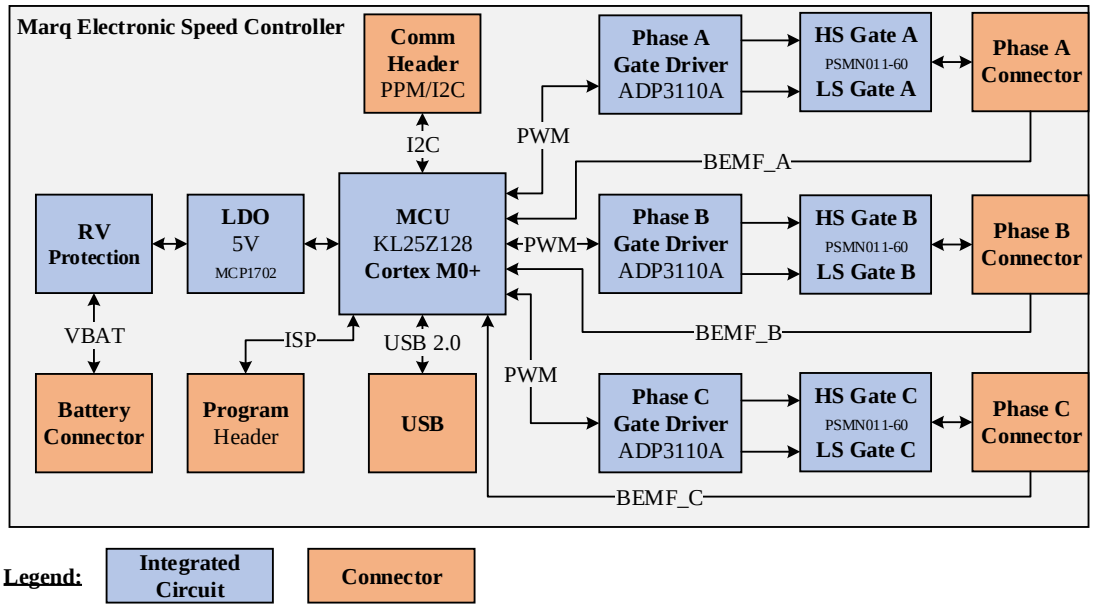

Figure 7.6: Block Diagram of Marq ESC

This ESC was designed to be compact and have capacity to drive atleast 10A of current. To achieve this, double sided population was required. Another useful aspect of this design was the USB interface for data acquisition as well as programming. This ESC was created first as a larger dev board with more debugging features such as headers for probing. Once the theory of operation was confirmed, this board was shrunk to a 0.9" by 1.6" board. Pictures of both of these boards are shown in Fig. **7.7**

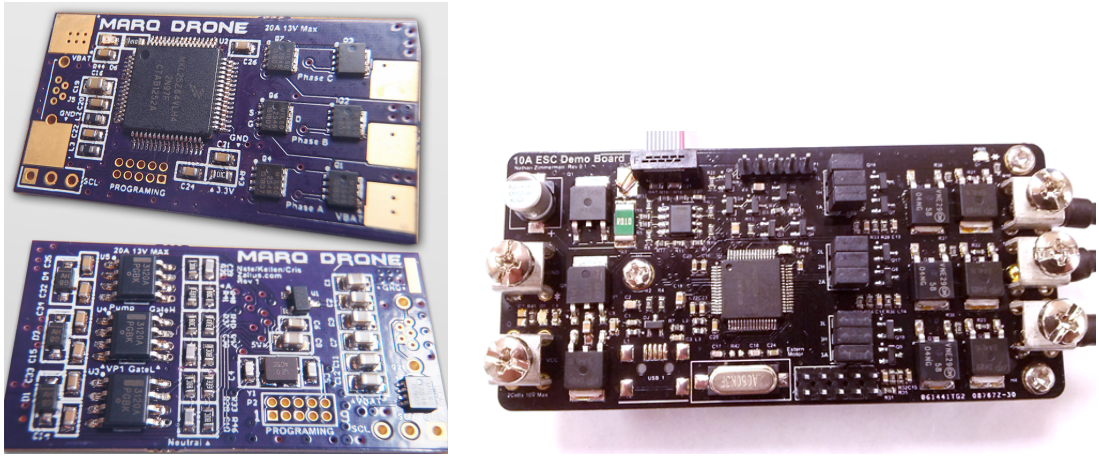

(a) (b)

Figure 7.7: Picture of ESCs: (a) Marq ESC, (b) Marq ESC Dev board

With regards to method of operation, recall these ESC are effectively a sensorless brushless motor controllers as stated in Section 2.1. This controllers uses is back EMF zero crossing detection[16]. The following section will briefly describe brushless motor basics as well as the BEMF zero cross detection driving method used in this controller.

7.4.1 Brushless motor operation

Brushless motors are synchronous 3 phase permanent magnet motors. Like a DC brushed motor, brushless motor consists of a stator which contains coils and a rotor which contains permanent magnets. If the coils are energized correctly, the coils create a rotational torque that acts on the magnets on the rotor. Since the magnets are adhered to rotor, this rotational torque causes the motor shaft to spin. However, if the coils on the stator are not energized correctly with respect to the polarity and position of the magnets, rotational torque is not generated. Consequently, knowledge of the rotors position is required in order to properly drive a DC motor. For brushed motors, a mechanical device called a brush is used such that stator coils are always properly energized with respect to the rotor. However, with a brush-less motor, this mechanical linkage from stator to the rotor is removed in order

to reduce friction and extend motor lifetime. Without the mechanical linkage between the rotor and the stator, external sensing methods of the rotor are required. Hall effect sensor can be used in order to detect the rotors position. However, hall effect sensors are expensive and require additional wires as well as mechanical protection. Another method of driving brushless motors is with sensor-less techniques such as BEMF zero cross detection.

7.4.2 Introduction to BEMF Zero Cross Driving

BEMF zero cross detection driving is a brushless 3 phase motor driving method that relies on estimating the rotors position by using voltage generated by the motors velocity. Naturally, brushless motors generate voltage when rotating similar to how a generator produces power. This voltage generated by the brushless motor is called back electro-motive force or back voltage. During operation, it is possible to view the BEMF signal of a DC 3 phase brushless DC motor on a disconnected phase. Within the BEMF wavefrom, there is an event called the "zero crossing". This event is used to determine the rotor's position in order to drive the motor correctly. The following section will introduce basic driving concepts as well as how to observe and utilize zero crossing events.

7.4.3 Brush-less Motor Driving Hardware

Brushless motors are 3 phase loads. To drive current in any direction through these three phases, three H-bridge switches are used. Consequently, there is a total of six switches and only two switches are turned on at a given time. This leaves one phase disconnected and this phase's voltage is representational of the BEMF of the motor. This concept is illustrated in Fig. 7.8 where the phase A high side switch is on, where the phase C low side switch is on,

and where phase B voltage is the BEMF signature.

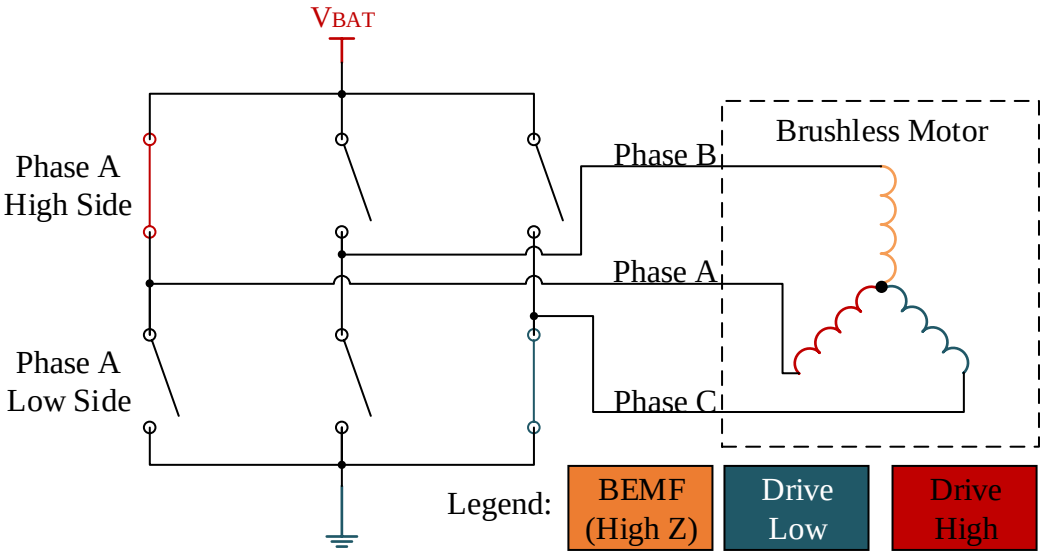

Figure 7.8: Diagram of brushless motor and 6 driving switches

These 6 switches must be actuated in a specific sequence in order for the motor to spin. This sequence is often called the "6 step trapezoidal commutation sequence". This sequence is illustrated in Fig. **7.9**. If actuated correctly, sequence creates a rotational torque on the

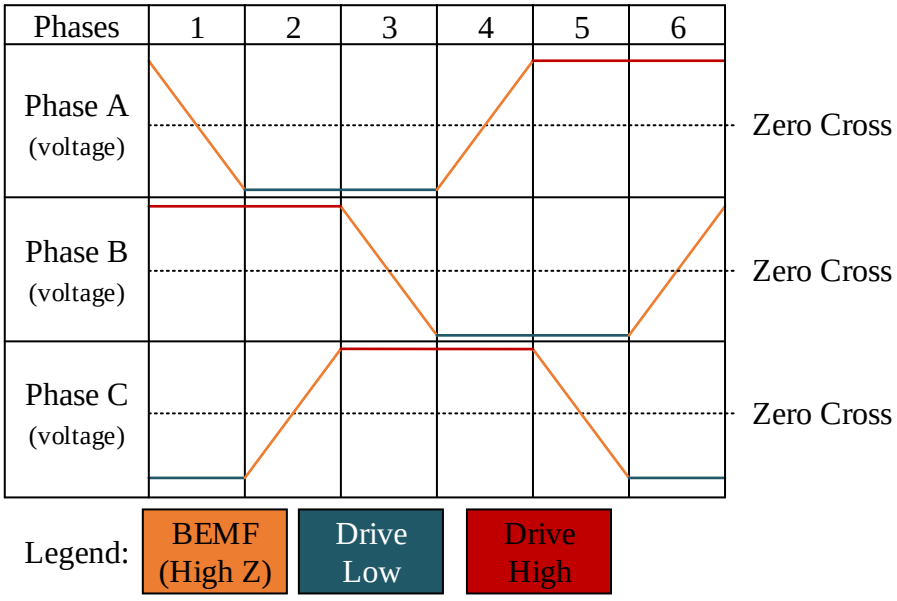

Figure 7.9: 6 step trapezoidal commutation sequence

rotor of the motor. Note that in this sequence, one phase is always producing BEMF. The

BEMF phase is used in order to determine the position of the rotor such that power can be applied productively. The position of the rotor can be determined by detecting zero crossing events. A zero crossing is where the BEMF crosses over the neutral voltage of the motor. This zero crossing event represents a rotor mid point between a commutation step. To utilize this zero crossing event, an assumption can be made that the rotor is not rapidly accelerating within a commutation step. This assumption is fair for brush-less quad-copter since the torque load is nearly constant. With this assumption, one can assume that the time it takes for the mid point to be observed will also be the approximate time it takes for the rotor to reach the next commutation phase. A basic software flowchat demonstrating this concept is shown in Fig. **7.10**.

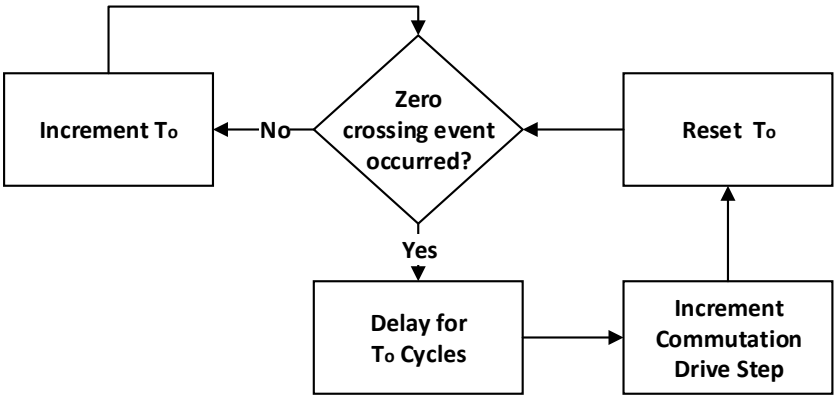

Figure 7.10: Software block diagram of zero cross brushless motor driving

While this driving scheme is simple, complexity arises in detecting the zero cross event. The zero crossing event can be determined by using a hardware comparator that compares the motor neutral voltage with the BEMF waveform. However, most brushless motors for multi-rotors do not expose neutral signal line of the motor. Consequently, this neutral voltage must be approximated by summing the three phase voltages. This is further complicated by significant BEMF noise generated by PWM switching. The diagram shown

in Fig. **7.9** illustrates 100% duty cycle which is not a common mode of operation. It follows that to vary the speed of the motor, the duration of on time is reduced with PWM. These switching signals create voltage transients that couple onto the BEMF phase. A brushless motor phase voltage is shown in Fig. **7.11** along with the hardware comparator readings.

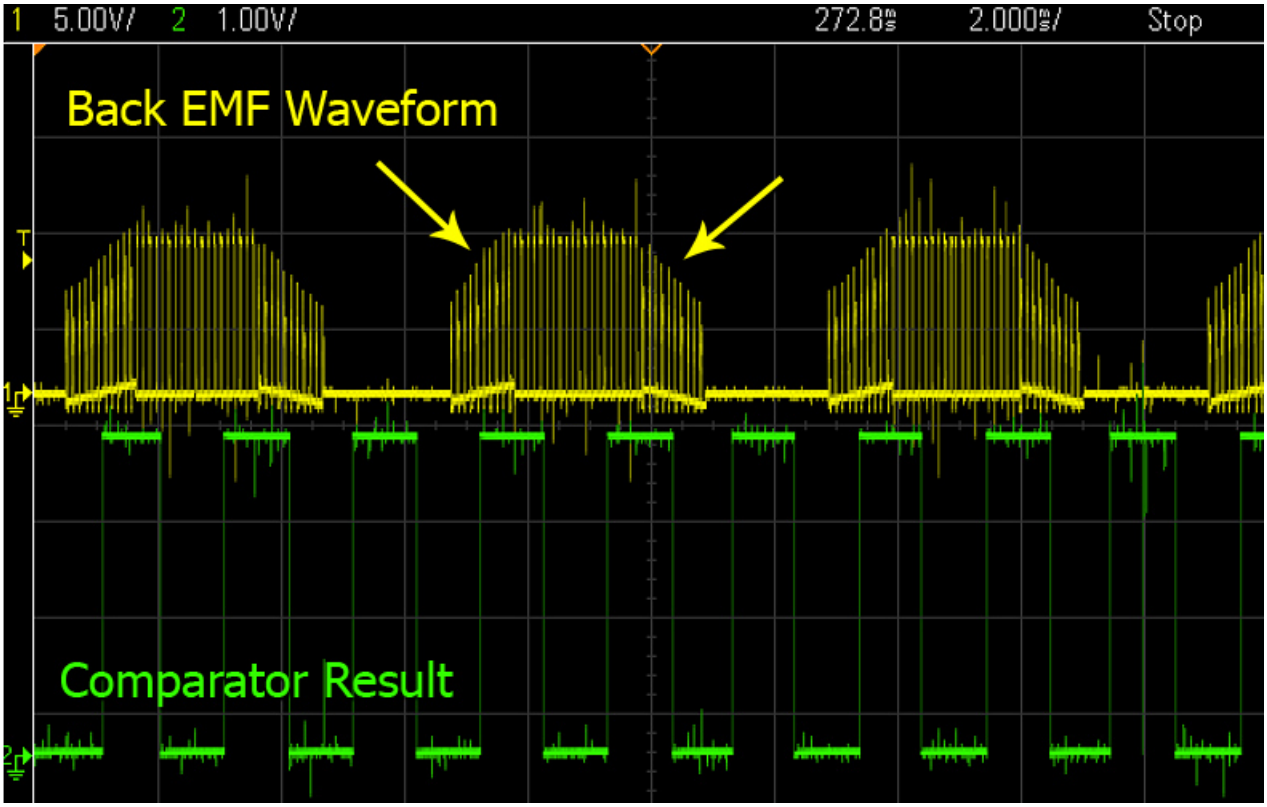

Figure 7.11: Brushless motor phase voltage(yellow) and zero cross detection comparator(green)

To achieve these results, hardware filtering was implemented on the MCU where comparator samples were windowed and transitions were generated only after a certain amount of consecutive agreeing samples were observed. This filtering along with the software method proposed in Fig. **7.10** allowed for effective brushless motor operation.

7.4.4 ESC Conclusion

Brushless motors are efficient motors that can be driven through various sensorless techniques such as zero cross detection. Section 7.4.3 overviews both the hardware and software required to implement BEMF zero-cross driving of brushless motors. While sensorless driving was achieved, there was not enough time to incorporate the drivers shown in Fig. **7.7** into the final quadcopter.

CHAPTER 8

ICL and Lidar Integration

8.1 Introduction

This chapter will overview a strategy to meet the secondary control objective proposed in equation **3.2** which is the elimination of positional drift. Positional drift is one obstacle of many that must be overcome in order to achieve autonomous indoor flight of quad-copters. Unlike land based robots, there is no significant static frictional force to keep a quadcopter in place when hovering. Consequently, there are a variety of factors that can cause positional drift in a quadcopter. One source of drift results from equation **3.4** being an approximation. Frame imperfections and air turbulence results in a summed force vector that isn't purely vertical. Another source of drift can be from external forces such as air flow in a room. A final source of drift can occur from imperfections in the control system or imperfections in the orientation estimation. As a result of these sources, positional drift is a common problem for quadcopters. The sensors in over-viewed in Chapter **??** are incapable of measuring positional drift directly. Consequently, to directly sense positional drift, more sensors are needed. For out door flight, GPS in combination with IMU and barameter sensors have been used to reduce positional drift with an extended kalman filter[36]. However, GPS is not reliable indoors and barometers do not provide sub meter accuracy. Consequently, other sensors are used such as optical flow cameras, external cameras, radio beacons, and lidar. This thesis will explore use of the lidar sensor.

8.2 Lidar use for positioning

Lidar is a rotating laser range finder that provides 2-Dimensional position information. A laser range finder calculates distance by measuring the time required for a laser to strike a target and bounce back. This time of flight measurement can be converted to distance using the speed of light. The lidars distance output is then encoded into polar coordinates ($r\angle\theta$). This data can then be converted to Cartesian coordinates with $x = r \cdot cos(\theta)$, $y = r \cdot sin(\theta)$. A example 2D lidar dataset of a room is shown in Fig. 8.1 where points represent the lidar's distance reading of the room.

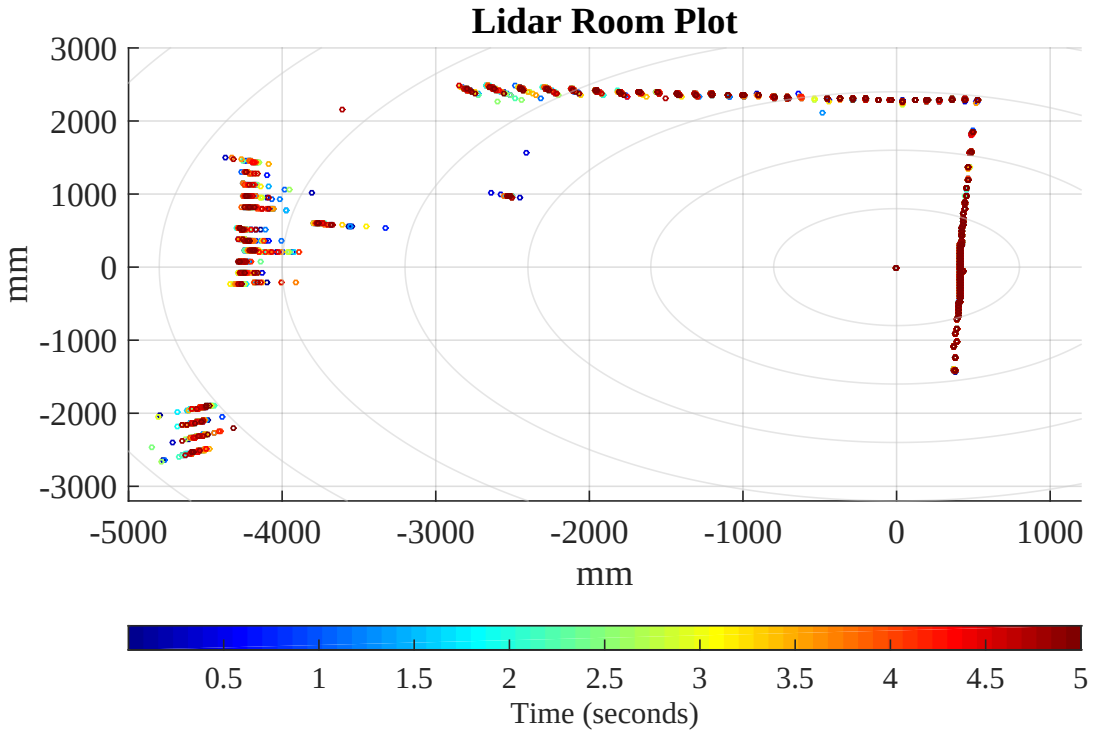

Figure 8.1: Lidar plot of room

In this plot, the change in color represents a change in time. For this dataset, the lidar was in a stationary position. With regards to the physical hardware, this dataset was taken with the XV-11 lidar. This lidar was used in order to help eliminate positional drift cheaply and in a computational efficient manner. Currently, this lidar is the most affordable lidar on the

market which provides motivation for its use. Commonly, in other research, more expensive lidars such as the Hokuyo UTM-30XL lidar was used[2][13]. Pictures of the XV-11 lidar and the Hokuyo UTM-30XL are shown in Fig. **8.2**.

(a) (b)

Figure 8.2: (a) Hokuyo UTM-30LX lidar used in [2] . (b) Neato XV-11 lidar device used in this project.

While the XV-11 lidar is more affordable, this price reduction comes at the cost of performance. Table 8.2 overviews the technical performance between the XV-11 lidar and the UTM-30LX Lidar.

Lidar device:	**Hokuyo UTM-30LX**	**Neato XV-11**
Points per revolution	1,440	360
Revolution speed (ms)	25	250
Max range (m)	30	4
Cost (USD)	4,825	150

Table 8.1: Specifications of the two lidars from Fig.8.2.

While lidar can provide crucial distance information, this data comes at the cost of significant computational requirements. For example, the UTM-30LX generates 57600 points per second. Once points are obtained, a significant amount of post processing must occur in order to transform this data into useful positional information. As a result, systems developed with lidars often consist of GHz processors with gigabytes of RAM. This chapter will focus on developing an algorithm to achieve this translational information with significantly less computation.

8.3 Method of parsing Lidar Data

In order to eliminate the quadcopter's positional drift $(\Delta x, \Delta y)$, an algorithm is required in order to estimate $(\hat{\Delta x}, \hat{\Delta y})$ from the lidar datasets. A example dataset of positional drift is shown in Fig. **8.3** where the lidar was moved left by roughly 600mm.

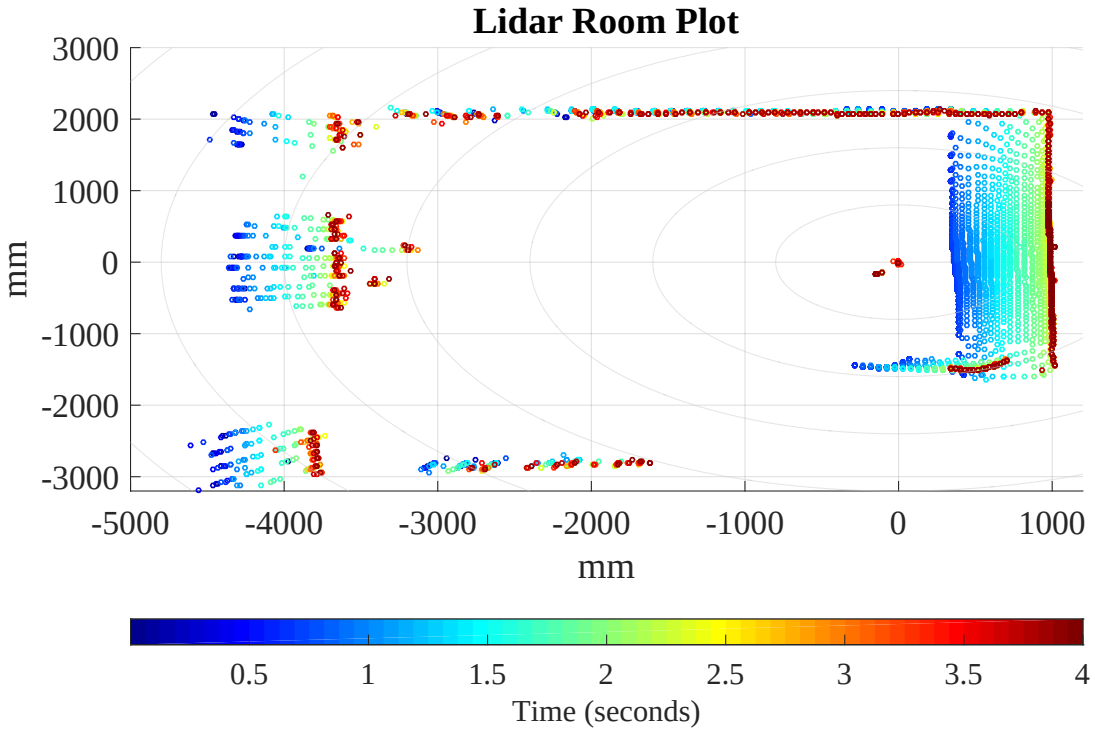

Figure 8.3: Lidar moved to the left by $\approx 600mm$

To estimate information from this lidar data, various computational geometry methods are employed such as iterative closest point (ICP), and iterative closest point line (ICPL) [12][37]. These methods are commonly used for solving point cloud translation problems. In addition to determining positional translation, these algorithms can also be employed to detect rotational differences and scaling differences between data sets. However, in order to limit scope, complexity, and computation, the lidar will be employed only for translational determination. The magnetometer for example, can be used to determine rotation. While ICP can estimate translation, ICP becomes less accurate with less data points and when

datasets that are taken at a further distance away. For example, if ICP is employed on the dataset in Fig. **8.3**, ICP would register positional changes in both X and Y as shown in Fig. **8.4**.

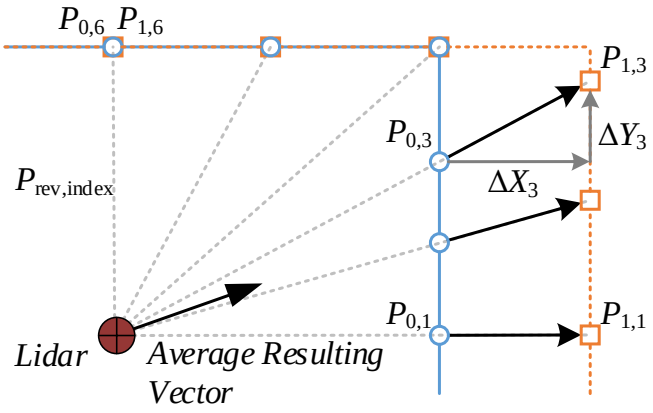

Figure 8.4: ICP Iteration

ICP operates with gradient descent and a example iteration is shown in equation **8.1** where x and y are arrays of N lidar points, where σ represents the gradient descent learning rate, and where $\Delta X, \Delta Y$ represent the resulting lidar translation.

$$\begin{aligned} \delta x = E\left[\sum_{i=0}^{i=N}(x_i - x_{cp})\right], \qquad \delta y = E\left[\sum_{i=0}^{i=N}(y_i - y_{cp})\right] \\ \Delta x = \Delta x + \delta x, \qquad \Delta y = \Delta y + \delta y \\ x = \sum_{i=0}^{i=N}(x_i + \sigma \cdot \delta x), \qquad y = \sum_{i=0}^{i=N}(y_i + \sigma \cdot \delta y) \end{aligned} \tag{8.1}$$

Note that additional computation is required in order to find (x_{cp}, y_{cp}) which represent the coordinates of the closest point from a previous lidar data set to a present given point (x_i, y_i). Convergence requirements and the value of the learning rate would be determined by a designer on a application basis. However, due to the geometry nature of ICP acting on lidar data, this algorithm may not converge to a correct value.

8.4 Iterative Closest Line

This chapter will overview a specific implementation of the iterative closest line (ICL) algorithm developed for parsing lidar data efficiently and accurately. ICL is based on a closest point to line metric as opposed to ICP which is based on a closest point to point metric. In ICL, the point P_{cp} with coordinates (x_{cp}, y_{cp}) is replaced with a point P_{CL} with coordinates (x_{CL}, y_{CL}). The point P_{CL} is located on line between the two previous closest points. In addition, P_{CL} is also the closest point on that line to the point being compared. The concept of P_{CL} points is shown in Fig. **8.5** where lidar points are denoted in the form of $P_{lidarRevolution,index}$.

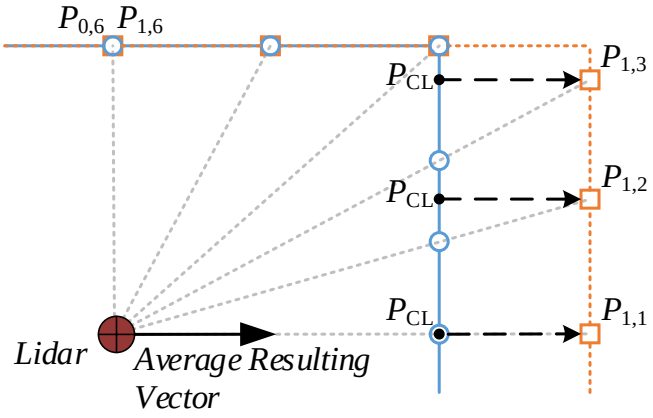

Figure 8.5: ICP Iteration

The point (x_{CL}, y_{CL}) is calculated using equation **8.2** where points $(x_1, y_1), (x_2, y_2)$ represent the two closest points from a prior lidar revolution with respect to a new lidar point (x_3, y_3). Note that in equation **8.2**, a, b, c represent parameters of the general line equation which is expressed as $a \cdot x + b \cdot y + c = 0$. Lines were formulated in this manner as opposed to slope intercept form in order to mitigate potential devisions by 0.

$$
\begin{aligned}
a &= y_2 - y_1, \quad b = x_1 - x_2, \quad c = -by_1 - ax_1 \\
x_{CL} &= \frac{b(bx_3 - ay_3) - ac}{a^2 + b^2} \\
y_{CL} &= \frac{a(-bx_3 + ax_3) - bc}{a^2 + b^2}
\end{aligned} \tag{8.2}
$$

With the calculation procedure of (x_{CL}, y_{CL}) complete, the next step in ICL algorithm is to formulate and minimize a cost function J. The ICL cost function J shown in equation **8.3** where i represents the index of N lidar points.

$$
J = \sum_{i=1}^{N} (x_i - x_{CL})^2 + (y_i - y_{CL})^2 \tag{8.3}
$$

This cost function can be minimized iteratively through gradient descent. To use gradient descent, the partial derivatives must be calculated as shown in equation **8.4**.

$$
\begin{aligned}
\delta x_k &= \sum_{i=1}^{N} \frac{\partial J_{k,i}}{\partial x} = \sum_{i=1}^{N} (x_{k,i} - x_{CL}) \\
\delta y_k &= \sum_{i=1}^{N} \frac{\partial J_{k,i}}{\partial y} = \sum_{i=1}^{N} (y_{k,i} - y_{CL})
\end{aligned} \tag{8.4}
$$

Now that the necessary mathematical concepts have been overviewed, a basic sudo code example for ICL is shown in Fig. **8.6**.

While this code example only covers a single lidar revolution, a more complete example can be found at www.githuburlgoeshere.com. The performance of this algorithm in comparison to vanilla ICP is shown in Fig. **8.7** acting upon the dataset shown in Fig. **8.3**.

ICL and ICP were performed on every consecutive set of lidar data. Δx represents the rate

```
int N = 360; // 360 points per revolution
float α = 0.5 // Learning Rate
int iterationCount = 10 // Fixed number of iterations
float δx,δy,Δx,Δy,x_CL,y_CL =0; //intermediate variables
float x[] = {x1, ... xn}; //Array of recent X lidar points
float y[] = {y1, .. yn}; // Array of recent Y lidar points
float xPrevious[] = {x1, ... xn}; //Array of previous X lidar points
float yPrevious[] = {y1, .. yn}; // Array of previous Y lidar points

void ICL(){

for( j = 0; j<iterationCount;j++)
{
  for( i = 0; i < N; i++){ //accumulate delta terms.
    x_CL = findCL(x[i],xPrevious); //Find closest point line
    y_CL = findCL(y[i],yPrevious);
    δx = δx + (x[i] - x_CL);
    δy = δy + (y[i] - y_CL);
  }
  for( i = 0; i < N; i++){ // Simultaneous update all points
    x[i] = x[i] - α * δx/N;
    y[i] = y[i] - α * δy/N;
  }
  Δx = Δx + δx/N; // accumulate displacements
  Δy = Δy + δy/N; // accumulate displacement
  δx = 0; δy = 0; // Reset delta values for next iteration
}
printf(Δx , Δy) // Output results

}
```

Figure 8.6: Code example of ICL

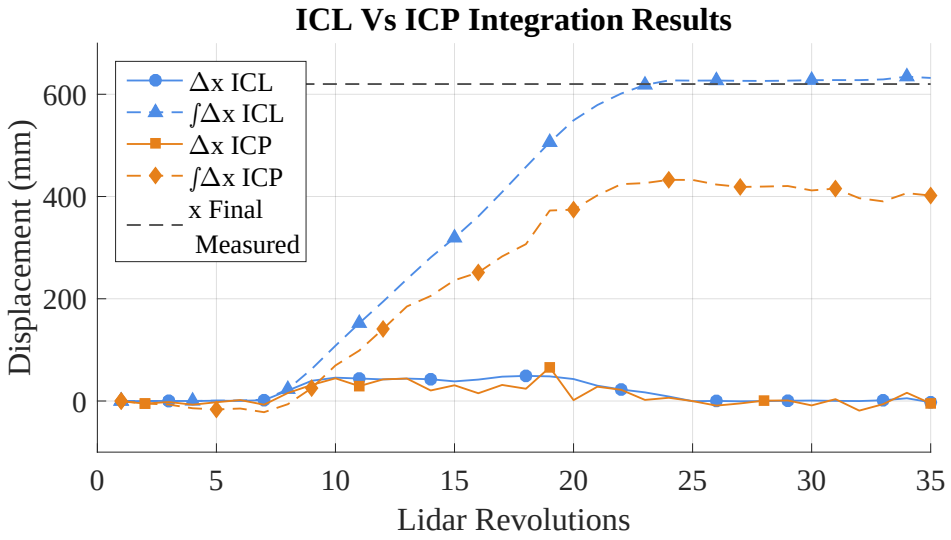

Figure 8.7: ICP and ICL integration results acting on dataset in Fig. **8.3**

.

of drift while $\int \Delta x$ represents the total accumulated drift. As seen in Fig. **8.7**, ICL error is smaller over time which results in the correct integration distance over time. In contrast, ICP has non negligible error resulting in significant accumulated error over time. Consequently, this implementation of ICL is a preferred candidate for parsing lidar data on the fly.

8.5 Lidar Integration with Quadcopter Control System

This section will overview a simple proposed method of integrating lidar information into the quadcopters control system such that positional drift is reduced. As shown in Sections 8.3 and 8.4, ICP and ICL can act on lidar data to obtain positional drift estimations $\Delta x, \Delta y$. An additional PID control loop can then be added acting on the quadcopter's ϕ, θ orientation angles to drive $\Delta x, \Delta y$ to zero respectively. This control scheme is shown in Fig. **8.9** which is an extension of control system shown in Fig. **5.2** adding lidar as well as a sonar z height feedback.

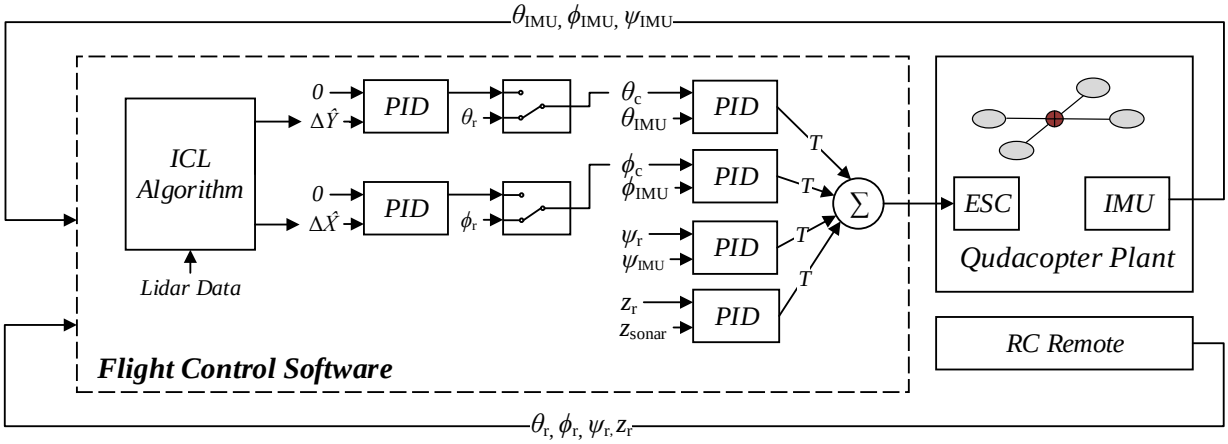

Figure 8.8: Quadcopter control diagram with lidar and sonar inputs added

8.6 Control System Testing, Simulation and Conclusion

The control system proposed in Fig. **8.9** was tested only in simulation due to time constraints. Flying a quadcopter with the XV-11 lidar would be challenging due to its heavy weight in addition to significant torque oscillations that would be coupled to the frame quad-frame. Consequently, this control scheme was tested in matlab using a similar mathematical model[19]. In this model, an external disturbance was added causing drift in both the x and y planes. The control system in Fig. **8.9** then acted upon ϕ, θ to counteract this drift.

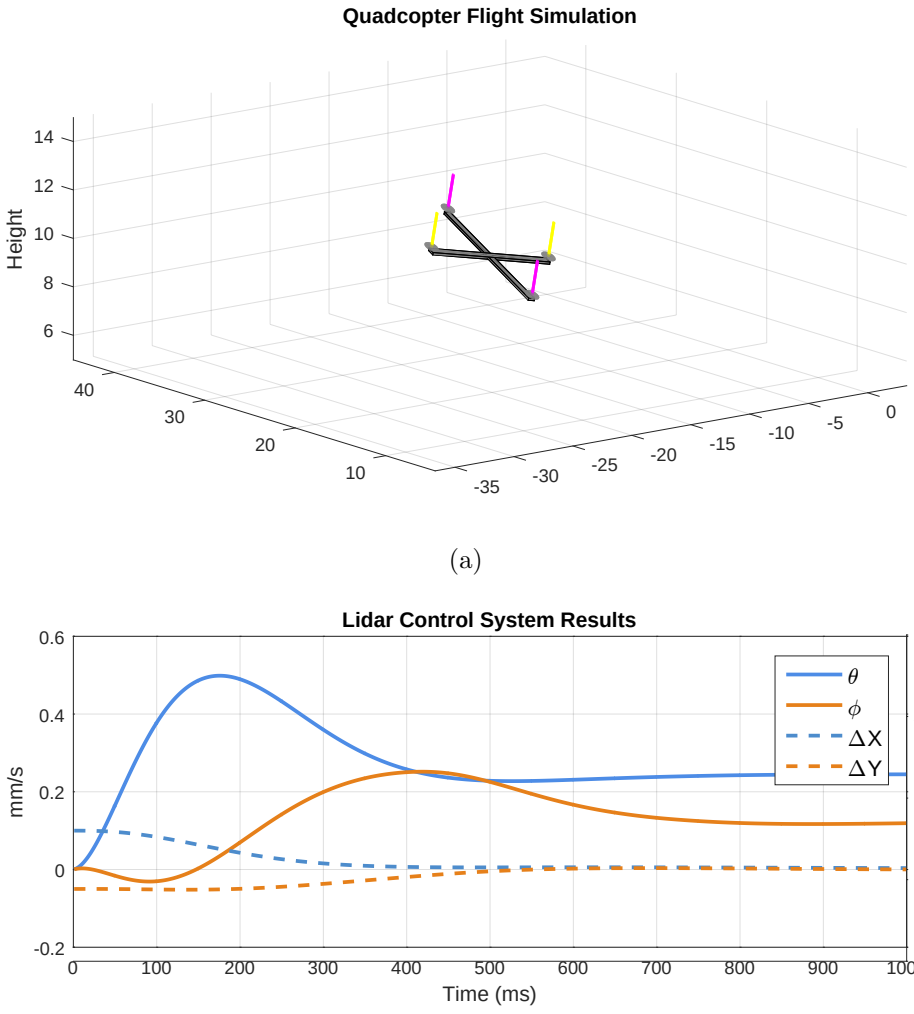

Figure 8.9: (a) Quadcopter simulation with external disturbance. (b) Plot of positional drift elimination

CHAPTER 9

Conclusion and Future Work

9.1 Flight Performance

This section overviews the performance of meeting the control objectives proposed in equation **3.1**. Using the control system proposed in chapter 5 and the hardware shown in chapter 7, the quadcopter was able to achieve flight with minimal steady state error. A segment of data taken during a flight hover test is shown in Fig. **9.1**.

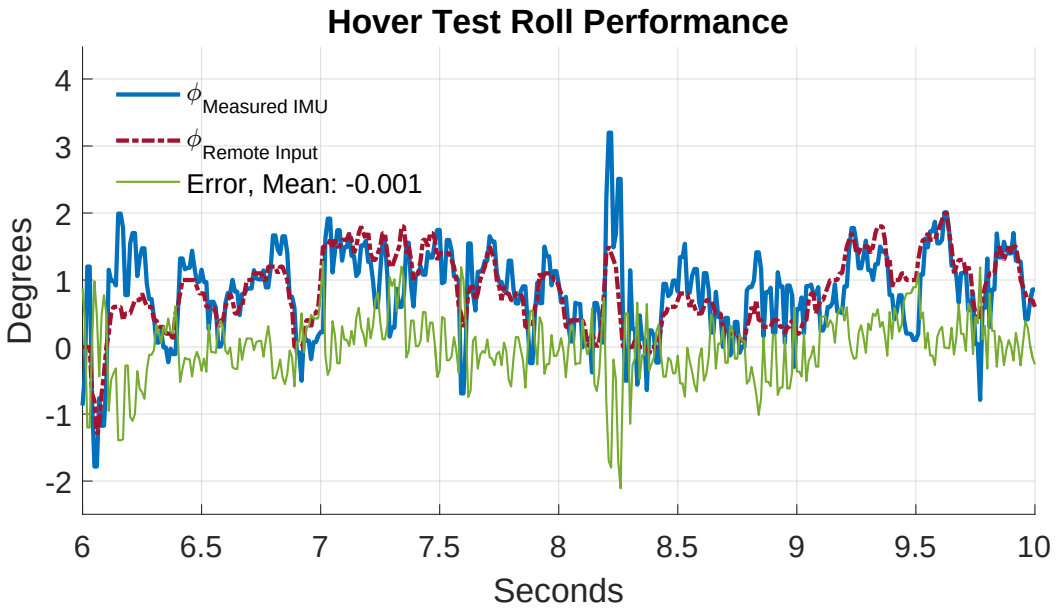

Figure 9.1: Roll performance in hover test of quadcopter

Note that in this flight test, a human was controlling the quadcopter attempting to make the qudacopter hover in place. As a result of this, the user commanded roll, ϕ_{Remote} is not 0. Consequently, the error $\phi_{Remote} - \phi_{Measured}$, can be used as a performance metric. For the

entire duration of this test, the error averaged to be 0.001^o. However, the standard deviation of the error is 0.4816 degrees. In other-words, roughly 70% of the time the error is within 0.5^o of the target. This noise error is in part due to the noise of the user generated control signal and in part due to jitter/noise in the control system. While pitch and roll have similar performance, yaw had the most control error over time. This is in part due to the control system gains and it is also in part due to the quadcopter design not having a control input that acts directly on yaw. Recall from the physical model that yaw control is achieved by a differential torque from clockwise and counter clockwise spinning motors. In contrast, pitch and roll can be controlled directly by the forces exerted by the propellers on the frame. The control system errors for pitch, roll, and yaw are shown in Fig. **9.2**.

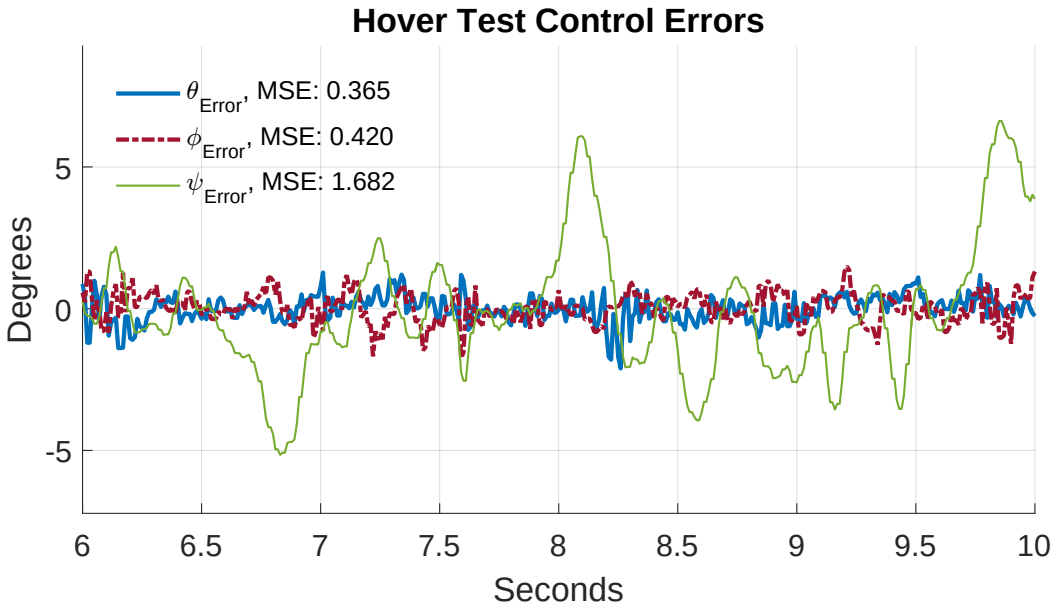

Figure 9.2: Pitch, roll, and yaw performance during hover test of quadcopter

Using the dataset in Fig. **9.2**, the mean squared error (MSE) was generated for each control axis. The MSE tracks the controllability of each axis. For reference, a flight video of the drone can be seen at: https://www.youtube.com/watch?v=cArrBF8TGZQ .

9.2 Conclusions

The main purpose of this thesis was to develop both the hardware and software for a quadcopter system. Chapter 3 developed a control update laws as well as control objectives. Chapter 4 developed a 9 DOF fusion filter to provide accurate estimations of orientation. Chapter 5 demonstrated a control system to achieve stable auto leveling flight using a series of PID controllers. Chapter 6 overviews the RF hardware involved in creating the transcieving link between the remote and the quadcopter. Chapter 7 specifies the other hardware involved in the system such as the flight controller and electronic speed controllers. Chapter 8.4 demonstrates theory involved with autonomous flight and using a lidar to maintain position while indoors. Finally, the conclusion demonstrated flight results of the overall system.

9.3 Future Work

Provided the time and future opportunity presents itself, improvements would be made IMU fusion filter as well as the control system. Currently, the IMU filter operates on Euler angles when ideally it should be based upon quaternions to avoid singularities. In addition, quaternions also allow for true linear spherical interpolation where as low pass filtering Euler angles does not produce a linear response. With regards to the control system, the first thing that would be improved is the PID control system performance. The current balancing action is somewhat noisy and the yaw control is lacking. In addition to PID control, other control techniques could be implemented such as linear quadratic regulator (LQR) as well as model predictive control (MPC). Another improvement would be to integrate the designed electronic speed controllers into quadcopter system. A final improvement would be to mount

the lidar to the quadcopter and implement the ICL algorithm in real time.

APPENDIX A

Hardware schematics and PCBs

A.1 Hardware Schematics

The following are electrical schematics used in the creation of the quadcopter hardware. This hardware was developed in an educational licensed version of Altium at Marquette University. The PCB for these electronic assemblies were manufactured through www.oshpark.com. The boards were then populated and reflowed at the Marquette Embedded Systems Laboratory.

Marq Drone Flight Controller

2. Power
3. Micro

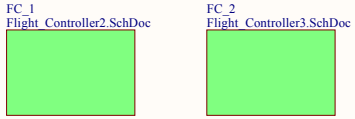

Power & Connectors & Sensors

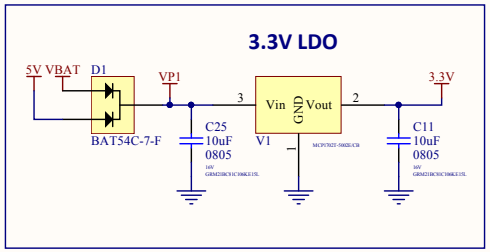

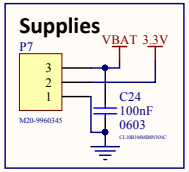

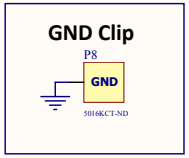

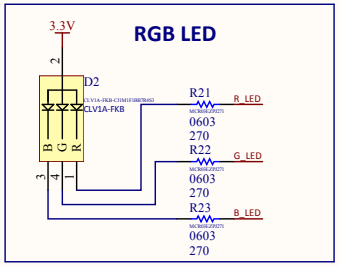

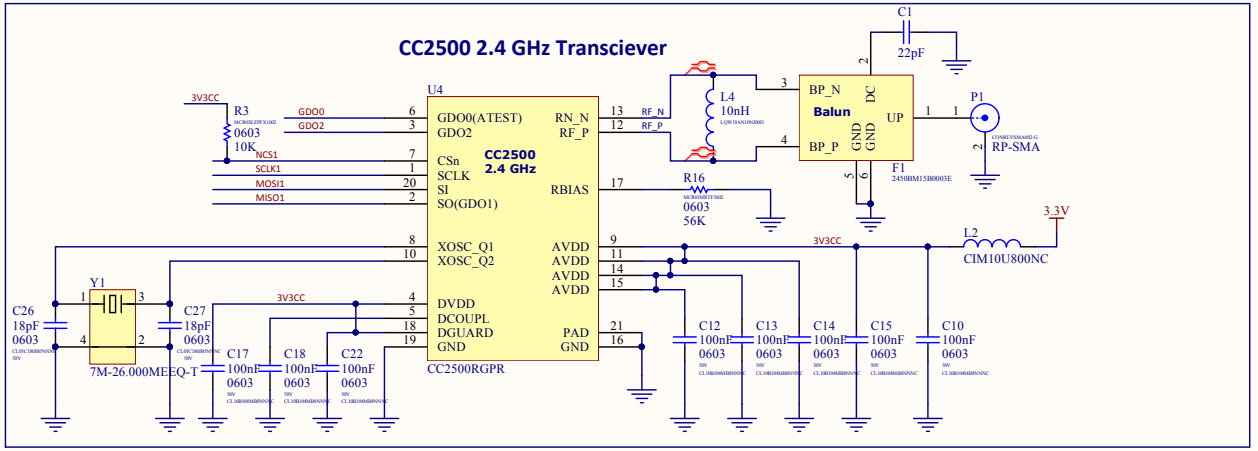

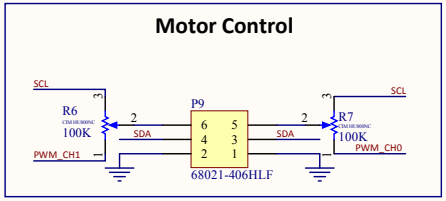

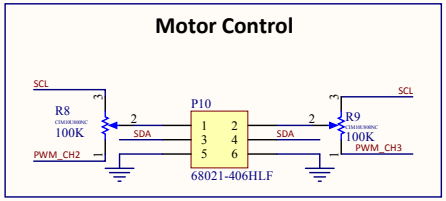

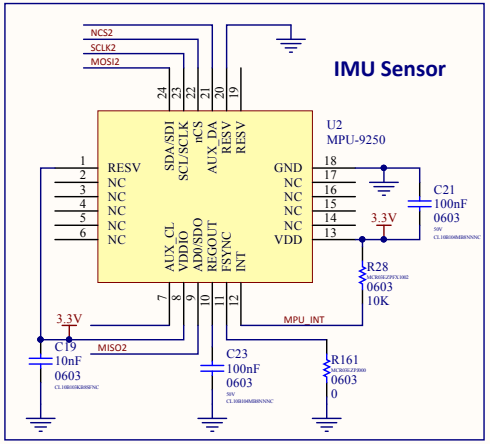

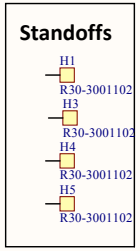

Micro

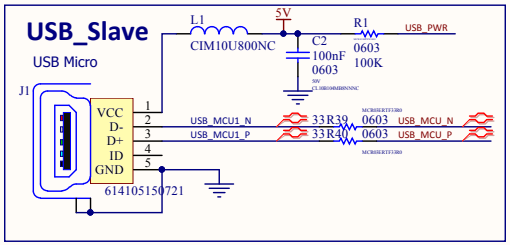
USB_Slave
USB Micro
J1
VCC
D-
D+
ID
GND
614105150721
L1
CIM10U800NC
5V
C2
100nF
0603
R1
0603
100K
USB_PWR
USB_MCU1_N
USB_MCU1_P
33R39
33R40
0603
USB_MCU_N
USB_MCU_P

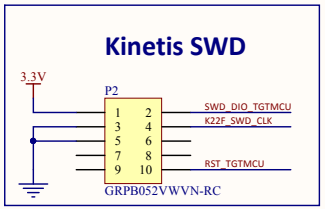
Kinetis SWD
3.3V
P2
SWD_DIO_TGTMCU
K22F_SWD_CLK
RST_TGTMCU
GRPB052VWVN-RC

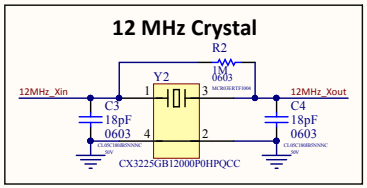
12 MHz Crystal
R2
1M
0603
Y2
12MHz_Xin
12MHz_Xout
C3
18pF
0603
C4
18pF
0603
CX3225GB12000P0HPQCC

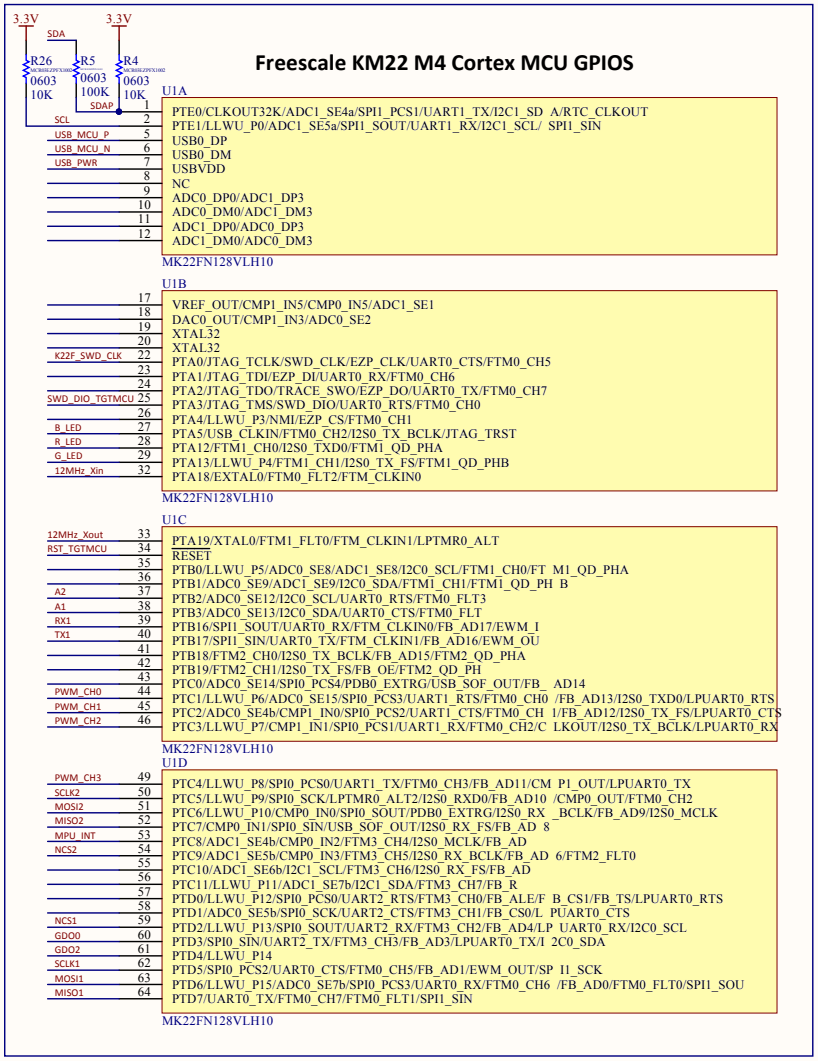
Freescale KM22 M4 Cortex MCU GPIOS
3.3V
SDA
R26
R5
R4
0603
10K
100K
SDAP
SCL
U1A
PTE0/CLKOUT32K/ADC1_SE4a/SPI1_PCS1/UART1_TX/I2C1_SD A/RTC_CLKOUT
PTE1/LLWU_P0/ADC1_SE5a/SPI1_SOUT/UART1_RX/I2C1_SCL/ SPI1_SIN
USB0_DP
USB0_DM
USBVDD
NC
ADC0_DP0/ADC1_DP3
ADC0_DM0/ADC1_DM3
ADC1_DP0/ADC0_DP3
ADC1_DM0/ADC0_DM3
MK22FN128VLH10
U1B
VREF_OUT/CMP1_IN5/CMP0_IN5/ADC1_SE1
DAC0_OUT/CMP1_IN3/ADC0_SE2
XTAL32
XTAL32
PTA0/JTAG_TCLK/SWD_CLK/EZP_CLK/UART0_CTS/FTM0_CH5
PTA1/JTAG_TDI/EZP_DI/UART0_RX/FTM0_CH6
PTA2/JTAG_TDO/TRACE_SWO/EZP_DO/UART0_TX/FTM0_CH7
PTA3/JTAG_TMS/SWD_DIO/UART0_RTS/FTM0_CH0
PTA4/LLWU_P3/NMI/EZP_CS/FTM0_CH1
PTA5/USB_CLKIN/FTM0_CH2/I2S0_TX_BCLK/JTAG_TRST
PTA12/FTM1_CH0/I2S0_TXD0/FTM1_QD_PHA
PTA13/LLWU_P4/FTM1_CH1/I2S0_TX_FS/FTM1_QD_PHB
PTA18/EXTAL0/FTM0_FLT2/FTM_CLKIN0
MK22FN128VLH10
U1C
PTA19/XTAL0/FTM1_FLT0/FTM_CLKIN1/LPTMR0_ALT
RESET
PTB0/LLWU_P5/ADC0_SE8/ADC1_SE8/I2C0_SCL/FTM1_CH0/FT M1_QD_PHA
PTB1/ADC0_SE9/ADC1_SE9/I2C0_SDA/FTM1_CH1/FTM1_QD_PH B
PTB2/ADC0_SE12/I2C0_SCL/UART0_RTS/FTM0_FLT3
PTB3/ADC0_SE13/I2C0_SDA/UART0_CTS/FTM0_FLT
PTB16/SPI1_SOUT/UART0_RX/FTM_CLKIN0/FB_AD17/EWM_I
PTB17/SPI1_SIN/UART0_TX/FTM_CLKIN1/FB_AD16/EWM_OU
PTB18/FTM2_CH0/I2S0_TX_BCLK/FB_AD15/FTM2_QD_PHA
PTB19/FTM2_CH1/I2S0_TX_FS/FB_OE/FTM2_QD_PH
PTC0/ADC0_SE14/SPI0_PCS4/PDB0_EXTRG/USB_SOF_OUT/FB_ AD14
PTC1/LLWU_P6/ADC0_SE15/SPI0_PCS3/UART1_RTS/FTM0_CH0 /FB_AD13/I2S0_TXD0/LPUART0_RTS
PTC2/ADC0_SE4b/CMP1_IN0/SPI0_PCS2/UART1_CTS/FTM0_CH 1/FB_AD12/I2S0_TX_FS/LPUART0_CTS
PTC3/LLWU_P7/CMP1_IN1/SPI0_PCS1/UART1_RX/FTM0_CH2/C LKOUT/I2S0_TX_BCLK/LPUART0_RX
MK22FN128VLH10
U1D
PTC4/LLWU_P8/SPI0_PCS0/UART1_TX/FTM0_CH3/FB_AD11/CM P1_OUT/LPUART0_TX
PTC5/LLWU_P9/SPI0_SCK/LPTMR0_ALT2/I2S0_RXD0/FB_AD10 /CMP0_OUT/FTM0_CH2
PTC6/LLWU_P10/CMP0_IN0/SPI0_SOUT/PDB0_EXTRG/I2S0_RX _BCLK/FB_AD9/I2S0_MCLK
PTC7/CMP0_IN1/SPI0_SIN/USB_SOF_OUT/I2S0_RX_FS/FB_AD 8
PTC8/ADC1_SE4b/CMP0_IN2/FTM3_CH4/I2S0_MCLK/FB_AD
PTC9/ADC1_SE5b/CMP0_IN3/FTM3_CH5/I2S0_RX_BCLK/FB_AD 6/FTM2_FLT0
PTC10/ADC1_SE6b/I2C1_SCL/FTM3_CH6/I2S0_RX_FS/FB_AD
PTC11/LLWU_P11/ADC1_SE7b/I2C1_SDA/FTM3_CH7/FB_R
PTD0/LLWU_P12/SPI0_PCS0/UART2_RTS/FTM3_CH0/FB_ALE/F B_CS1/FB_TS/LPUART0_RTS
PTD1/ADC0_SE5b/SPI0_SCK/UART2_CTS/FTM3_CH1/FB_CS0/L PUART0_CTS
PTD2/LLWU_P13/SPI0_SOUT/UART2_RX/FTM3_CH2/FB_AD4/LP UART0_RX/I2C0_SCL
PTD3/SPI0_SIN/UART2_TX/FTM3_CH3/FB_AD3/LPUART0_TX/I 2C0_SDA
PTD4/LLWU_P14
PTD5/SPI0_PCS2/UART0_CTS/FTM0_CH5/FB_AD1/EWM_OUT/SP I1_SCK
PTD6/LLWU_P15/ADC0_SE7b/SPI0_PCS3/UART0_RX/FTM0_CH6 /FB_AD0/FTM0_FLT0/SPI1_SOU
PTD7/UART0_TX/FTM0_CH7/FTM0_FLT1/SPI1_SIN
MK22FN128VLH10

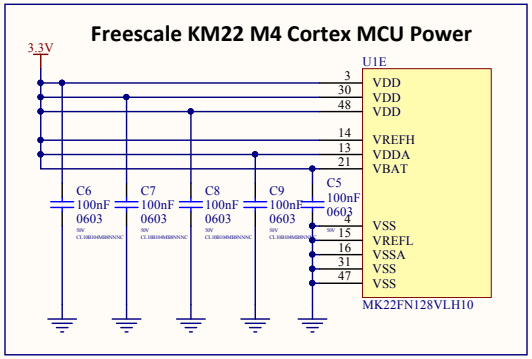
Freescale KM22 M4 Cortex MCU Power
3.3V
U1E
VDD
VDD
VDD
VREFH
VDDA
VBAT
VSS
VREFL
VSSA
VSS
VSS
C6
C7
C8
C9
C5
100nF
0603
MK22FN128VLH10

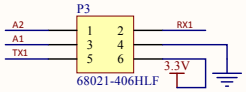
P3
A2
A1
TX1
RX1
3.3V
68021-406HLF

A.5 Flight Controller Schematic

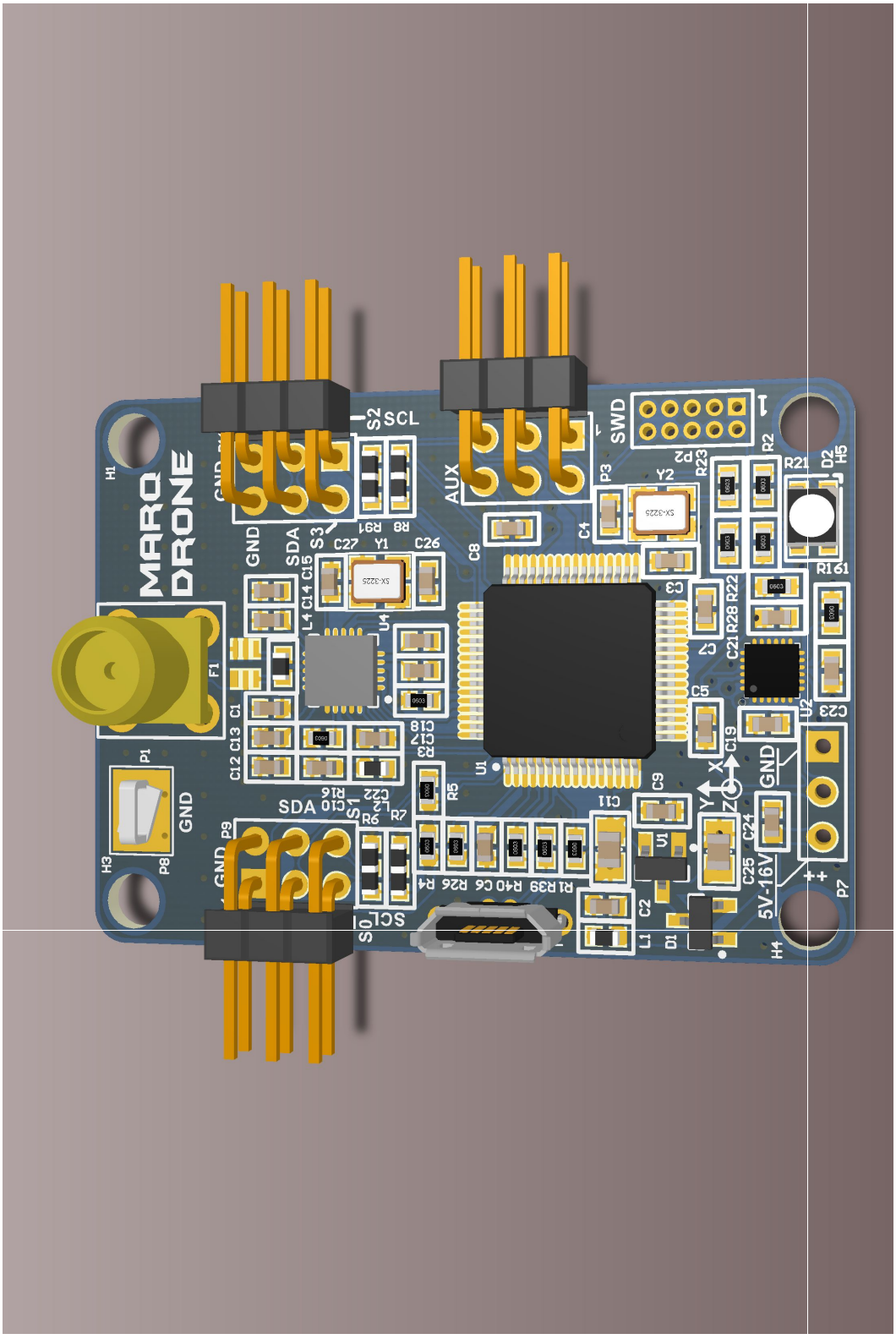

Sensorless Brushless Motor Controller

A.6 ESC Schematic

Power System

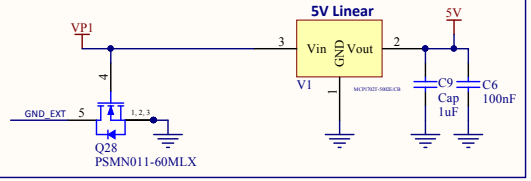

USB_Slave

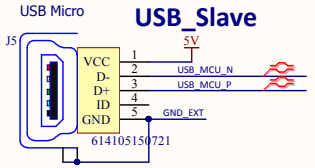

Kinetis SWD

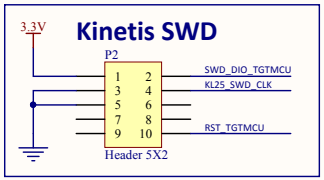

Sudo Neutral

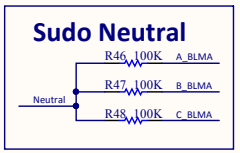

12 MHz Crystal

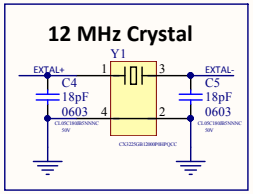

Bulk Capacitence

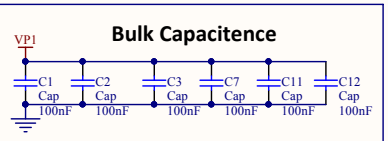

External COM

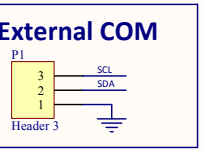

1 Phase A

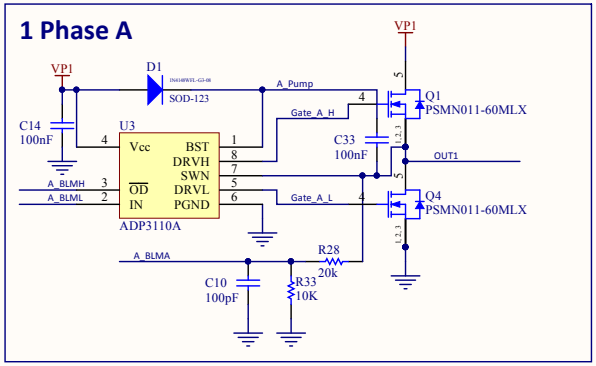

1 Phase B

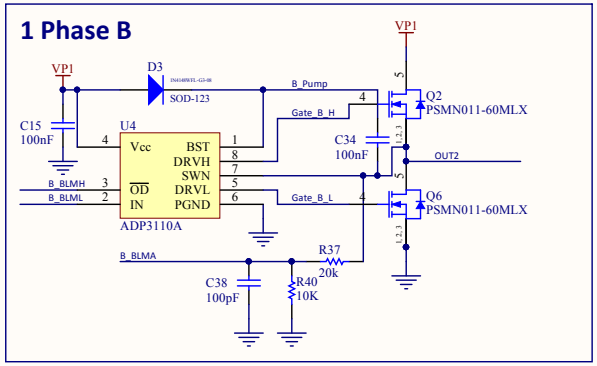

1 Phase C

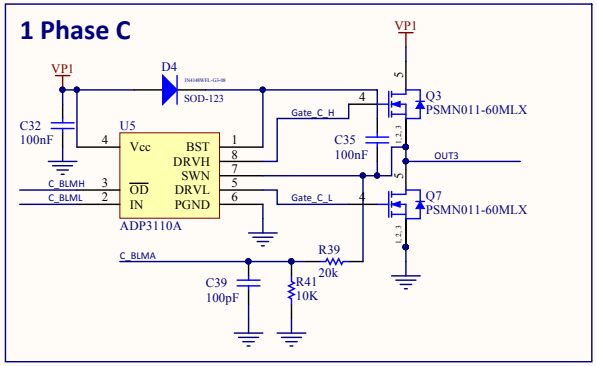

EXT LED

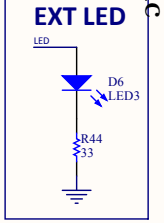

Kinetis Bank A

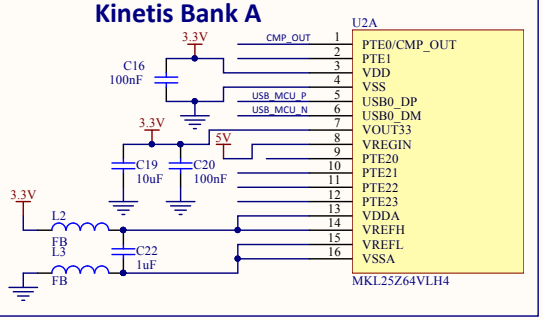

Kinetis Bank B

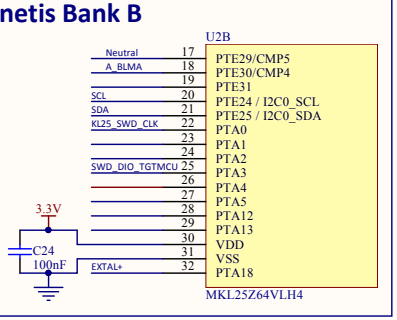

Kinetis Bank C

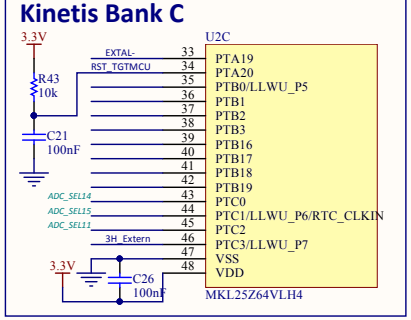

Kinetis Bank D

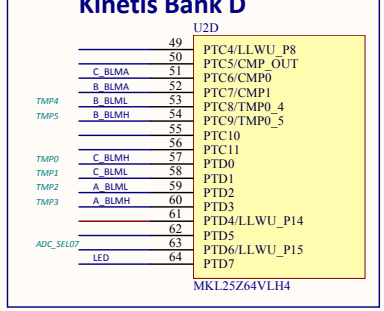

Title	Sensorless Brushless Motor Controller	
Size: A3	Number	Revision: Rev 1
Date: 9/7/2015		Sheet of
File: C:\Users\..\ESC3.SchDoc		Drawn By: Nathan Zimmerman

A.7 ESC Schematic

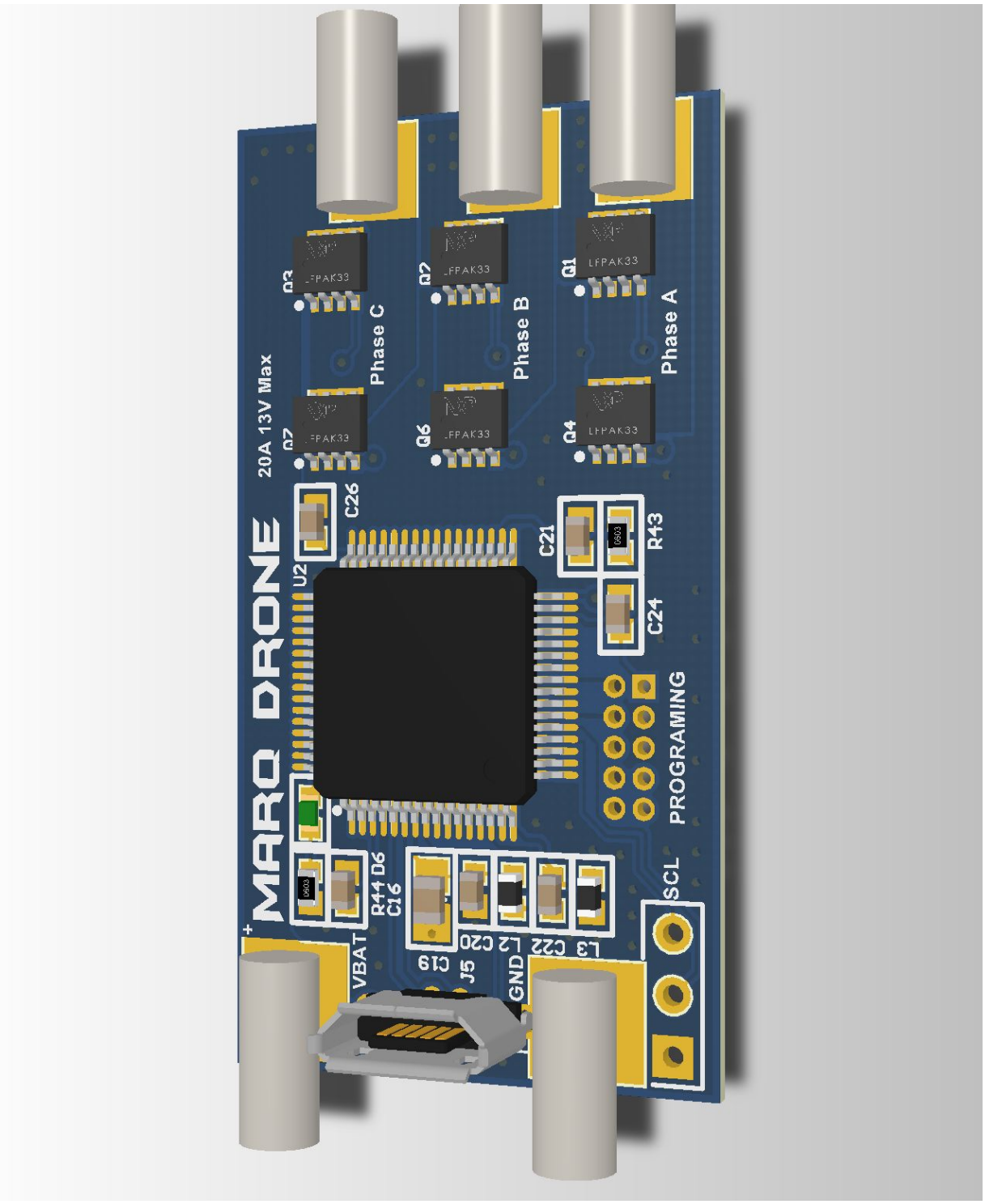

A.8 ESC Schematic

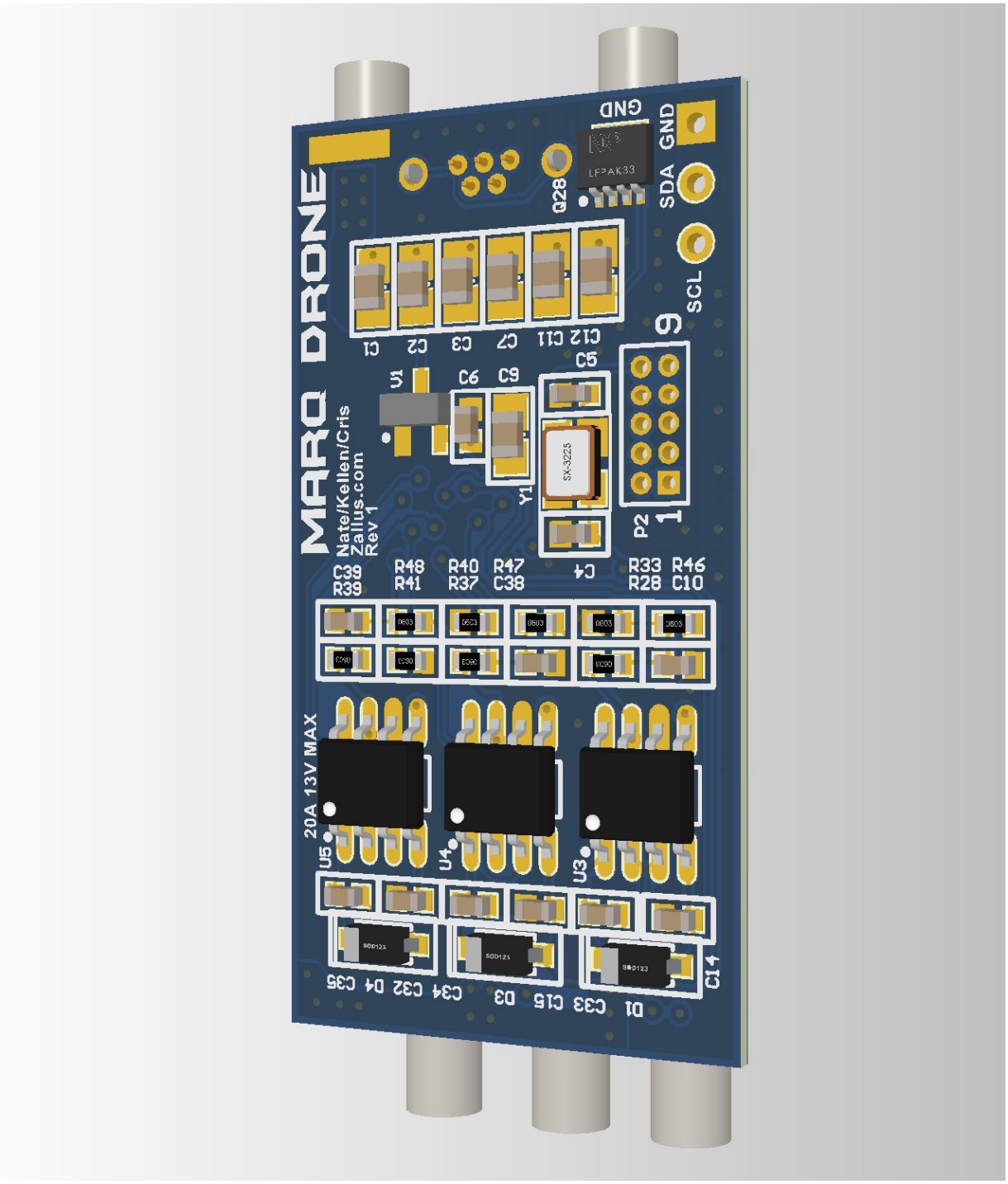

A.9 RF Controller Schematic

Lipo Protection & Power System

Lithium Charger

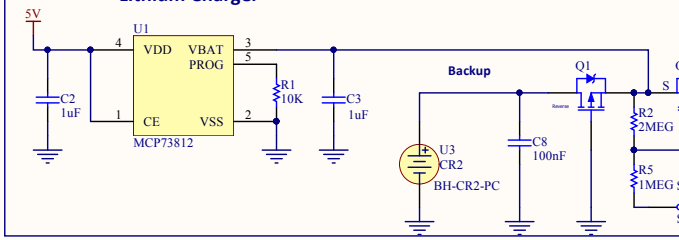

Backup

3.3V LDO Reg

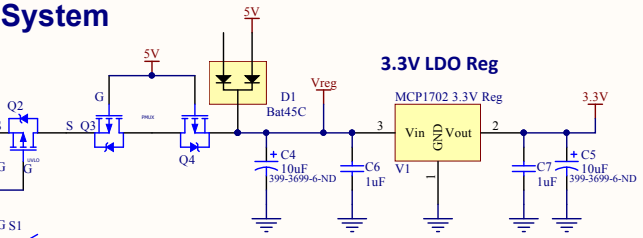

Reset Button

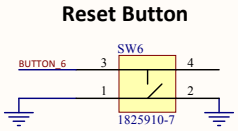

Reset Button

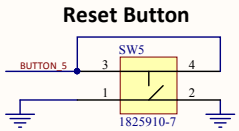

Reset Button

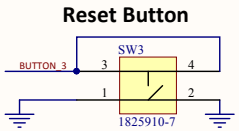

Reset Button

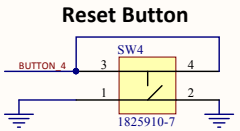

Reset Button

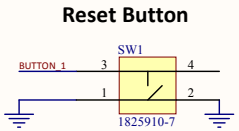

Reset Button

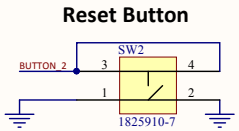

Joystick Input

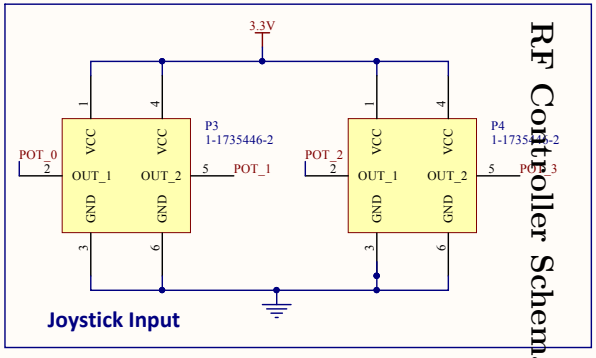

LEDS

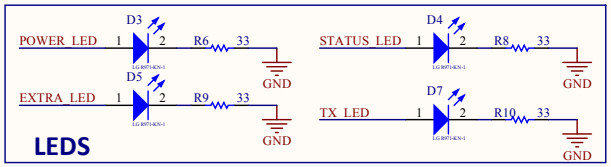

USB_Slave

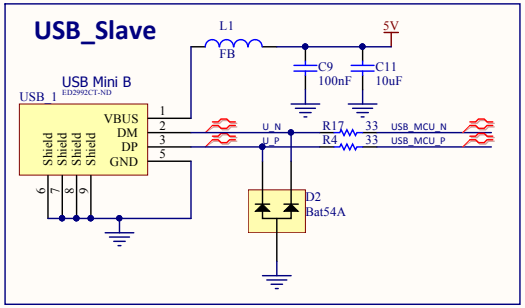

Kinetis SWD

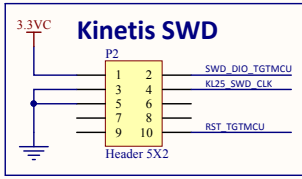

CC2500 2.4 GHz Transciever

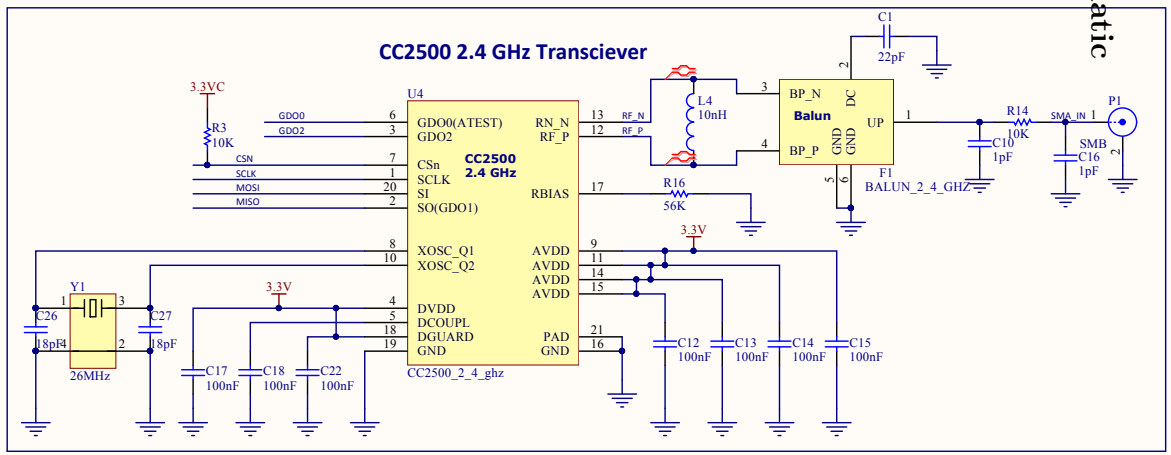

Kinetis Bank A

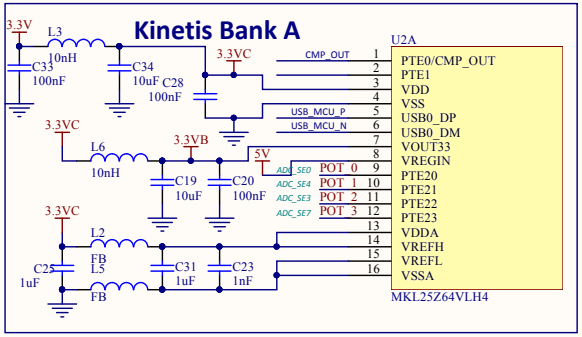

Kinetis Bank B

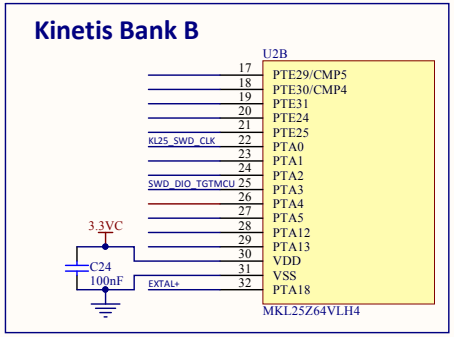

Kinetis Bank C

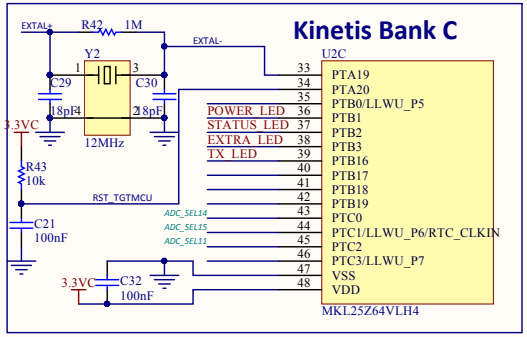

Kinetis Bank D

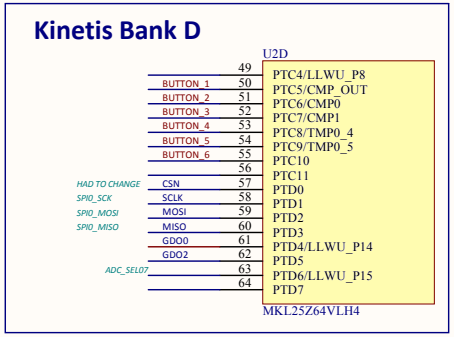

P6 Header 4

P5 Header 4

Title		91
Size A3	Number	Revision 1
Date: 10/4/2015		Sheet of
File: C:\Users\...\RF_Controller.SchDoc		Drawn By: Kellen Carey

A.10 RF Controller Schematic

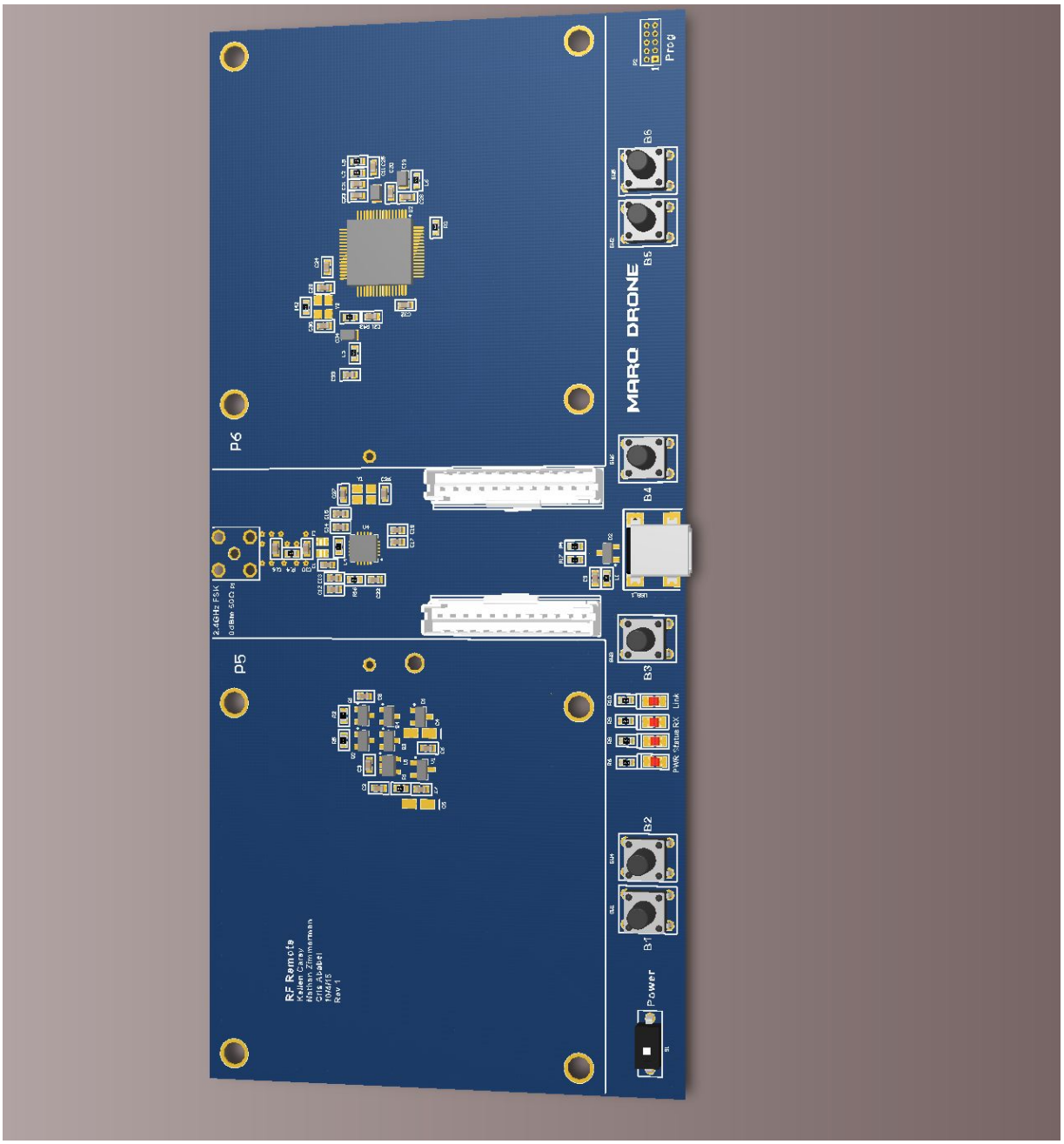

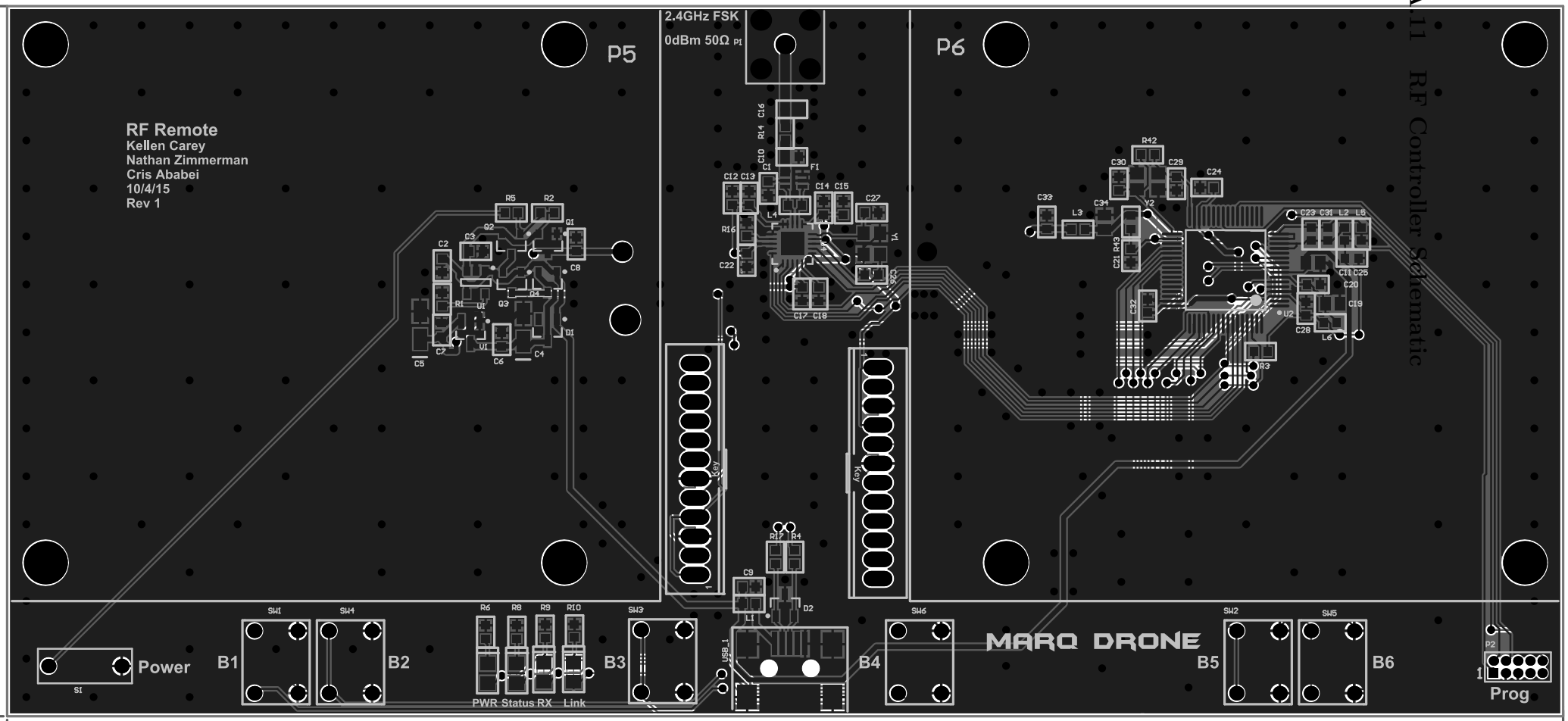

2913.39

6377.95

Sensorless 10A ESC REV2.0

Nathan Zimmerman

A.12 ESC Dev Board

Over Current Latch Circuit Trip 12A

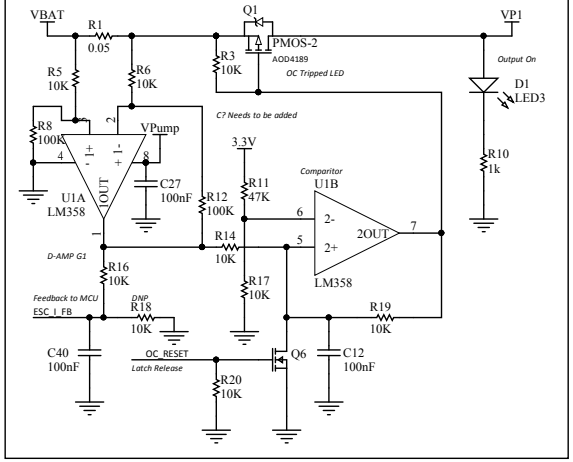

Doubler Charge Pump

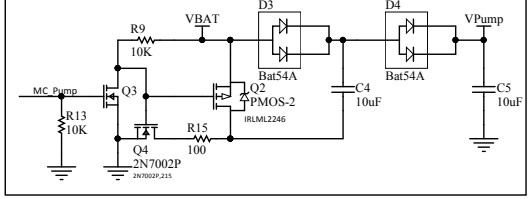

Power System

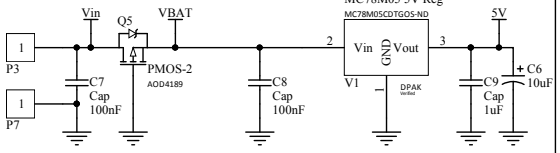

External Motor

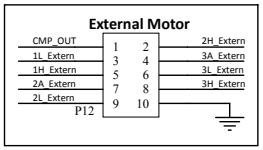

USB_Slave

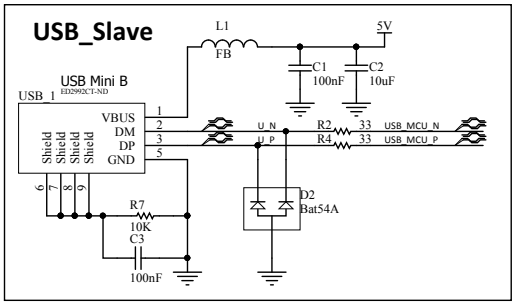

Power Rails

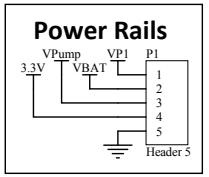

Kinetis SWD

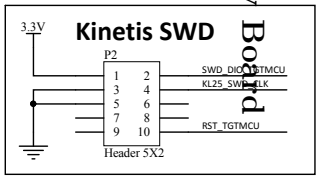

1 Phase A

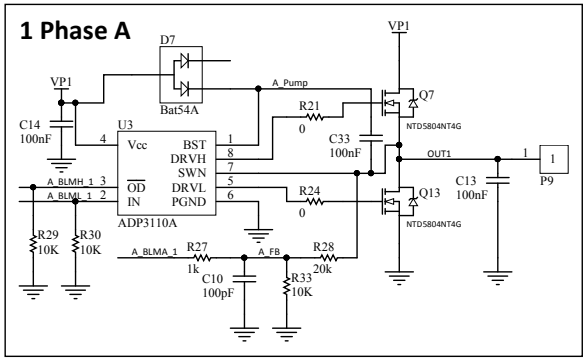

1 Phase B

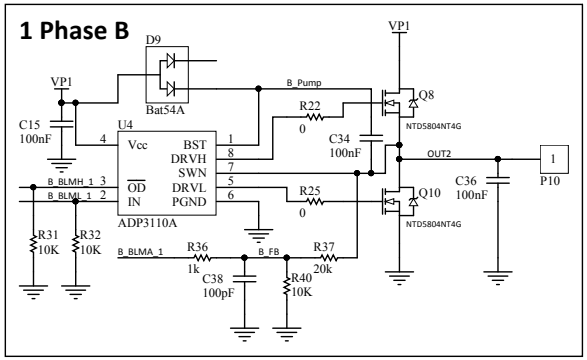

1 Phase C

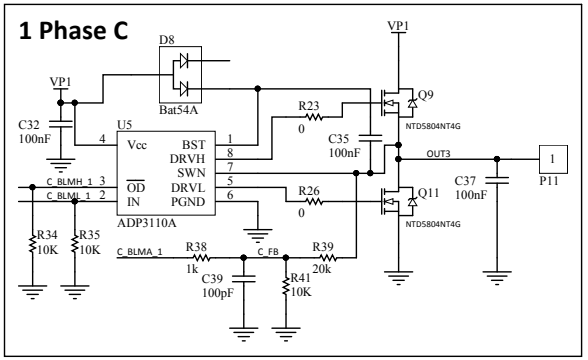

Standoffs

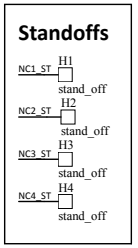

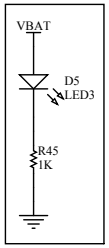

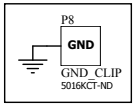

Phase Signal Interconnects

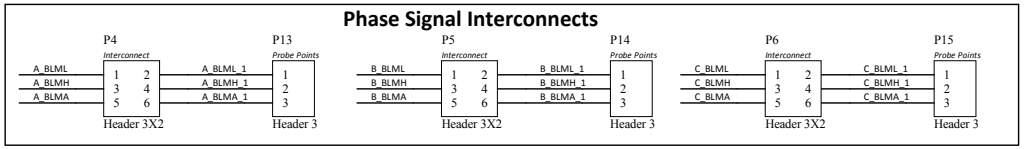

Sudo Neutral

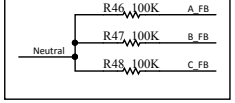

Bulk C

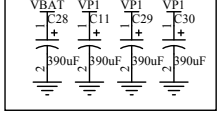

Kinetis Bank A

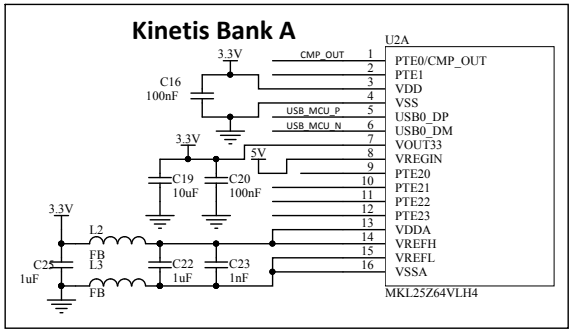

Kinetis Bank B

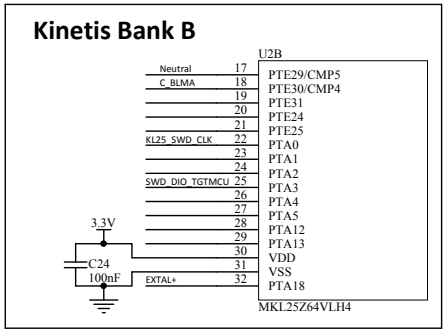

Kinetis Bank C

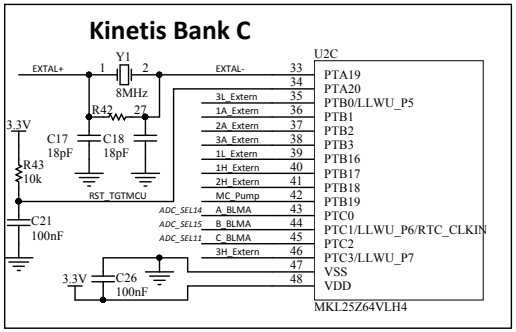

Kinetis Bank D

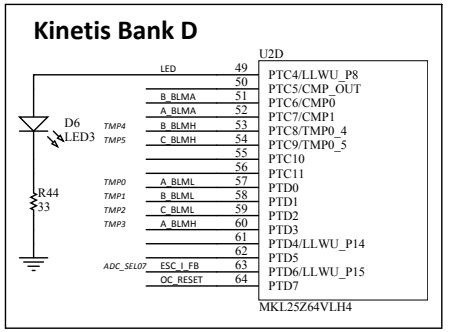

ESC Rev 2

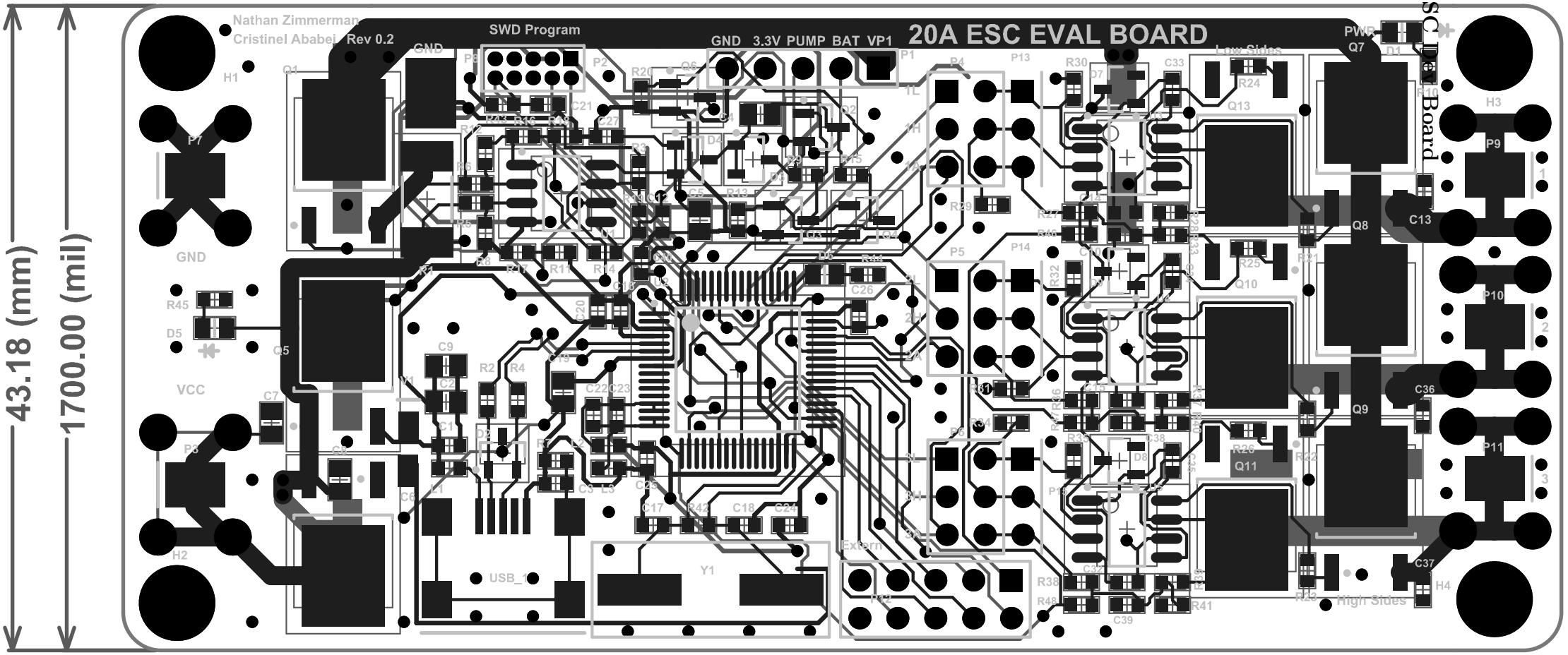

Nathan Zimmerman
Rev 2

APPENDIX B

Transmission Line Calculations

B.1 Microstrip Line Z_o Calculation

The following are empirical formulas used to calculate the characteristic impedance of a microstrip line where W is the width of the track, ϵ_r is the relative permittivity, t is the thickness of the track, and h is the height of the dielectric[38]. Care should be taken that the correct relative permittivity is selected with respect to the frequency of operation.

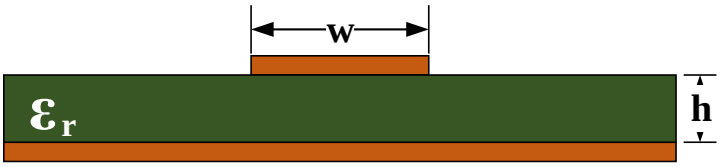

$$
\begin{aligned}
&\epsilon_{eff} = \frac{\epsilon_r + 1}{2} + \frac{\epsilon_r - 1}{2} \cdot \left[\frac{1}{\sqrt{1 + \frac{12h}{W}}} + 0.04\left(1 - \frac{W}{h}\right)^2 \right] \\
&\Delta W = \frac{t}{\pi} \cdot ln\left[\frac{4e}{(t/h)^2 + \left(\frac{1/\pi}{w/t+1.1}\right)^2} \right] \\
&\Delta W' = \Delta W \left(\frac{1 + 1/\epsilon_r}{2} \right) \\
&W' = W + \Delta W' \\
&Z_o = \frac{120\pi}{2 \cdot \sqrt{2} \cdot \pi \cdot \sqrt{\epsilon_r + 1}} \cdot ln\Bigg(1+ \\
&\frac{4h}{W'} \cdot \left[\frac{14 + 8/\epsilon_{eff}}{11} \cdot \frac{4h}{W'} + \sqrt{(\frac{14 + 8/\epsilon_{eff}}{11})^2 \cdot (\frac{4h}{W'})^2 + \frac{1 + 1/\epsilon_{eff}}{2} \cdot \pi^2} \right] \Bigg)
\end{aligned}
\tag{B.1}
$$

B.2 Coplanar Waveguide Z_o Calculation

The following are empirical formulas used to calculate the characteristic impedance of a coplanar waveguide where a is the width of the track, b is the width of the waveguide, and ϵ_r is the relative permittivity[38]. Other variables used in this equation are intermediate variables and K is an elliptical integral.

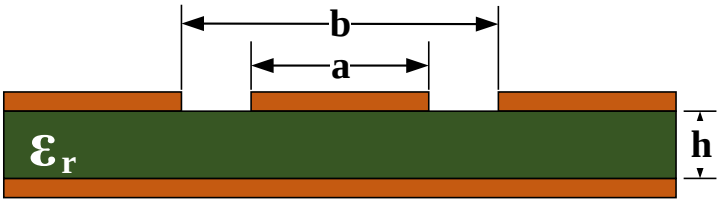

$$
\begin{aligned}
k &= \frac{a}{b} \\
kl &= \frac{tanh(\frac{\pi \cdot a}{4 \cdot h})}{tanh(\frac{\pi \cdot b}{4 \cdot h})} \\
kl' &= \sqrt{1 - kl^2} \\
k' &= \sqrt{1 - k^2} \\
K(k) &= \int_0^{\pi/2} \frac{1}{\sqrt{1 - k^2 \cdot (sin(\theta))^2}} d\theta \\
\epsilon_{eff} &= \frac{1 + \frac{\epsilon_r \cdot K(k') \cdot K(kl)}{K(k) \cdot K(kl')}}{1 + \frac{K(k') \cdot K(kl)}{K(k) \cdot K(kl')}} \\
Z_o &= \frac{60\pi}{\sqrt{\epsilon_{eff}}} \cdot \frac{1}{\frac{K(k)}{K(k')} + \frac{K(kl)}{K(kl')}}
\end{aligned}
\tag{B.2}
$$

References

[1] R. Dahai, W. Lingqi, Y. Meizhi, C. Mingyang, Y. Zheng, and H. Muzhi, "Design and analyses of a mems based resonant magnetometer", *Sensors*, vol. 9, no. 9, pp. 6951, 2009.

[2] S. Winkvist, "Low computational SLAM for an autonomous indoor aerial inspection vehicle", Master's thesis, University of Warwick, the Netherlands, 2013.

[3] Clean Flight, "Clean Flight", http://cleanflight.com, 2016, [Online; accessed 5-April-2016].

[4] Open Pilot, "Open Pilot", https://www.openpilot.org, 2016, [Online; accessed 5-April-2016].

[5] R. Mahony, V. Kumar, and P. Corke, "Multirotor aerial vehicles: Modeling, estimation, and control of quadrotor", *IEEE Robotics Automation Magazine*, vol. 19, no. 3, pp. 20–32, Sept 2012.

[6] M. Mueller and D. Raffaello, "A model predictive controller for quadrocopter state interception", in *Control Conference (ECC), 2013 European*. IEEE, 2013, pp. 1383–1389.

[7] S. Lupashin, A. Schoellig, M. Sherback, and R. D'Andrea, "A simple learning strategy for high-speed quadrocopter multi-flips", in *Robotics and Automation (ICRA), 2010 IEEE International Conference on*. IEEE, 2010, pp. 1642–1648.

[8] P.E. Santos L. Argentim, W. Contrimas and R. Aguiar, "Lqr and lqr-pid on a quadcopter platform", in *IEEE Int.Conference on Electronics, Informatics and Vision*. 2013, pp. 1–7, IEEE.

[9] M.G. Ortega G.V. Raffo and F.R. Rubio, "An integral predictive/nonlinear h infinity control structure for a quadrotor helicopter", in *Automatica*. 2013, pp. 1–7, IEEE.

[10] Pixhawk, "PIXHAWK is the all-in-one unit, combining FMU and IO into a single package", https://pixhawk.org/, 2016, [Online; accessed 15-May-2016].

[11] Tau Labs, "Sparky 2", https://github.com/TauLabs/TauLabs/wiki/Sparky2, 2016, [Online; accessed 15-May-2016].

[12] Z. Zhang, "Iterative point matching for registration of free-form curves and surfaces", in *Int. Journal of Computer Vision*. 1994, pp. 19–25, IEEE.

[13] Ji Zhang and Sanjiv Singh, "Loam: Lidar odometry and mapping in real-time", in *Robotics: Science and Systems Conference*, July 2014.

[14] N. Roy A. Bry, A. Bachrach, "State estimation for aggressive flight in gps-denied environments using onboard sensing", in *IEEE International Conference on Robotics and Automation*. 2012, pp. 19–25, IEEE.

[15] C. Hubert, *Electric Machines*, 2nd edition, 2002.

[16] NXP, "3-Phase BLDC Motor Control with Sensorless Back EMF Zero Crossing Detection Using 56F80x", cache.freescale.com/files/product/doc/AN1914.pdf, 2016, [Online; accessed 2-April-2016].

[17] NXP, "Sensorless PMSM Field-Oriented Control", http://www.nxp.com/doc/DRM148, 2016, [Online; accessed 2-April-2016].

[18] DJI, "Inspire 1", http://www.dji.com/product/inspire-1, 2015, [Online; accessed 2-April-2016].

[19] Andrew Gibiansky, "Quadcopter Dynamics and Simulation", http://andrew.gibiansky.com/blog/physics/quadcopter-dynamics, 2012, [Online; accessed 6-January-2016].

[20] CyPhy, "CyPhy LVL 1", http://www.cyphyworks.com/robots/lvl1/, 2015, [Online; accessed 2-April-2016].

[21] R. C. Hibbeler, *Statics and Dynamics*, 12th edition, 2010.

[22] ST Microchip, "Accelerometer and Gyroscopes Sensors: Operation, Sensing, and Applications", https://www.maximintegrated.com/en/app-notes/index.mvp/id/5830, 2015, [Online; accessed 21-April-2016].

[23] ST Microchip, "Tilt measurement using a low-g 3-axis accelerometer", http://www.st.com/web/en/resource/technical/document/application_note/CD00268887.pdf, 2013, [Online; accessed 2-Febuary-2016].

[24] V.B Bhatia, *Classical Mechanics: With introduction to Nonlinear Oscillations and Chaos*, Narosa Pub House, 1st edition, 1997.

[25] A. Trusov, "Overview of MEMS Gyroscopes: History, Principles of Operations, Types of Measurements", http://www.alexandertrusov.com/uploads/pdf/2011-UCI-trusov-whitepaper-gyros.pdf, 2011, [Online; accessed 13-April-2016].

[26] Freescale, "Layout Recommendations for PCBs Using a Magnetometer Sensor", cache.freescale.com/files/sensors/doc/app_note/AN4247.pdf, 2013, [Online; accessed 5-April-2016].

[27] Freescale Semiconductor, "Tilt Sensing Using a Three-Axis", http://www.freescale.com/files/sensors/doc/app_note/AN3461.pdf, 2013, [Online; accessed 2-Febuary-2016].

[28] S. Madgwick, "An efficient orientation filter for inertial and inertial/magnetic sensor arrays", Tech. Rep., University of Bristol, Department of Mechanical Engineering, Apr. 2010.

[29] Pieter Jan, "Reading a IMU Without Kalman: The Complementary Filter", http://www.pieter-jan.com/node/11, 2013, [Online; accessed 28-Febuary-2016].

[30] N. Nise, *Control Systems Engineering*, 6th edition, 2011.

[31] Federal Communications Commission, "Rules and Regulation for Title 47", https://www.fcc.gov/general/rules-regulations-title-47, 2016, [Online; accessed 15-May-2016].

[32] C. Balanis, *Antenna Theory: Analysis and Design*, 4th edition, 2015.

[33] Maxim Integrated, "Impedance Matching and the Smith Chart: The Fundamentals", https://www.maximintegrated.com/en/app-notes/index.mvp/id/742, 2002, [Online; accessed 16-April-2016].

[34] Texas Instruments, "Low-Cost Low-Power 2.4 GHz RF Transceiver", http://www.ti.com/lit/ds/symlink/cc2500.pdf, 2016, [Online; accessed 16-April-2016].

[35] Johanson Technology, "2.45 GHz Impedance mathced Balun-Filter for Texas Instruments' CC2500, CC2510, and CC2511 Chipsets", http://www.johansontechnology.com/datasheets/baluns/Balun_Filter_Matched_2450BM15B0003_v4.pdf, 2012, [Online; accessed 16-April-2016].

[36] ArduPilot Dev Team, "Extended Kalman Filter Navigation Overview and Tuning", http://ardupilot.org/dev/docs/extended-kalman-filter.html#extended-kalman-filter, 2016, [Online; accessed 22-April-2016].

[37] A. Censi, "An icp variant using a point-to-line metric", in *2008 IEEE International Conference on Robotics and Automation*. 2008, pp. 19–25, IEEE.

[38] B. Wadell, *Transmission Line Design Handbook*, 1st edition, 1991.

[39] S. O. H. Madgwick, "Estimation of imu and marg orientation using a gradient descent algorithm", in *IEEE International Conference on Rehabilitation Robotics*. 2011, pp. 1–7, IEEE.

[40] Lauszus Kristian, "Flight Controller for Quad Rotor Helicopter in X-configuration", Master's thesis, Technical University of Denmark, the Netherlands, 2015.

[41] M.J. Thompson, "LORENTZ FORCE MEMS MAGNETOMETER", http://www-bsac.eecs.berkeley.edu/publications/search/send_publication_pdf2client.php?pubID=1271176542, 2010, [Online; accessed 4-Febuary-2016].

[42] Ingo Ltkebohle, "BWorld Robot Control Software", http://aiweb.techfak.uni-bielefeld.de/content/bworld-robot-control-software/, 2008, [Online; accessed 2-Febuary-2016].

[43] Freescale Semiconductor, "Tilt Sensing Using a Three-Axis", http://www.freescale.com/files/sensors/doc/app_note/AN3461.pdf, 2013, [Online; accessed 2-Febuary-2016].

[44] Senodia, "What is MEMS?", http://senodia.com/technology.aspx?id=275, 2013, [Online; accessed 2-Febuary-2016].